Study and Modelling of the Melt Pool Dynamics during Selective Laser Sintering and Melting

THÈSE N^{O} 6826 (2015)

PRÉSENTÉE LE 26 NOVEMBRE 2015
À LA FACULTÉ DES SCIENCES ET TECHNIQUES DE L'INGÉNIEUR
LABORATOIRE DE GESTION ET PROCÉDÉS DE PRODUCTION
PROGRAMME DOCTORAL EN SYSTÈMES DE PRODUCTION ET ROBOTIQUE

ÉCOLE POLYTECHNIQUE FÉDÉRALE DE LAUSANNE

POUR L'OBTENTION DU GRADE DE DOCTEUR ÈS SCIENCES

PAR

Tatiana POLIVNIKOVA

acceptée sur proposition du jury:

Prof. J. A. Schiffmann, président du jury
Prof. R. Glardon, Dr E. Boillat, directeurs de thèse
Dr Ph. Thévoz, rapporteur
Dr V. Romano, rapporteur
Dr A. Jacot, rapporteur

ÉCOLE POLYTECHNIQUE
FÉDÉRALE DE LAUSANNE

Suisse
2015

To Sveta and Nadia

Acknowledgements

Foremost I would like to thank my thesis directors, Rémy Glardon and Eric Boillat, for the possibility to be a part of LGPP during these four years and to work in its calm and friendly atmosphere. Thank you for your support, for the encouragement and motivation and for the patience during long discussions.

I am also grateful to the members of the thesis jury, Valerio Romano, Alain Jacot, Philippe Thévoz and Jürg Schiffmann, for the interest to my work, for the insightful comments, and for the fact, that the question session during my private defense turned into an interesting scientific discussion, which allowed me to look at my work at a new angle.

My sincere thanks to Christoph Van Gestel, Jamasp Jhabvala and Pascal Clausen for the fruitful collaboration. I am also grateful to Marc Matthey for the technical support at all time.

I would particularly like to thank Ioanna Paniara and Corinne Lebet for their help in solving administrative problems.

I am very much grateful to my fellow labmates, Maryam Darvish, Christos Tsagkalidis and Nikola Kalentic for the moral support. Working with you was a pleasure.

This work would not be possible without help of my dear family. I cannot say how much I am thankful to my mother, Olga Polivnikova, for her love and support. And I will always be grateful to the members of my family, who unfortunately are no longer here, but who significantly influenced my personality: my beloved grandfather Valentin Leonov and my godfather Boris Djubua.

I would also like to thank Sergey Kolosov, a good friend of mine, for the given opportunities.

And I have no words to express my gratitude to my Russian friends, Anna Popkova, Nadia Sergeeva, Yuri Sergeev, Sveta Korotkova and Ilya Koshkin, who supported me all these years, despite the distance separating us. Actually, this work I dedicate to friendship.

Lausanne, 23 September 2015 T. P.

Abstract

Selective Laser Sintering (SLS) and Selective Laser Melting (SLM) are parent layer manufacturing processes that allow generating complex 3D parts by consolidating layers of powder material on top of each other. Consolidation is obtained by processing the selected areas using the thermal energy supplied by a focused laser beam. In SLS partial fusion of powder particles takes place, followed by a solidification of the created liquid. SLM is essentially the same process as SLS, with the difference that the particles are completely molten under the laser beam. This development is driven by the need to produce near full dense objects, with mechanical properties comparable to those of bulk materials and by the desire to avoid lengthy post processing cycles. Identification of the optimal process conditions (so-called process window) is a crucial task for industrial application of SLS/SLM processes. Operating parameters of the process are adjusted in correspondence with optical and thermal properties of the processed material. Nowadays in SLS/SLM there is a tendency to increase the speed of the fabrication as a consequence of the available higher laser powers. It leads to increase of laser scanning speeds. In these circumstances, to rely only on experimental investigations in order to adjust process and material parameters is time-consuming and ineffective. Simulation tools are strongly needed for the visualization and analysis of SLS/SLM processes.

In SLM the powder grains under the laser are completely molten and form a liquid domain called melt pool. Evolution of the melt pool during the process, its interaction with the laser, the substrate and the surrounding non-molten powder strongly affect the quality of the final part.

The goal of this work is to study the melt pool dynamics by means of a finite-element simulation software, built specially for SLS/SLM. The numerical model is based on the homogeneous medium hypothesis. It considers the interaction between the laser and the powder material, the phase transformations and the evolution of the material properties during the process. We also study the influence of the phase change on the process efficiency.

The macroscopic model is completed by the sub-models, which allow to study at microscopic level the processes taking place in the powder bed during its laser heating and melting. Melting of separate powder particles during laser irradiation is studied by means of the improved Single Grain Model. The capillary phenomena taking place in the powder bed during SLS/SLM are also considered. The interconnection of powder grains during their melting is approached by the mechanism of liquid drops coalescence. According to the obtained results, the depth-dependent sintering threshold for powder materials is proposed.

Key words: Selective Laser Sintering, Selective Laser Melting, powder, 18Ni(300) Maraging Steel, numerical model, finite element, temperature, enthalpy, sintering threshold, process efficiency, melt pool, stabilization, effective thermal conductivity, absorptivity, Single Grain Model, plane wave, capillary, liquid drop, coalescence.

Résumé

Le frittage sélectif par laser (SLS) et la fusion sélective par laser (SLM) sont des procédés de fabrication additifs voisins qui permettent de construire des pièces 3D de géométrie compliquées en consolidant localement des couches de poudre l'une au-dessus de l'autre. Les zones à consolider sont mises en fusion grâce à l'énergie thermique fournie par un faisceau laser finement focalisé. La cohésion du matériau est obtenue après un processus de resolidification complexe. Dans le procédé SLS la fusion des particules de poudre n'est que partielle. Le procédé SLM est essentiellement le même à la différence près que les particules sont complètement fondues. Le développement du procédé SLM à partir du procédé SLS plus ancien a été motivé par la nécessité de produire des objets entièrement denses, avec des propriétés mécaniques comparables à celles des pièces obtenues en fonderie, usinage ou forgeage et sans avoir à passer par de longs cycles de post-traitement. L'identification de conditions opératoires optimales est une tâche cruciale pour l'application industrielle des procédés SLS/SLM. Dans la pratique, les paramètres du procédé sont adaptés aux propriétés optiques et thermiques du matériau utilisé. De nos jours, l'augmentation de la puissance des lasers disponibles sur le marché a permis une augmentation des vitesses de production des procédés SLS/SLM. Dans ces conditions, les approches purement expérimentales pour la mise au point des paramètres procédé sont coûteuses et relativement peu efficaces. Les outils de simulation sont donc devenus nécessaires pour l'optimisation et l'analyse des technologies SLS/SLM.

Dans le procédé SLM, les grains de poudre sous le laser sont fondus complètement. Ils forment un domaine liquide appelé bain de fusion. L'évolution de ce domaine au cours du processus, de son interaction avec le laser, le substrat et la poudre non fondue affectent fortement la qualité de la pièce finale.

Le but de ce travail est d'étudier la dynamique du bain de fusion au moyen d'un logiciel de simulation par éléments finis, adapté spécialement aux procédés SLS / SLM. Le modèle numérique est basé sur la technique mathématique d'homogénéisation du milieu traité et prend en compte de nombreux mécanismes comme l'interaction entre le laser et la poudre, les transformations de phase et l'évolution des propriétés du matériau en cours de consolidation. Nous étudions également l'influence du changement de phase sur l'efficacité du procédé.

Le modèle macroscopique est complété par des sous-modèles, qui permettent d'étudier des processus qui se déroulent, à l'échelle microscopique, dans le lit de poudre lors de son traitement par laser. La fusion des particules de poudre en cours d'irradiation est étudiée au moyen d'une généralisation du modèle classique du grain isolé. Les phénomènes de capillarité se produisant dans le lit de poudre pendant les procédés SLS/SLM sont également étudiés. En particulier, l'interconnection des grains de poudre en cours de fusion est analysée grâce à des modèles (théoriques et numériques) de coalescence de gouttes. Les résultats obtenus ont notamment conduit à la définition d'un seuil de frittage dépendant de l'intensité du faisceau laser et de ses propriétés de pénétration dans la poudre.

Mots clefs : frittage sélectif par laser, fusion sélective par laser, poudre, acier maraging 18Ni (300), modèle numérique, éléments finis, température, enthalpie, seuil de frittage, efficacité des processus, bain de fusion, stabilisation, conductivité thermique effective, absorption effective, modèle du grain isolé, onde plane, écoulement capillaire, goutte de liquide, coalescence.

Contents

List of Figures

List of Tables

List of Symbols

A_{mp} Surface area of the stabilized melt pool

C_p Heat capacity

E^d_{surf} Surface laser energy density

E^d_{vol} Volume laser energy density

E_a Activation energy

I_0 Incident radiation intensity

I_r Reflected radiation intensity

L_c Characteristic length

L_f Latent heat of fusion

L_v Latent heat of vaporization

M_{th} Powder grain thermal mass

N Mean coordination number

P Laser power

Q Intensity distribution of the heat source

R Reflectivity of the material

R_g Universal gas constant

T Temperature

T_0 Temperature of the environment

T^0_{av} Average temperature of the grain at the moment t_0 (SGM)

T_f Melting temperature

T_t	Melting threshold temperature
T_t^{SGM}	Melting threashold of the powder grain
T_v	Boiling temperature
Ω	Working domain
Φ	Sintering potential
Σ_p	Contact thermal resistance between two powder particles
α	Surface absorptivity of the material
α_l	Surface absorptivity of liquid material
α_p	Surface absorptivity of the powder
α_s	Surface absorptivity of solid material
δ	Optical penetration depth of the material
δ_0	Radius of the sphere, used for temperature averaging
η	Thermal diffusivity
γ	Liquid-gas surface tension
γ_a	Adiabatic exponent of the gas phase
κ	Thermal exchange coefficient
$\mathbf{E}_0$	Electric amplitude of the plane wave
$\mathbf{s_t}$	Poynting vector
Bo	Bond number
Kn	Knudsen number
$\mathrm{Nu_l}$	Nusselt number
$\mathrm{Ra_l}$	Rayleigh number
μ	Dynamic viscosity of the liquid
μ_p	Vacuum magnetic permeability
ω	Laser beam radius
ρ	Density
ρ_l	Liquid material density

ρ_p Powder density

ρ_s Solid material density

σ Stefan-Boltzmann constant

τ_M Maxwell relaxation time of the liquid

τ_{sint} Characteristic sintering time of the material

v Laser scanning speed

ε Material emissivity

ε_I Imaginary part of the dielectric constant

ε_R Real part of the dielectric constant

ε_d Dielectric constant

ζ Sintering rate

d_0 Powder grain diameter

$d_{\mathrm{mp}}^{\mathrm{b}}$ Melt pool stabilization distance for the bulk material

$d_{\mathrm{mp}}^{\mathrm{pl}}$ Melt pool stabilization distance for the powder layer

$d_{\mathrm{mp}}^{\mathrm{th}}$ Theoretical stabilization distance of the melt pool

f_s Fraction of the solid material

g Gravitational acceleration

$h_{\mathrm{mp}}^{\mathrm{pb}}$ Melt pool depth in the powder bed

h_h Hatching distance

h_l Powder layer thickness

k Effective thermal conductivity

k_{atm} Thermal conductivity of the surrounding atmosphere

k_g Thermal conductivity of gas phase

k_l Effective thermal conductivity of liquid material

k_s Effective thermal conductivity of solid material

l_0 Gas mean-free path

q Heat source induced by Joule heating in the powder grain

q_{abs} Heat flux corresponding to absorbed heat

q_{conv} Heat flux corresponding to convective heat losses

q_{rad} Heat flux corresponding to radiative heat losses

q_{surf} Surface heat source

r_0 Powder grain radius

r_c Contact radius

t Time

t^0 Time of contact point melting (SGM)

t^{tr} Transition time of the surface state within the laser spot

t^i_{max} Maximum time of the grain irradiation (SGM)

t^l Time of complete grain melting (SGM)

t^s Time to melting of the powder grain (SGM)

t_{att} Time when the melt pool touches the substrate

t^{b}_{mp} Melt pool stabilization time for bulk material

$t^{\text{pb}}_{\text{mp}}$ Melt pool stabilization time for powder bed

$t^{\text{pl}}_{\text{mp}}$ Melt pool stabilization time for powder layer on the substrate

$t^{\text{th}}_{\text{mp}}$ Theoretical melt pool stabilization time

t_c Time of liquid drops coalescence

u Enthalpy per unit mass

1 Introduction

Selective Laser Sintering (SLS) and Selective Laser Melting (SLM) are parent layer manufacturing processes that allow generating complex 3D parts by consolidating layers of metallic, ceramic, or polymer powder material on top of each other. Consolidation is obtained by processing the selected areas using the thermal energy supplied by a focused laser beam. In SLS partial fusion of powder particles takes place, followed by a solidification of the created liquid. SLM is essentially the same process as SLS, with the difference that the particles are completely molten under the laser beam and form a liquid domain called melt pool. The main advantages of SLS/SLM are three-dimensional geometrical freedom, complying with modern design requirements, mass customization and material flexibility.

Industrial application of SLS/SLM technologies requires from the process rather strict conditions to be fulfilled: porosity, hardness, surface roughness, geometrical accuracy and other properties of the final part should be sufficient to guarantee its reliability over the entire life cycle. The economical aspects – production time and cost – also should be considered.

SLS/SLM operating parameters (so-called process window) are adjusted in correspondence with optical and thermal properties of the material. Nowadays in SLS/SLM there is a tendency to increase the speed of the fabrication as a consequence of the available higher laser powers. Identification of the optimal process parameters is a crucial task for industrial application of SLS/SLM.

Efficiency of SLM process and the quality of the final part are strongly connected to the evolution of the melt pool during the process, its interaction with the laser, the substrate and the surrounding non-molten powder. Knowledge of the melt pool geometry allows to adjust such important operating parameters as hatching distance of the scanning strategy and powder layer thickness. Prediction of the melt pool surface area evolution and melt pool position with respect to the laser helps to estimate and increase process efficiency and can be also useful for the calibration of online monitoring systems for Selective Laser Melting.

Parameters of the melt pool and the character of its interaction with the laser radiation during SLM are defined by the evolution of thermal and optical properties of the powder due to its melting. Physical laws, describing this evolution, are related to the phenomena taking place in the powder at the level of powder grains: to their melting dynamics and their interaction in the presence of the liquid phase.

We can see that SLS/SLM processes involve dynamical phenomena, strongly dependent on numerous parameters. To rely only on experimental investigations in this case is time-consuming, ineffective and expensive. Numerical modelling of SLS/SLM is strongly needed.

All numerical approaches, developed for SLS/SLM, describe a working domain (a powder on a substrate) with some thermal and mechanical properties and certain boundary conditions and a heat source of a specified profile shape, which interacts with the domain. One of the commonly used modelling methods is based on the description of the heat transfer in the homogenized working domain, characterized by its effective properties. However, as mentioned above, it is clear that for better understanding of SLS/SLM it is necessary to consider the process at microscopic level, i.e. at the level of powder grains. Generally it leads to the increase of numerical model complexity and, consequently, to the decrease of computation speeds.

The solution to this problem is in the use of a numerical model based on material homogenization, completed with separate sub-models simulating the process at the powder grain level. The sub-models can be divided in two categories:

- models, describing the effective properties of a loose powder;
- models, studying powder grain melting dynamics and their interaction in the presence of the liquid phase.

Results of these sub-models, added to the basic macroscopic model, will allow to simulate the SLS/SLM even in the absence of large computing powers.

1.1 Research objectives

This study will focus on the following objectives:

1. *Development of theoretical models for the description of the loose powder effective properties.*
2. *Development of theoretical models describing the melting dynamics and the interactions of molten powder particles during SLS/SLM.*
3. *Theoretical investigation and numerical simulation of SLS/SLM using a macroscopic model based on the homogeneous medium hypothesis, completed by the results of microscopic sub-models.*
4. *Estimation of the influence of material properties evolution on SLS/SLM process efficiency.*
5. *Study of the properties and dynamics of the melt pool formed during SLM process.*

This work is mainly concerned by the study of SLS and SLM of 18Ni(300) Maraging Steel powder. The considered operating parameters are chosen in accordance with modern industrial requirements.

1.2 Thesis structure

The structure of this work is as follows. Chapter 2 introduces main principles of Selective Laser Sintering and Selective Laser Melting. It also discusses process requirements and describes commonly used approaches for the numerical simulation of SLS/SLM.

In Chapter 3, 18Ni(300) Maraging Steel is studied. Properties of the solid and liquid phases of the material are discussed. Different methods for estimating the effective powder parameters are also introduced. The process parameters, chosen in the context of this study, are also presented.

In Chapters 4 and 5, we introduce the models studying SLS/SLM at the powder grain level. In Chapter 4, using the improved Single Grain Model, we study melting of a separate powder particle. We approach laser irradiation by a plane wave. Melting time and threshold temperature of a powder grain are estimated. Chapter 5 focuses on the capillary phenomena taking place in the powder during melting. The dynamics of molten powder grain interconnection is considered in the framework of the liquid drop coalescence model.

Chapter 6 describes the numerical methods used to discretize the macroscopic SLS/SLM model. Theoretical assumptions, based on the results of Chapters 4 and 5, are presented. Recommendations about the space and time discretization are given.

Chapter 7 introduces a model for a depth-dependent sintering threshold, based on the results of the Single Grain Model (Chapter 4). An experimental validation of this model is also presented.

Chapter 8 focuses on phenomena, taking place during SLS/SLM, which can influence the process efficiency. The evolution of powder effective parameters due to the phase change is studied, convective and radiative losses are estimated.

In Chapter 9 the melt pool dynamics during SLM is discussed. Evolution of the melt pool during the process is studied and melt pool stabilization criteria are presented. A method to adjust the powder layer thickness, according to material and process parameters, is also introduced.

2 State of the Art

Selective Laser Sintering (SLS) and Selective Laser Melting (SLM) are parent Additive Manufacturing processes using a laser to melt and solidify metallic, ceramic, polymer or composite powders. Additive manufacturing is the name given to a host of related technologies used to create physical objects by sequential deposition of material layers. The originality of Additive Manufacturing is that material is added to form the desired part and not subtracted from a bigger part. All the non-used material can be recycled in the next construction.

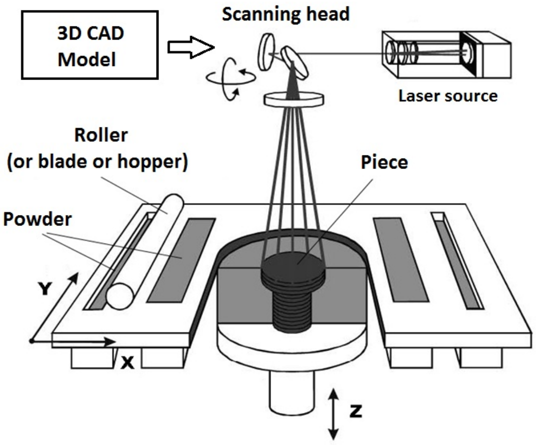

Figure 2.1 – The SLS process scheme [1].

2.1 SLS/SLM process definition

Selective Laser Sintering (SLS) is a layer manufacturing process that allows generating complex 3D parts by consolidating layers of powder material on top of each other [6, 7]. The object is built layer by layer. Consolidation is obtained by processing the selected areas using the thermal energy supplied by a focused laser beam (Fig. 2.1). Using a beam deflection system, each layer is scanned according to its corresponding cross-section as calculated from the CAD model. Partial fusion of the particles takes place, followed by a solidification of the created liquid.

Selective Laser Melting (SLM) is essentially the same process as SLS, with the difference that the particles are completely molten under the laser beam and form a liquid bath (a melt pool). This development was driven by the need to produce near full dense objects, with mechanical properties comparable to those of bulk materials and by the desire to avoid lengthy post-processing cycles.

The main advantages of SLS/SLM are three-dimensional geometrical freedom, complying with modern design requirements, mass customization and material flexibility. In contrast to material removal techniques, complex parts can be fabricated without the need for lengthy tool path calculations. Shapes that may not be realizable by conventional machining can be built (conformal cooling channels in injection molds) [1]. SLS/SLM technology makes it possible to create fully functional parts directly from metals, ceramics and plastics without using any intermediate binders or any additional processing steps after the laser sintering operation [8, 9, 10, 11]. Remaining unprocessed powder can be reused.

2.1.1 Binding mechanisms

Different binding mechanisms can be responsible for the consolidation of the powder during SLS and SLM processes [12, 13, 14]:

- ***Solid State Sintering (SSS)***. Occurs below the material melting temperature: diffusion of atoms in solid state (volume diffusion, grain boundary diffusion or surface diffusion [15, 16]) creates necks between adjacent powder particles growing with time [17, 18]. The mechanism is rarely applied as diffusion of atoms in solid state is slow and does not meet the requirements of the process.
- ***Liquid Phase Sintering (LPS)***. Part of the powder material is molten while other parts remain solid. The liquefied material spreads between the solid particles almost instantaneously as it is driven by intense capillary forces. The material that melts may be different from the one remaining solid: the 'low melting point' material is called the binder, while the 'high melting point' material is generally called the structural material. The binder may remain as part of the final product or may be removed during a debinding cycle. Binder and structural materials can be brought together simply by using a mixture of two-component powders, or they can be combined in composite or coated powders.
- ***Partial Melting***. The heat supplied to a powder particle is sufficient only to melt the grain surface, while particle core remains solid. The molten material plays the role of the binder. Small necks are formed between the non-molten particle cores [1]. This binding mechanism is used for metals. The technique is sometimes called ***Direct Metal Laser Sintering (DMLS)*** [15].
- ***Full Melting***. Applied to achieve fully dense parts without need for any post-processing. One of the most popular technologies nowadays. However, to achieve satisfactory results, requires a detailed preliminary analysis of the material and process parameters (so-called process window). For each new material, a process-window needs to be determined separately, in order to avoid scan track instabilities (sphereodisation of the liquid melt pool, also known as 'balling') and part porosity [19, 20].

2.1.2 Materials and applications

SLS/SLM technologies are widely used in various industries, medicine and research, offering a range of advantages compared to conventional manufacturing techniques. Most of the materials, used in SLS/SLM, are developed by machine makers and are strictly application-oriented [14, 21].

- *Metals.* Iron-based powders and various steels (moulds and tools [22, 23, 24]), titanium-based powders and Co-Cr (implants and scaffolds).
- *Polymers.* Polyamide, polystyrene and PEEK (SLS plastics), PCL (biomedical applications), PVA, PC.
- *Ceramics.* HA, SiC, ZrO_2, Al_2O_3, glass-ceramic, Ta_2O_5, bismuth titanate. Least-processed materials by SLS/SLM, as far as they are susceptible to develop cracks.

2.1.3 Requirements to the process

Industrial application of Selective Laser Sintering/Melting requires from the process rather strict conditions to be fulfilled: porosity, hardness, surface roughness, geometrical accuracy and other properties should be sufficient to guarantee the reliability of the final product over the entire life cycle. It is also necessary to consider the economical aspects of the process – production time and cost.

Laser power and laser scanning speed are adjusted in correspondence with optical and thermal properties of the process material. In the case of polymers and composites the technique is now well understood and widely used, but for metals and ceramics it still suffers from a lack of precision, surface roughness and poor mechanical properties. Identification of the optimal process parameters (process window) is a crucial task for industrial application of SLS/SLM processes.

According to the industrial requirements, nowadays in SLS/SLM there is a tendency to increase the speed of the fabrication as a consequence of the available higher laser powers (up to 1 kW). For metal powders it leads to increase of scanning speeds (up to 3 – 4 m/s).

2.2 Characterization of SLS/SLM process

Material and process parameters, listed in §§ 2.1.2 – 2.1.3, are strongly related to each other. Laser and scanning parameters are adjusted according to chemical, optical and heat transfer properties of the processed material.

2.2.1 Process parameters

The relation between laser and strategy parameters defines the amount of energy received by a processed material and, subsequently, is of a great influence on the product properties. It would be convenient to have a variable which can link all the process parameters and, therefore characterize SLS/SLM process.

Laser energy density is a commonly used factor to characterize SLS/SLM process and properties of a final sintered part. Generally energy density can connect laser power, scanning speed, hatching distance of the scanning strategy, laser beam diameter and thickness of the powder layer.

According to [25, 26, 27, 28] surface laser energy density E^d_{surf} (in J/m^2) can be expressed as:

$$E^d_{\mathrm{surf}} = \frac{P}{v h_h}, \quad \text{or} \quad E^d_{\mathrm{surf}} = \frac{P}{2 v \omega}, \tag{2.1}$$

where P is the laser power, v – the scanning speed, h_h – the hatching distance and ω – the radius of the laser beam.

An expansion of the expression (2.1) is proposed in [29]:

$$E^d_{\mathrm{surf}} = \frac{P}{v h_h} x, \tag{2.2}$$

where ratio $x = 2\omega / h_h$ characterizes the overlapping of the trace of a laser beam spot.

Volume based laser energy density E^d_{vol} (in J/m^3) is also widely used for the characterization of SLS/SLM processes [30]:

$$E^d_{\mathrm{vol}} = \frac{P}{v h_h h_l}, \tag{2.3}$$

where h_l is the thickness of a powder layer.

However, it can be seen, that volumic density of laser energy doesn't take into account the diameter of the laser beam and the beam profile. Therefore, it can be reasonable to add another factor, characterizing the laser – laser intensity or laser fluence.

In fact, no one of the parameters (2.1) – (2.3) reflects all the details of the Selective Laser Sintering/Melting process due to its non-linearities. We will discuss this problem in detail in the next chapters.

2.2.2 Material parameters

One of the commonly used methods to characterize a powder is to consider it as a homogeneous medium with some effective properties. We will discuss this model in detail in Chapter 6.

In the framework of the homogeneous medium hypothesis, a powder bed, like any homogeneous material, can be characterized by its thermal diffusivity $\eta = k/\rho/C_p$, where C_p is the heat capacity of the material, ρ is the powder bed density and k is the effective value of its thermal conductivity. Optical parameters of a powder bed are described by its effective surface absorptivity and optical penetration depth.

During SLS/SLM powder properties evolve to the parameters of a bulk material. In this study we will discuss the consequences of this evolution.

However it is clear, that the modification of parameters during laser sintering/melting is the result of changes in the structure of the powder bed. For better understanding of SLS/SLM at macroscopic level, we need to consider processes, which take place at the level of a powder particle, like melting, rearrangement and interaction of powder grains. Therefore powder properties (packing, grain size distribution, etc.) strongly influence the process.

2.3 Numerical modelling of SLS/SLM

The complexity of SLS/SLM processes is that they involve dynamical phenomena, caused by a time dependent temperature distribution [31]. These phenomena are strongly dependent on many parameters. Process variables for SLS/SLM technologies can be divided in several groups:

(a) *Material properties*: Chemical composition, size distribution, shape, optical and heat transfer properties of powder and molten material.

(b) *Laser parameters*: Laser power, spot size, beam spatial distribution, scanning speed, possibly pulse rate and duration.

(c) *Strategy of manufacturing*: Scanning strategy, powder deposition parameters, powder layer thickness, application of a protective atmosphere, preheating.

To rely only on experimental investigations in order to adjust process and material parameters is time-consuming, ineffective and expensive. Simulation tools are strongly needed for the visualization and analysis of SLS/SLM processes.

All numerical approaches, developed for SLS/SLM modelling, describe a powder bed with some thermo-mechanical properties and certain boundary conditions and a heat source of a specified profile shape, which interacts with the powder bed. First attempts aiming to describe theoretically the mechanisms of the heat transfer in a powder bed were made in [17, 32, 33]. Mathematical models of the heat distribution for single scan tracks were proposed in [34, 35]. In [36] an analytical model was used to evaluate the temperature field created in a titanium sample during pulsed laser treatment. Finite element analysis by means of commercial software was performed in [37] for laser enamelling. A finite element numerical model, based on the relations between specific enthalpy, temperature and sintering potential, was introduced in [38] (see Chapter 6 for details). In [39] the transient temperature field for $TiAl_6V_4$ SLM parts was predicted. A 3D model for the analysis of the relations between the process parameters and the mass of a powder layer was proposed in [40].

All these models, described above, are based on the homogenization of a powder bed. However the question of interaction of laser radiation with a powder, considered as a packing of particles, was also studied. Numerical model, based on the solution of Radiation Transfer Equation (RTE) for the absorbing and scattering medium was proposed in [41, 42]. For the same purpose ray-tracing modeling was used in [7, 43].

Evolution of effective thermal parameters of a powder bed during SLS/SLM was studied in [38, 44, 45, 46].

Nowadays there is a tendency to model SLS/SLM processes not only at macroscopic, but also at microscopic level, aiming to study powder melting dynamics. These models are often based on the solution of Navier-Stokes equations (for example [47]). However the lattice Boltzmann method (LBM) becomes more popular [48].

3 18Ni(300) Maraging Steel Powder

This work is mainly concerned by the study of Selective Laser Sintering and Selective Laser Melting of 18Ni(300) Maraging Steel powder. In this Chapter we describe the properties of the bulk material. We also discuss the effective values of the thermal conductivity and of the light absorptivity in the loose powder. We introduce different methods to estimate the effective parameters. For the estimation of the effective powder absorptivity we use a theoretical approach based on the solution of the radiation transfer equation. For the calculation of the effective thermal conductivity of a powder bed we apply a discrete thermal resistances model. We also introduce an experimental validation of these theoretical methods.

Besides that we introduce and discuss process parameters chosen for this study.

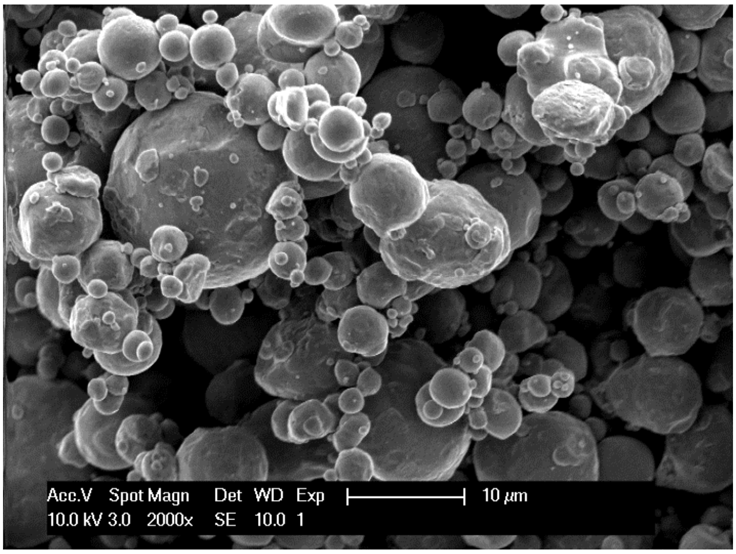

Figure 3.1 – 18Ni(300) Maraging Steel Powder.

3.1 Grain size distribution

The photo of 18Ni(300) Maraging Steel powder we study is shown in Fig. 3.1. The grain size distribution of the powder can be seen in Fig. 3.2 [2]. In this work the details of the real distribution will not really be taken into account. Instead we will often approach it by a monosized distribution for a diameter d_0= 8.87 μm, which corresponds to a radius r_0= 4.435 μm.

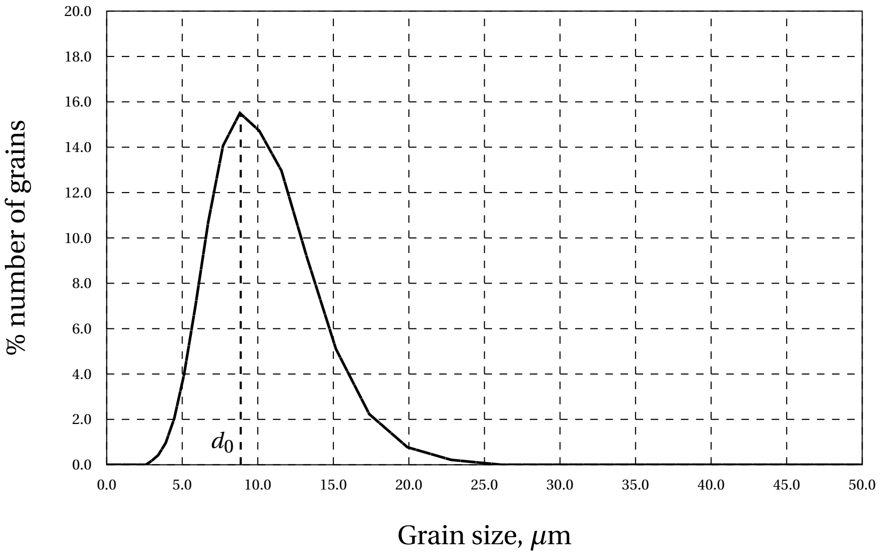

Figure 3.2 – Grain size distribution of the 18Ni(300) Maraging Steel powder [2].

Aluminum, Al	0.10 %
Boron, B	$\leq$ 0.0030 %
Carbon, C	$\leq$ 0.030 %
Cobalt, Co	9.0 %
Iron, Fe	67.0 %
Manganese, Mn	$\leq$ 0.10 %
Molybdenum, Mo	4.80 %
Nickel, Ni	18.5 %
Phosphorous, P	$\leq$ 0.010 %
Silicon, Si	$\leq$ 0.10 %
Sulfur, S	$\leq$ 0.010 %
Titanium, Ti	0.60 %
Zirconium, Zr	0.010 %

Table 3.1 – 18Ni(300) Maraging Steel chemical composition [2].

Density of the solid material ρ_s	0.008 g/mm^3
Thermal conductivity k_s	26 W/m/°C
Heat capacity C_p (for $T >$ 1091°C)	0.5 J/g/°C
Melting temperature T_f	1413 °C
Boiling temperature T_v	2862 °C
Latent heat of fusion L_f	247 J/g
Latent heat of vaporization L_v	6260 J/g

Table 3.2 – 18Ni(300) Maraging Steel bulk material properties.

3.2 Bulk material properties

The chemical composition of the 18Ni(300) Maraging Steel bulk material is given in Tab. 3.1.

Other physical properties are presented in Tab. 3.2. According to [2], we assume $T_f = 1413$°C as the material melting point. Due to lack of complete information, they do not all correspond exactly to 18Ni(300) Maraging Steel. Sometimes they have been interpolated from the properties of pure iron or close grades of steel. The values L_f and L_v correspond to the latent heat of fusion and latent heat of vaporization of Grade 316 Stainless Steel, respectively [49, 50]. For T_v we take the vaporization point of iron.

According to [2], the density ρ_s of 18Ni(300) Maraging Steel is not dependent on temperature. The thermal conductivity of the material at 50 °C is $k_s = 25.8$ W/m/°C [2]. We round this value to 26 W/m/°C and assume it to be constant. The heat capacity C_p strongly depends on temperature. The value given in Tab. 3.2 ($C_p = 0.5$ J/g/°C) will only be used for temperatures $T > 1091$°C. For smaller values of T, the heat capacity can be deduced from the data concerning the β-function of the material (see Fig. 3.3).

β-function

In Chapter 6, describing the numerical model, we will use the so-called β-function, which connects the enthalpy per unit mass u to the temperature T. The β-function of 18Ni(300) Maraging Steel has been measured by EMPA [51] for $u < 598.9$ J/g and under the assumption that $\beta(0) = 0$ which means that

$$u = 0 \text{ J/g, when } T = 0°\text{C}. \tag{3.1}$$

For values of u larger than 598.9 J/g, the β-function is constructed under the assumption that $C_p \simeq 0.5$ J/g/°C and by taking the values of L_f, L_v, T_f and T_v into account (see Tab. 3.2). The final result is presented in Fig. 3.3. Fig. 3.3b is the zooming of the grey area on the graph Fig. 3.3a.

3.3 Powder properties

As it will be explained in detail in Chapter 6, we will consider the powder bed as a homogeneous medium, which is characterized by effective properties: surface absorptivity, optical penetration depth, thermal conductivity and density. These parameters strongly depend on powder geometry and material properties.

In this section we present methods to estimate the effective properties. We also discuss assumptions we have to make for the 18Ni(300) Maraging Steel powder.

3.3.1 Surface absorptivity and optical penetration depth

The ability of a powder to absorb laser energy is one of the key factors for the SLS/SLM process quality. In general, when electromagnetic radiation is incident to the surface of a medium, it is partially reflected from the surface and partially penetrates into the material (Fig. 3.4). The reflected part of the radiation I_r, if non-linear phenomena are neglected, can be expressed as:

$$I_r = RI_0, \tag{3.2}$$

where I_0 is the intensity of the incident radiation and R is the reflectivity (or the reflection coefficient) of the material. Further in this study, to characterize the ability of the material to absorb radiation, we will use the notion of the *surface absorptivity*:

$$\alpha = 1 - R. \tag{3.3}$$

In fact, surface absorptivity of a medium is defined as the fraction of the incident radiation which penetrates into the medium.

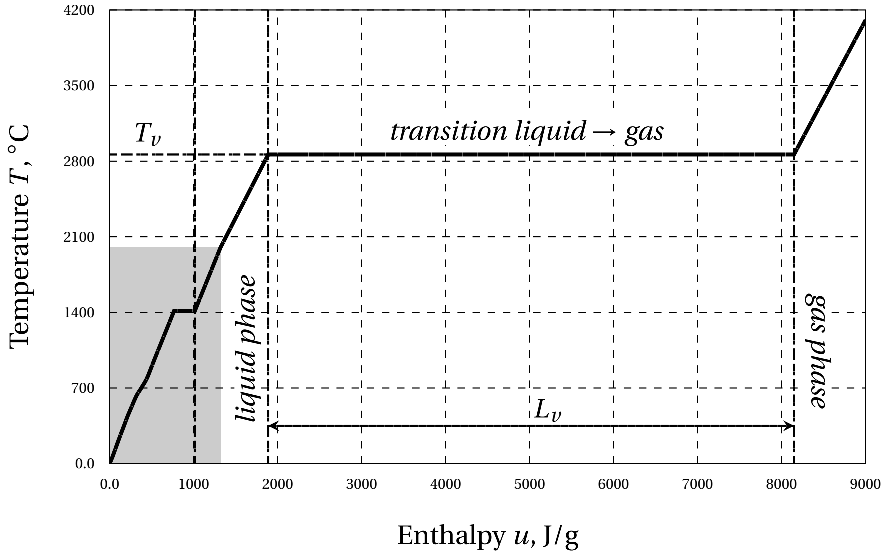

(a) β-function for 18Ni(300) Maraging Steel.

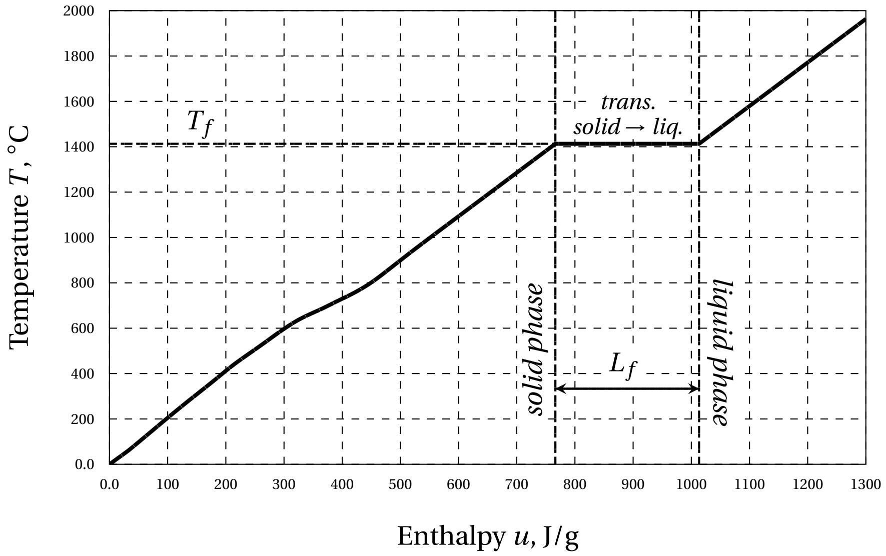

(b) β-function for 18Ni(300) Maraging Steel (zoom of the grey region).

Figure 3.3 – β-function for 18Ni(300) Maraging Steel.

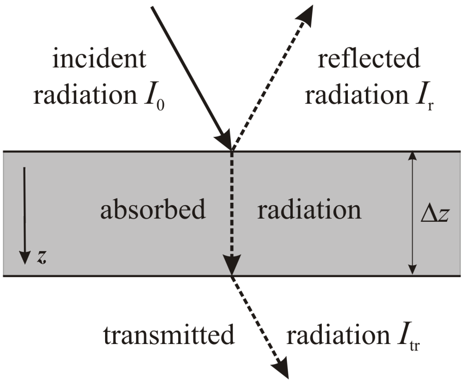

Figure 3.4 – Radiation reflection, transmission and absorption.

During propagation in the medium, the non-reflected radiation is partially absorbed by the material. In the case of a plane electromagnetic wave, propagating in a homogeneous medium along direction z, perpendicular to the medium surface, the radiation intensity decay according to Beer-Lambert law. The intensity of the transmitted radiation at a distance z from the material layer surface (see Fig. 3.4) is:

$$I_{\text{tr}}(z) = \alpha I_0 e^{-z/\delta}, \tag{3.4}$$

where δ is the *optical penetration depth* of the material, I_0 – the incident intensity and α – the surface absorptivity (see (3.2)–(3.3))

If the incident radiation is not a plane wave but a Gaussian beam (TEM$_{00}$) the law (3.4) generalizes under some conditions [52]. These conditions are:

(i) the material surface corresponds the waist plane of the beam;

(ii) the distance z is relatively small compared to the beam radius ω:

$$z \ll k_\lambda \omega^2, \tag{3.5}$$

where $k_\lambda = 2\pi/\lambda$ is the wave number, λ – the laser wavelength.

In such a situation, one may write:

$$I_{\text{tr}}(x, y, z) \simeq \alpha I_0(x, y) e^{-z/\delta} \tag{3.6}$$

with $I_0(x, y)$, the incident gaussian beam intensity at location (x, y) on the top surface (Fig. 3.4). Equation (3.6) is known as the paraxial approximation of the gaussian beam.

In the case we study $\lambda = 1070$ nm, $\omega = 40\ \mu$m (see Tab. 3.4), and the condition (3.5) for the paraxial approximation is: $z \ll 9.3$ mm. Therefore for powder layers up to several hundreds microns thick the propagation of the gaussian beam can be described by (3.6).

The optical penetration depth is a measure of light propagation in the material. It is defined as the depth at which the radiation intensity inside the material falls to $1/e$ of its original value at the surface. Generally, for bulk metals, the optical penetration depth is of the order of tens of nanometers [53]. As we can see from (3.4), if the optical penetration depth is small compare to the thickness of the material $\delta \ll \Delta z$, we can neglect the transmitted part of the radiation I_{tr}.

The incident radiation falling onto a powder bed is not only partially absorbed by the outer surface but also penetrates through the pores due to multiple reflections. For metallic powders with grain size of $10-20\ \mu$m, δ is of the order of several powder particle diameters [54]. Therefore in laser sintering/melting of a powder layer with a thickness less than hundred microns, the penetration depth plays an important role in laser energy deposition. The influence of δ increases for highly reflective metallic powders [43].

Estimation of the parameters of laser energy deposition onto a powder bed was an objective of many studies [7, 17, 41, 43, 55, 56]. The principal question, arising with regard to the radiation transfer during laser treatment of powders, is the influence of the wavelength, material, particle size, packing structure and density. The subject was studied experimentally [56], by ray-tracing modeling [7, 43] and by solving the radiation transfer equation (RTE) [41].

Several techniques for measuring powder absorptivity/reflectivity currently exist [56, 57, 58]. One of the most reliable methods was applied by N.K. Tolochko (so-called radiometric technique). He used an integrating sphere for direct measurement of a powder absorptivity.

The radiometric technique was applied in LGPP for 18Ni(300) Maraging Steel powder [59]. Experiments showed that the effective absorptivity of the powder is quite high compare to the absorptivity of the bulk material: $\alpha_p^{\mathrm{exp}} = 0.7-0.8$.

These experimental results are confirmed by the solution of the radiation transfer equation (RTE), which was performed by A.V. Gusarov in [41]. In his method he applies the *statistical scattering model* to a powder bed. In the model radiative properties in packed powder beds of non-spherical particles with arbitrary orientation (statistically isotropic powder bed) are expressed as the properties of packed beds of spherical particles with the same porosity and specific surface.

According to the Gusarov's solution of RTE the effective absorptivity of 18Ni(300) Maraging Steel powder bed is in the range $\alpha_p^{\mathrm{theor}} = 0.78-0.88$. This theoretical estimation is in good correspondence with the results obtained by means of the integrating sphere α_p^{exp}. In our simulation we will use the value $\alpha_p = 0.8$ for the effective absorptivity of 18Ni(300) Maraging Steel powder.

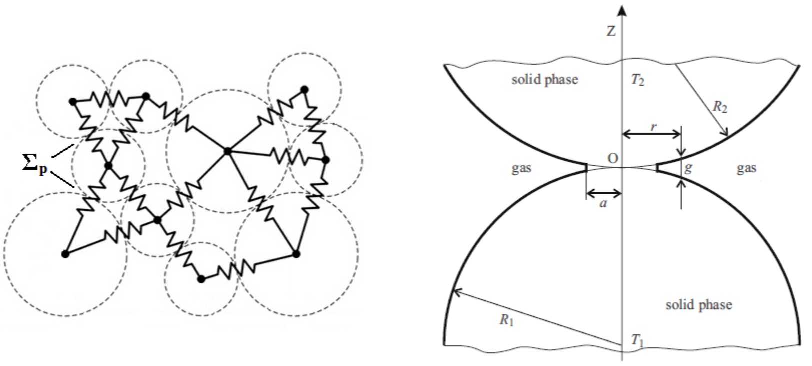

Figure 3.5 – Discrete thermal resistances model for powder beds by A.V. Gusarov (pic. [3]).

Experiments for the definition of the optical penetration depth were also performed by means of the integrating sphere [59, 60]. According to the results, the penetration depth of 18Ni(300) Maraging Steel loose powder is $\delta \simeq 20\ \mu$m.

3.3.2 Powder density

The value of 18Ni(300) Maraging Steel powder density ρ_p can vary from 50% to 70% of the density ρ_s of the solid material. In most of our simulations we will consider the case of a very loose powder: we assume that the powder density ρ_p is 50% of the density of the bulk material $\rho_p = 0.5\rho_s = 0.004$ g/mm^3 (see Tab. 3.2).

3.3.3 Effective thermal conductivity

In the framework of the homogeneous medium hypothesis we usually use the concept of effective thermal conductivity for powders. The effective thermal conductivity relates to a certain volume (greater than the size of inhomogeneity) of the material and describes the heat conduction of this volume as a whole. A powder bed is considered as a multiphase heterogeneous medium, where the solid particles are dispersed in a continuous gas phase in such a way that they can touch each other and form point contacts between them. Therefore, the effective thermal conductivity of a powder depends both on the properties of the solid and of the gas phases.

The model of effective thermal conductivity developed by A.V. Gusarov [3] takes into account all the types of thermal interaction between particles in powder and packed beds. This model, applied to packed equal spheres, estimates the effective thermal conductivity as a function of the volume fraction of solid f_s, the mean coordination number N, and the thermal resistance of a contact between two neighbouring particles Σ_p.

Powder type	d_0	f_s	k_p (eq.(3.7))	k_p (exp.)
18Ni(300) Maraging Steel	8.87 μm	50 – 55%	0.0982 W/m/°C	0.0847 W/m/°C
Commercially Pure Silver	5 μm	60%	0.0857 W/m/°C	0.0949 W/m/°C

Table 3.3 – Thermal conductivity of powders in air at normal conditions: theoretical prediction and experimental results.

The contact resistance Σ_p depends on four dimensionless parameters: the relative size of the contact r_c/r_0 between powder grains, the ratio of thermal conductivities of the solid and gas phases k_s/k_g, the Knudsen number Kn, and the adiabatic exponent of the gas phase γ_a.

If the particles of an heterogeneous medium form only point contacts (as in the case of loose powders), the heat flux through the solid phase is negligible and the heat transfer is performed through the gas gap between powder particles.

For point contacts $r_c \simeq 0$, at high k_s/k_g, as it is in a powder bed:

$$\begin{aligned} \frac{k_p}{k_g} &= \frac{f_s N}{2}\left[\frac{1}{2}\ln(1+L)+\ln(1+\sqrt{L})+\frac{1}{1+\sqrt{L}}-1\right] \\ L &= \frac{3}{4\sqrt{\pi}\mathrm{Kn}}\frac{\gamma_a+1}{9\gamma_a-5}, \quad \mathrm{Kn}=l_0/d_0, \end{aligned} \tag{3.7}$$

where l_0 is a gas mean-free path, d_0 - powder grain diameter.

In this study k is the notation of the *effective* thermal conductivity of the material. In order to denote the effective thermal conductivities of the powder and of the solid material we use k_p and k_s, respectively.

For the validation of the theory, described above, an experimental setup for powder conductivity measurements, based on the classical flash method [61], was developed [59]. The first experimental results for several powder types are presented in Tab. 3.3. They are compared to theoretical prediction of Gusarov's theory for point contacts (3.7).

In the theoretical estimation of the effective thermal conductivity of powders we assume that air plays the role of the gas phase between powder particles: $\gamma_a = 7/5$, k_g= 0.026 W/m/°C, $l_0 = 58$ nm [3]. The coordination number $N = 5.57$ corresponds to a randomly packed powder bed (see [62]).

The results in Tab. 3.3 show that the effective thermal conductivity of a powder is of the order of several times the conductivity of air and depends on the particles diameter. One can see good correlation between theory and practice for maraging steel and pure silver powders.

In the simulation we will use the value $k_p = 0.1$ W/m/°C for the effective thermal conductivity of 18Ni(300) Maraging Steel powder.

3.4 Molten material properties

In this study we assume that the thermal conductivity k_l of the liquid 18Ni(300) Maraging Steel is similar to the value k_s for the solid material and is not dependent on temperature. According to [63], the thermal expansion coefficient for different grades of steels at the melting point does not exceed $2 \cdot 10^{-5}$ 1/°C. Therefore the density ρ_l of molten 18Ni(300) Maraging Steel is approximately equal to the density ρ_s of the solid material. However the same assumption cannot be made for the material surface absorptivity, which evolves significantly during melting.

According to [56, 64, 65] absorptivity of a flat solid stainless steel surface for a wavelength close to 1 μm at the room temperature is in the range $0.4 - 0.6$, depending on the roughness of the surface. Whereas the surface absorptivity of liquid steel can vary from 0.1 to 0.3 for the same wavelength [64, 65].

In this work we choose the values $\alpha_l = 0.2$ and $\alpha_s = 0.5$ for the surface absorptivity of molten and solid 18Ni(300) Maraging Steel, respectively.

Remark 3.1. *Actually the surface absorptivity of molten steel strongly depends on its chemical composition and on the interaction with the surrounding atmosphere. For example, oxidation of the liquid material surface can cause a significant increase of absorptivity: up to 0.7, according to [64, 66]. However in this study we assume that the surface oxidation is negligible. This assumption is justified since the SLS/SLM process is performed under a protective atmosphere (argon Ar).*

Laser wavelength λ	1070 nm
Laser beam profile	top-hat/gaussian
Laser beam radius ω	40 μm
Laser power P	100; 200; 300 W
Scanning speed v	1; 2; 3 m/s

Table 3.4 – Process parameters used in the study.

3.5 Operation parameters used for Maraging Steel Powder

The typical process parameters, used in this study, are presented in Tab. 3.4. We have chosen them in accordance with modern industrial requirements (see Chapter 2). The parameters form 9 sets (see Tab. 3.5). However some of them will not give good results for the chosen laser and material parameters. We will discuss it in next chapters.

The choice of the scanning strategy and of the dimensions of the powder layer will be discussed in each chapter separately.

Set No.	Power/speed, W/(m/s)
1	100/1
2	100/2
3	100/3
4	200/1
5	200/2
6	200/3
7	300/1
8	300/2
9	300/3

Table 3.5 – Sets of the process parameters used in simulation.

Parameter	Powder bed	Solid material	Liquid material
Grain radius r_0	4.435 μm	–	–
Optical penetration depth δ	20 μm	–	–
Absorptivity α	0.8	0.5	0.2
Thermal conductivity k	0.1 W/m/°C	26 W/m/°C	26 W/m/°C
Density ρ	0.004 g/mm^3	0.008 g/mm^3	0.008 g/mm^3

Table 3.6 – Properties of 18Ni(300) Maraging Steel.

3.6 Conclusions

Tab. 3.6 summarizes the properties of 18Ni(300) Maraging Steel powder, solid and liquid material, which we will use in the study.

It can be seen that, during sintering/melting of 18Ni(300) Maraging Steel, the thermal conductivity and the absorptivity of the material change drastically. Thermal conductivity of the powder is of the order of several times the conductivity of air but it is less than 1% of the conductivity of bulk material. At the same time the liquid material (as all liquid metals) is highly reflective, while the powder bed effectively absorbs laser energy. In the next chapters, we will discuss the influence of these phenomena on the SLS/SLM process.

Observe that such a significant change in the properties due to melting is typical for the majority of metallic powders used in SLS/SLM.

4 Single Grain Model

In this Chapter we consider the mechanisms of heating and melting of a separate and perfectly spherical powder grain irradiated by a plane electromagnetic wave. This theory is often called Single Grain Model (SGM) [38, 67]. We improve the existing model by considering the real intensity distribution instead of the homogeneous one and by taking the finite thermal conductivity of a powder particle into account.

The main outputs of the Single Grain Model will be:

- an estimation of the melting time of a grain;
- a relatively precise information about the evolution of the average temperature inside a grain.

These results will be used later on to build the reliable consolidation model we need to integrate into the macroscopic description of the SLS/SLM process.

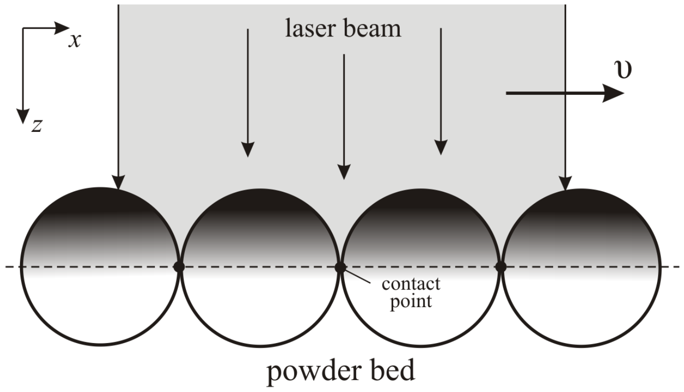

Figure 4.1 – Irradiation of the surface of a powder bed by a moving laser.

4.1 Single Grain Model: main assumptions

Evolution of the effective parameters of a powder bed depends on the melting dynamics of powder grains and their interaction and rearrangement. A Single Grain Model allows to study the process of melting of a separate powder grain on the surface of a powder bed during laser heating. Knowing the melting behavior of a single grain we can better understand the evolution mechanisms of powder properties during laser sintering/melting.

The Single Grain Model considers powder-laser interaction at a scale of a powder grain size. The grain is assumed to be spherical and there is no influence of the neighbouring grains.

Remark 4.1. *In [38, 67] the grain was assumed to be homogeneously irradiated all over its surface. Since homogeneous irradiation is difficult to justify, in this study we consider that the powder particle interacts with a monochromatic polarized plane wave (see Fig. 4.1), which is a rough approximation of a top-hat/gaussian laser beam. However we will keep the name 'Single Grain Model' for this theory.*

In a plane electromagnetic wave, linearly polarized in the direction of x-axis and propagating in the void along z-axis (see Fig. 4.1), the electric field at a moment of time $t = 0$ in a point (x, y, z) is:

$$\mathbf{E}(x,y,z,t) = \mathbf{E}_0 e^{-i(k_\lambda z - \omega_f t)} = E_0 e^{-i(k_\lambda z - \omega_f t)} \mathbf{e}_x. \tag{4.1}$$

The wave is characterized by its electric amplitude $\mathbf{E}_0$, the wave number $k_\lambda = 2\pi/\lambda$ and the angular frequency $\omega_f = k_\lambda c$ with c the speed of the light.

Laser wavelength λ	1070 nm
Laser beam radius ω	40 μm
Laser beam profile	top-hat/gaussian
Radius of the grain r_0	4.435 μm
Density ρ_s	0.008 g/mm^3
Thermal conductivity k_s	0.026 W/mm/°C
Dielectric constant $\varepsilon_R + i\varepsilon_I$	$(3.24 - i4.34)^2$
Latent heat of fusion L_f	247 J/g

Table 4.1 – Properties of the laser and of a typical 18Ni(300) Maraging Steel powder grain.

4.1.1 Intensity of the plane wave and laser power

An important characteristic of an electromagnetic plane wave is its time-average intensity I_0. This field proves to be constant in space and oriented in the direction of the wave propagation:

$$\mathbf{I}_0(x, y, z) = I_0 \mathbf{e}_z. \tag{4.2}$$

For the plane wave (4.1), the connection between I_0 and the electric amplitude is:

$$I_0 = \frac{k_\lambda}{2\mu_p \omega_f} E_0^2, \tag{4.3}$$

where $\mu_p = 4\pi \cdot 10^{-7}$ N/A^2 is the vacuum magnetic permeability.

In the Single Grain Model the plane wave we select to approach the laser beam, has a time-average intensity I_0 equal to the maximum laser beam intensity:

$$I_0 = \frac{P}{\pi\omega^2}. \tag{4.4}$$

for the top-hat or gaussian beam. We use the expression (4.4) both for the top-hat and gaussian beam, as far as we assume that powder particles we are interested in, i.e. the particles which are molten, are situated in the center of the laser beam.

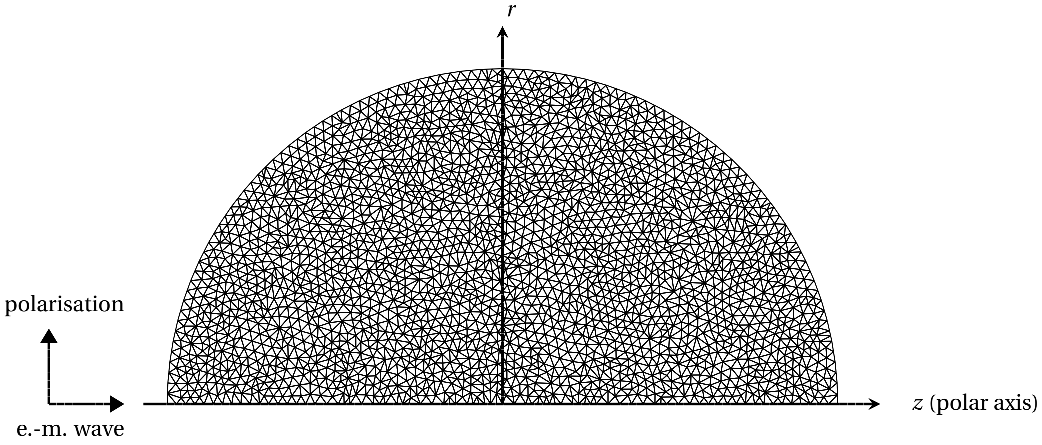

Figure 4.2 – Meshing of a 2D domain for the Single Grain Model calculations.

4.1.2 Heating of a spherical grain with a plane wave

The heating by a plane electromagnetic wave of amplitude $\mathbf{E}_0$ of a non-magnetic spherical particle with a complex dielectric constant $\varepsilon_d = \varepsilon_R + i\varepsilon_I$, can be described by Mie theory [68]. It allows to express the electric field, transmitted to the sphere, in the form:

$$\mathbf{E} = \|\mathbf{E}_0\|\mathbf{e}, \tag{4.5}$$

where **e** is the field transmitted for an incident wave with unit electric amplitude.

Using Mie solution of Maxwell equations, we can calculate the heat source q induced by Joule heating in the irradiated powder grain. It is proportional to the intensity I_0:

$$q = \frac{1}{\delta} I_0 \parallel \mathbf{e} \parallel^2 . \tag{4.6}$$

The factor

$$\delta = -\frac{1}{\varepsilon_I k_\lambda} \tag{4.7}$$

in (4.6) has the dimension of a length and corresponds to the optical penetration depth of the grain.

As we discussed in § 3.3.1 of Chapter 3, penetration depths of bulk metals are relatively small (tens of nanometers) compare to the radius of the grain ($r_0 = 4.435\ \mu$m). Therefore the volume source (4.6) is concentrated near its surface and a finite element simulation of the heating process would require a very fine meshing of the grain. The classical solution to avoid this issue is to replace the volume heat source (4.6) by an equivalent surface heat source q_{surf}:

$$q_{\text{surf}} = -I_0 \mathbf{n} \cdot \mathbf{s_t}. \tag{4.8}$$

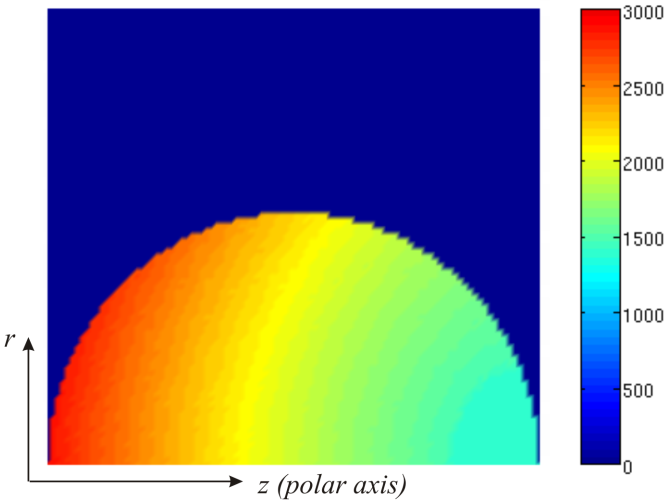

Figure 4.3 – Temperature distribution inside a spherical grain after 6 μs of irradiation by the plane wave with the intensity corresponding to the 100 W laser (Tab. 4.1).

In (4.8) $\mathbf{s_t}$ denotes the Poynting vector, transmitted to the sphere in the case of an incident plane wave with unit intensity.

In the case of a linearly polarized wave, the heat source has a simple dependency with respect to the polar angle φ (Fig. 4.2). If the polar axis is aligned with the direction of wave propagation (z-axis in our case), we can write that:

$$q_{\text{surf}}(r,z,\varphi) = I_0(b_0(r,z) + b_1(r,z)\cos 2\varphi), \tag{4.9}$$

where (r,z,φ) are the cylindrical coordinates and where b_0 and b_1 are functions of r and z only. The coefficients b_0 and b_1 can be calculated numerically by means of a simulation tool [69].

4.2 Melting of a powder grain

Using the theory presented above, we can model numerically the melting process of a separate spherical powder grain of radius r_0 irradiated by a laser beam of intensity I_0. The properties of the grain correspond to a typical particle in a 18Ni(300) Maraging Steel powder bed. They are listed in Tab. 4.1. The dielectric constant ε_d corresponds to the value for steel [53].

The mesh used to discretize the grain surface is presented in Fig. 4.2 in polar symmetry. In this context we can study the evolution of the temperature field in the particle and its melting during irradiation with a standard finite element method.

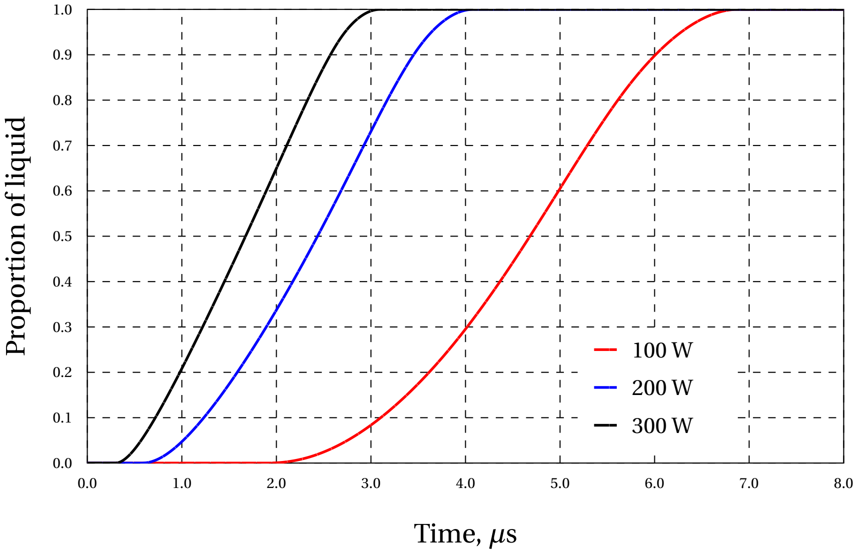

Figure 4.4 – Evolution of molten material proportion during grain melting by a plane wave of different intensities approaching laser beam with power 100 W, 200 W, 300 W.

Fig. 4.3 presents the temperature distribution inside a typical Maraging Steel powder grain after 6 μs of irradiation by a plane wave (λ = 1070 nm) approaching a laser beam with 100 W power (for the detailed laser and grain properties see Tab. 4.1).

Different simulations are performed for plane wave intensities corresponding to laser powers 100 W, 200 W and 300 W. The latent heat of fusion L_f is taken into account (see Tab. 4.1).

Evolution of the proportion of molten material during melting for these parameters is shown in Fig. 4.4. As it can be seen from this graph, the grain, irradiated by the plane wave, is not molten immediately.

We can calculate the time necessary to initiate melting from the beginning of the grain irradiation by the wave. We denote this time as t^s ('solidus'). We also estimate the time t^l ('liquidus'), after which the grain is completely molten. Results for the intensities, corresponding to the chosen laser powers, are presented in Tab. 4.2.

Laser power P	Wave intensity I_0 (4.4)	t^s	t^l	$t^i_{\max}$
100 W	19894 W/mm^2	1.84 μs	6.88 μs	24 – 71 μs
200 W	39789 W/mm^2	0.54 μs	4.08 μs	24 – 71 μs
300 W	59683 W/mm^2	0.26 μs	3.1 μs	24 – 71 μs

Table 4.2 – Single Grain Model. (i) t^s: start of the grain melting (Tab. 4.1); (ii) t^l: complete grain melting; (iii) $t^i_{\max}$: maximum time of grain irradiation (Fig. 4.5).

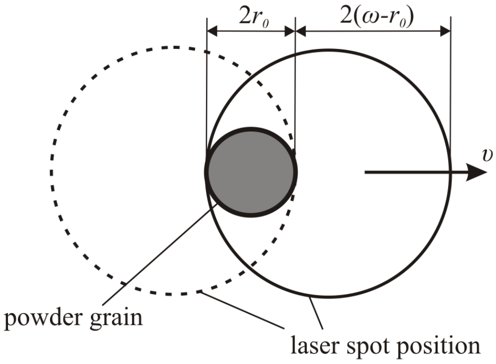

Figure 4.5 – Maximum irradiation of a powder grain by a top-hat laser beam.

From Tab. 4.2 it can be concluded, that for the selected parameters the melting of a typical 18Ni(300) Maraging Steel powder grain starts in a period of time less than 2 μs, and the particle is completely molten after $3-5$ μs.

In Tab. 4.2 the values of t^s and t^l are compared to the maximum time of grain irradiation $t^i_{\max}$. To define this time we go back to the system 'powder-laser'. Consider a top-hat laser beam of radius ω, travelling with a speed v and irradiating a powder bed. We assume that the powder bed consists of equally spherical particles of radius r_0. The maximum time while a powder grain can be located entirely within the border of the laser spot (see Fig. 4.5) is:

$$t^i_{\max} = 2(\omega - r_0)/v. \tag{4.10}$$

According to (4.10), for laser scanning speeds $1-3$ m/s, $t^i_{\max}$ is $24-71$ μs (Tab. 4.2).

From Tab. 4.2 we can see, that the time of the particle complete melting is several times less than its irradiation time by the laser.

4.3 Evolution of powder bed properties

We have shown before, that the irradiation of a powder grain by a plane wave is not homogeneous. The example of the temperature gradient inside the grain can be seen in Fig. 4.3. From this picture it is clear that when a part of the grain is already molten, a part of it still stays solid.

At the level of a powder bed, when a powder grain begins to melt, the molten material starts to form necks with the neighbouring particles. As it is shown in [1], at the first moment necks between particles are small and unstable, while during further laser irradiation they are merging and growing. Formation of stable interparticular necks between powder grains can be considered as a starting point of the evolution of the effective properties (absorptivity, thermal conductivity) of the powder bed.

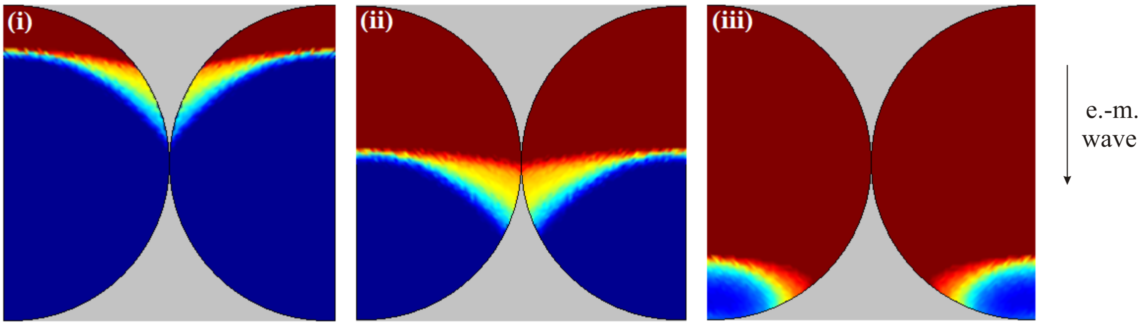

Figure 4.6 – Evolution of the proportion of the molten material during irradiation of two neighbouring grains: (i) $t < t^0$; (ii) $t \simeq t^0$, (iii) $t > t^0$.

To connect the melting of a separate powder grain to the properties of a powder bed, i.e. to link the Single Grain Model to the homogeneous medium hypothesis, commonly used for SLS/SLM simulation (see Chapter 6 for details), we will estimate the evolution of the average temperature of the grain during its melting by a plane wave.

We need to define the moment when a neck starts to form between two neighbouring powder grains. For this purpose we will make some assumptions on the irradiated powder bed:

- Surface of the powder bed is perfectly 'flat', i.e. the centers of powder grains in the surface layer of the powder are situated in the same horizontal plane.
- Two neighbouring grains on the surface of the powder bed are irradiated in the same way by the laser.
- Back-scattering of laser irradiation by powder grains is not taken into account.
- Heat transfer between the grains during their melting is not taken into account.

The position of a contact point between two neighbouring grains is shown in Fig. 4.1. During laser irradiation of the grains, the time t^0, when the melt front reaches the contact point, can be considered as the time of the neck-forming, i.e. when powder bed properties evolution starts.

We use the Single Grain Model to estimate the value of t^0. We study the temperature evolution in a point on the surface of a spherical particle, irradiated by a plane wave. The particle is made of 18Ni(300) Maraging Steel (see properties in Tabs. 4.1 and 3.6), and the point we consider is a contact point to a neighbouring particle (see Fig. 4.1).

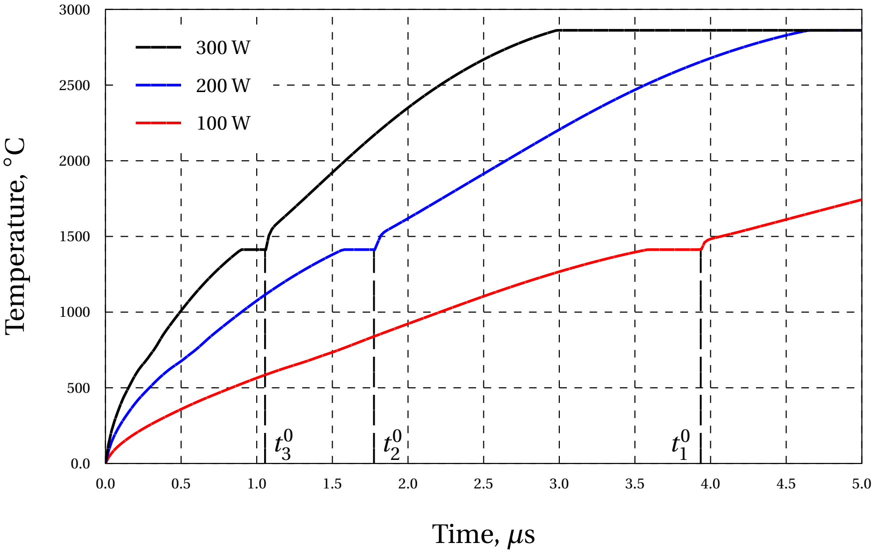

Figure 4.7 – Temperature evolution in the contact point between two grains irradiated by a plane wave, approaching the laser of different powers.

The intensities of the plane are adapted to approach a top-hat laser beam with a radius 40 μm and powers 100 W, 200 W or 300 W (Tab. 4.3). The simulated temperature evolution is presented in Fig. 4.7. The time t^0, when the melt front reaches the contact point, is also shown on this figure and its exact value is presented in Tab. 4.3.

Fig. 4.6 presents the stages of the evolution of the molten material proportion during laser irradiation of two neighbouring grains on the surface of a powder bed. As we can see, at the moment, when the melt front reaches the contact point between the particles, part of each particle still stays solid. To connect these results to the homogeneous medium model, we will estimate the average temperature of the grains T_{av}^0 at the moment t^0.

In Fig. 4.8 one can observe the evolution of the average temperature of the grains T_{av}^0 during their irradiation with a plane wave. The exact values of T_{av}^0 for the chosen intensities/powers are presented in Tab. 4.3.

Laser power P	Wave intensity I_0 (4.4)	C. p. melt time t^0	Av. temp. T_{av}^0
100 W	19894 W/mm^2	3.92 μs	1353 °C
200 W	39789 W/mm^2	1.76 μs	1213 °C
300 W	59683 W/mm^2	1.04 μs	1089 °C

Table 4.3 – Melting time t^0 of the contact point between two grains, irradiated by a plane wave of intensity I_0, and the average temperature T_{av}^0 of the grains at this moment.

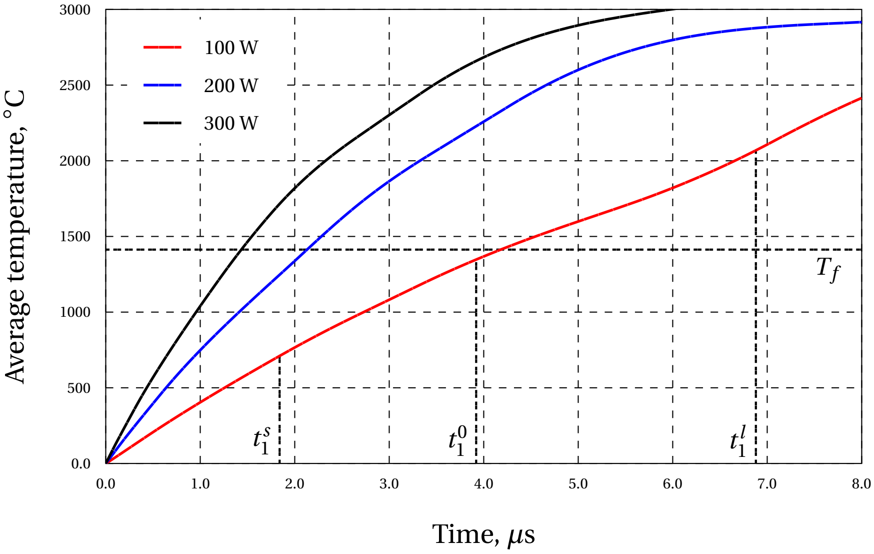

Figure 4.8 – Evolution of the average temperature of a powder grain (Tab. 4.1), irradiated by a plane wave, approaching the laser of different powers.

As it can be seen from Tab. 4.3, for the selected parameters, the melt front reaches the contact point, when the average temperature of the grain T_{av}^0 is less than the melting point $T_f = 1413$°C of the material.

It has to be observed on Fig. 4.8 that the time dependency of the average temperature of the grain T_{av}^0, heated by a plane wave, is not linear. The non-linearity is mostly explained by the phase transition. For example, if we look at the curve, corresponding to a laser power of 100 W, we see that the non-linear part is enclosed between $t_1^s = 1.84$ μs and $t_1^l = 6.88$ μs. These values correspond to the moments when the grain starts to melt and when it is completely molten, respectively (see Tab. 4.2).

Outside the interval (t^s, t^l), T_{av} depends almost linearly on time. Since we neglect losses for the surface of the grain, the slope of the graph is given by the ratio between the absorbed power and the (almost constant) thermal mass of the grain M_{th}

$$M_{\text{th}} = \frac{4}{3}\pi r_0^3 \rho_s C_p. \tag{4.11}$$

In this formula C_p is the heat capacity of 18Ni(300) Maraging Steel: $C_p \simeq 0.5$ J/g/°C for any temperature (see Fig. 3.3).

4.4 Different powder grain sizes

Fig. 3.1 shows, that the particles in the 18Ni(300) Maraging Steel powder we study are actually not of the same size. It is therefore important to discuss the value of the time to contact point melting t^0 and the average temperature T^0_{av} for different radii of powder grains. According to Fig. 3.1, besides $r_0 = 4.435$ μm, we chose values 2.5 μm and 10 μm.

Fig. 4.9a presents the values of time t^0 for the grains of the three chosen radii, irradiated by a plane wave, approaching a laser beam of waist 40 μm. We select laser power range from 50 W to 400 W.

It can be seen from Fig. 4.9a, that for the laser powers $100-300$ W, even for the maximum value of the grain radius (10 μm), the time t^0 is always less than 10 μs. As we already did before, we are going to estimate the average temperature T^0_{av} of the grains at the moment of time t^0. The results are shown in Fig. 4.9b.

From Fig. 4.9b one can observe, that for laser powers between 100 and 400 W, the average temperature of two neighbouring grains stays significantly below the melting temperature T_f at the moment when they start to be connected by a neck. For higher laser powers the surface melting of a particle is faster, therefore the average temperature of the grain at the moment, when powder sintering begins, will even be lower.

In the chosen range of the process (Tab. 3.4) and material (Tab. 3.6) parameters, the conclusion is that the homogenized temperature, at which sintering process starts, is significantly lower, than the melting point T_f of the material.

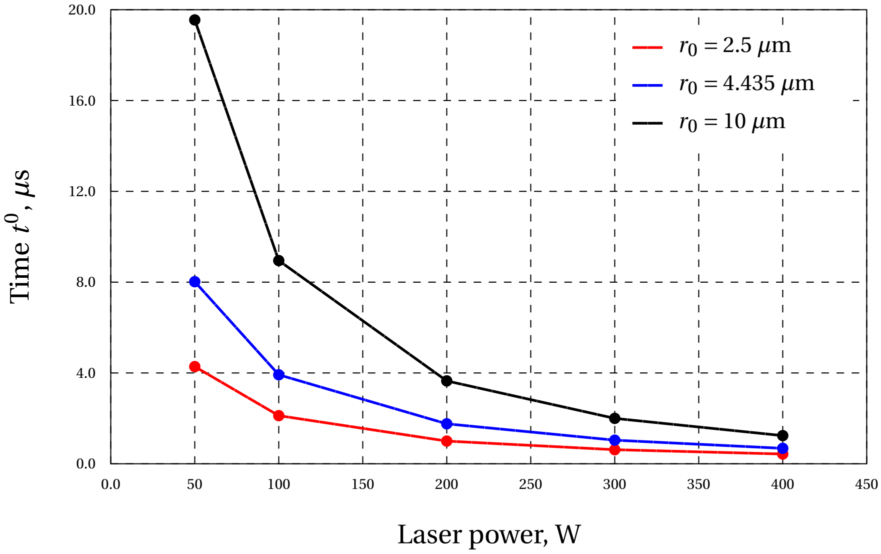

(a) Time to the contact spot melting t^0 between two equal spherical grains for different grain radii r_0.

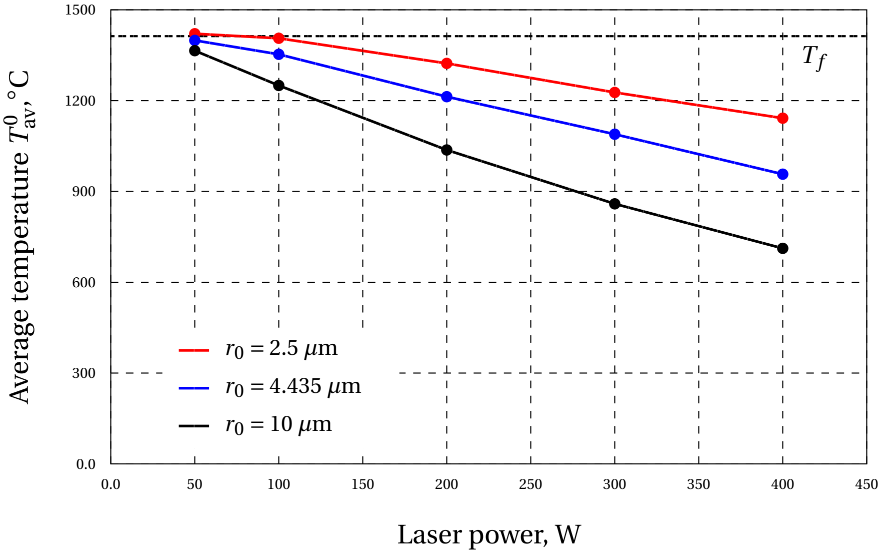

(b) Average temperature T^0_{av} of a powder grain at the moment t^0 for different grain radii r_0.

Figure 4.9 – Single Grain Model: Time to the contact spot melting t^0 and average temperature T^0_{av} of the powder grain at the moment t^0.

4.5 Conclusions

In this chapter we considered the melting process of a separate particle in the surface layer of a powder bed. The Single Grain Model has been applied for the particular case of a standard 18Ni(300) Maraging Steel powder (Tab. 3.6). For typical process parameters (Tab. 3.4) the following results have been obtained:

(i) Heating and complete melting of a powder grain on the surface of a powder bed under a laser takes less than 10 μs from the beginning of the irradiation. For the chosen parameters this time equals to $14-40\%$ of the maximum irradiation time.

(ii) The time, when the melt front reaches the contact point between two similarly irradiated neighbouring powder grains on the surface layer of the powder bed, can be considered as the start of neck-forming and the beginning of the evolution of powder bed effective parameters. In our case, this process starts less than 4 μs after the beginning of the irradiation. This delay is between $5-16\%$ of the maximum irradiation time.

(iii) The average temperature of a grain at the moment, when it is molten enough to form a neck with its neighbour, is less than the melting temperature T_f of the material. It can be said that evolution of the properties of the surface of a powder bed during laser scanning, *at the scale of powder grain size*, starts before the moment when the homogenized temperature reaches the value T_f. For the chosen range of laser power ($100-300$ W) the evolution process starts at an average temperature of $1000-1300$°C. However this threshold value depends on laser power and powder material.

5 Melting Dynamics

As we already discussed in Chapter 4, in SLS/SLM when powder grains, irradiated by a laser, start to melt, the molten material forms necks between them. The formation of necks is caused by the action of capillary forces and strongly depends on dynamic viscosity and surface tension of the liquid phase. The process of neck-forming between powder grains defines the evolution of effective powder properties during laser sintering.

In this Chapter we study capillary parameters of 18Ni(300) Maraging Steel under SLM conditions and their influence on the sintering process. We also discuss the mechanisms of interconnection of powder grains during their melting. We propose a model which considers the interaction of molten powder particles as a coalescence of liquid drops.

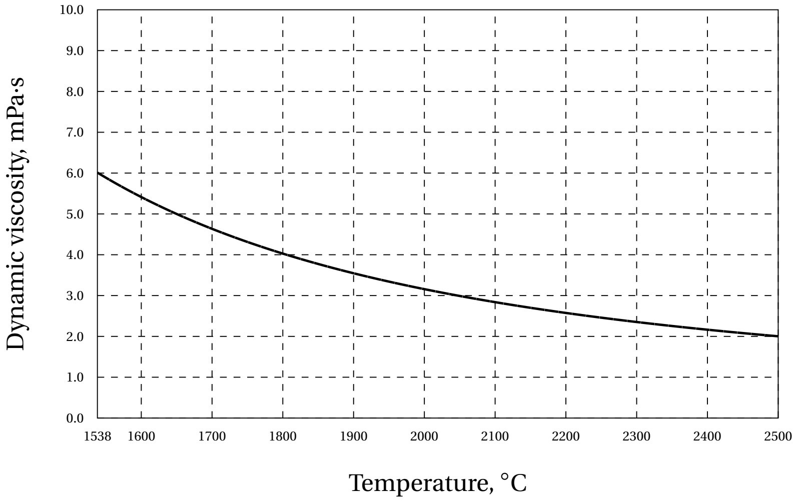

Figure 5.1 – The dynamic viscosity of pure liquid iron in the range of temperatures $1538°\mathrm{C} < T < 2500°\mathrm{C}$ [4].

5.1 Capillary properties of molten powder material

Rearrangement, interconnection and merging of powder particles during laser sintering/melting is driven by the capillary motion of the molten material. Description of the capillary flow of any material is based on its surface tension and dynamic viscosity. The capillary parameters are strongly dependent on the material properties and on the conditions of the melting process. In this Section, using 18Ni(300) Maraging Steel powder as an example, we discuss the main factors which can influence the capillary properties of a molten material during SLM of a metallic powder.

5.1.1 Dynamic viscosity

Viscosity is a property arising from collisions between neighbouring particles that are moving at different velocities. Dynamic viscosity of a liquid expresses its resistance to shearing flows. In this study we denote it as μ. Main factors influencing the dynamic viscosity are the chemical composition of the liquid and its temperature.

An empirical formula for the dynamic viscosity of a liquid metal which takes its chemical composition into account, is proposed in [70]. According to this paper, dynamic viscosities of different grades of liquid steel can vary from 6 to 20 mPa·s near the melting point of a material.

The Arrhenius equation is often used to describe the dependence on temperature of the dynamic viscosity of a liquid [71]:

$$\mu(T) = \mu_0 e^{E_a/R_g(T+273)}. \tag{5.1}$$

In (5.1) μ_0 is a coefficient, R_g= 8.314 J/mol/K is the universal gas constant and E_a is the activation energy. It corresponds to the potential energy barrier for the movement of an atom created by the nearest atoms in the liquid.

In [4] the coefficient μ_0 and the activation energy E_a are found empirically for liquid iron in the range of temperatures 1538°C < T < 2500°C:

$$\mu_0 = 0.253 \text{ mPa·s}, \quad E_a = 47.7 \text{ kJ/mol}. \tag{5.2}$$

In Fig. 5.1 we can observe the dependence of the dynamic viscosity μ of liquid pure iron on temperature T in the range 1538°C < T < 2500°C. The first value of this range is the melting point of iron. It can be seen, that the dynamic viscosity strongly depends on temperature and decreases significantly (from about 6 to 2 mPa·s) with temperature increase, which can influence interconnection and rearrangement processes of powder particles during SLM. We will discuss this question in this Chapter.

5.1.2 Surface tension

The surface tension of a fluid is a direct measure of the intermolecular forces acting at the surface and can be defined as the force per unit length acting parallel to the free surface. Data are sometimes expressed in terms of free surface energy, because surface tension also represents the free energy per unit surface. In this work the surface tension of the liquid-gas interface will be denoted as γ.

The surface tension of pure liquid metals depends on the strength of the cohesive forces acting between neighbouring atoms, and it can be related to physicochemical properties of the material. The principal parameters affecting the surface tension of a liquid-gas interface are the chemical composition of the liquid and the gas, the temperature and the chemical reactions with a surrounding atmosphere. However, in this study, it will be assumed that the molten material does not react with the protective atmosphere under which SLM process is performed.

In a first approximation, the influence of the temperature of a liquid on its surface tension can be described by a linear law [72]:

$$\gamma(T) = \gamma_f + \gamma'(T - T_f). \tag{5.3}$$

In (5.3) γ_f is the surface tension of the metal at the fusion point T_f and $\gamma' = \mathrm{d}\gamma/\mathrm{d}T$ is so-called temperature coefficient of the surface tension.

In [72] γ' for pure liquid metals is calculated on the basis of the nearest-neighbour interaction-broken-bond model. The value $\gamma' = -0.23 \cdot 10^{-3}$ J/m^2/K for pure iron is obtained and confirmed experimentally.

Parameter	1538°C	2500°C
Surface tension γ	1.79 N/m	1.51 N/m
Dynamic viscosity μ	6 mPa·s	2 mPa·s
Density ρ_l	0.008 g/mm^3	0.008 g/mm^3

Table 5.1 – Properties of liquid 18Ni(300) Maraging Steel, used in Chapter 5.

We use $\gamma_f \simeq 1.79$ J/m^2 as the initial value of the surface tension in (5.3). It corresponds to the surface tension of liquid sulfur free stainless steel at temperature about 1500°C in a pure argon atmosphere [73].

One can see from (5.3), that for pure iron the temperature coefficient of the surface tension γ' is quite small. We will use the same range of temperature T as for the dynamic viscosity μ (Fig. 5.1): in the range 1538°C $< T <$ 2500°C the surface tension of liquid iron decreases only from 1.79 to 1.51 J/m^2.

The surface tension of a material also depends on its chemical composition. According to [73], the surface tension γ_f of steel at its melting point can vary from 1.6 to 1.9 J/m^2, depending on its chemical composition. For various types of steel the character of the dependence of the surface tension on temperature can also be different. However in [73] we observe a similar behavior (slight decrease while the temperature is increasing) for several grades of steel.

5.1.3 Summary

In Tab. 5.1 we summarized the parameters of 18Ni(300) Maraging Steel which will be used in this Chapter.

For the estimation of the temperature influence on the process of powder melting, we have chosen the range of temperatures 1538°C $< T <$ 2500°C. It approximately corresponds to the temperatures between the fusion point and the vaporization point of 18Ni(300) Maraging Steel: T_f = 1413°C, T_v = 2862°C. Using laws (5.1) and (5.3), we calculated the values of the surface tension and the dynamic viscosity for the minimum and maximum temperatures in this interval. We also assume that the density of the liquid material ρ_l does not depend on temperature (see § 3.4 of Chapter 3).

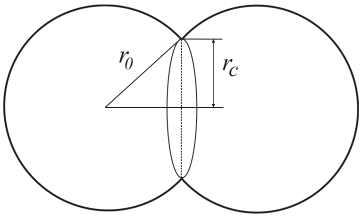

Figure 5.2 – Coalescence of two liquid drops.

5.2 Liquid drops coalescence model

When powder grains start to melt, they get connected by small necks [1]. Therefore contact points between powder particles are transformed to contact spots, which significantly changes heat transfer mechanisms in a powder bed.

In Chapter 4 we already discussed the starting time of effective powder bed properties evolution in the framework of the Single Grain Model. It was assumed that the neck-forming begins when the melt front in a powder grain, irradiated by a laser, reaches the point of contact with a neighbouring grain. We considered 18Ni(300) Maraging Steel powder and typical process parameters (Tabs. 3.5 and 4.1): laser powers 100 – 300 W, scanning speeds 1 – 3 m/s. We have shown that for typical powder particles ($r_0 = 4.435$ μm) the time when the neck starts to form, is 1 – 4 μs after the beginning of laser irradiation and that the particles are completely molten in 3 – 7 μs.

This theory gives us an idea of the order of magnitude for the molten material lifetime, during which necks form between grains. We believe that the neck-forming mechanism is essentially driven by capillary forces. To prove that gravity plays no role, we have to consider the Bond number [74]. It compares the surface tension to the gravitational forces:

$$\mathrm{Bo} = \frac{\Delta\rho g L_c^2}{\gamma}, \tag{5.4}$$

In (5.4) $\Delta\rho = \rho_l - \rho_{\mathrm{atm}}$ is the difference in densities of the liquid and gas phases, g – the gravitational acceleration, L_c – the characteristic length of the liquid volume, and γ is the liquid-gas surface tension. For a spherical liquid drop the characteristic length L_c is equal to the grain size $d_0 = 8.87$ μm. Argon is chosen as a gas phase: $\rho_{\mathrm{atm}} = 1.65 \cdot 10^{-6}$ g/mm^3. For 18Ni(300) Maraging Steel ($\rho_l = 0.008$ g/mm^3) the Bond number Bo is small:

$$\mathrm{Bo} \simeq 3.45 \cdot 10^{-6} \ll 1. \tag{5.5}$$

Drop radius r_0	Temperature T	Parameter K_2
2.5 μm	1538°C	0.55
4.435 μm	1538°C	0.58
4.435 μm	2500°C	0.66
10 μm	1538°C	0.6

Table 5.2 – Parameter K_2 (see eq.(5.7)) for different temperatures and radii of the drops [5].

Thus the behavior of a molten powder grain is driven by surface tension forces only: the gravitational forces are negligible and the molten grain keeps its spherical form in the absence of capillary interactions with neighbouring grains (or a substrate). Therefore we can assume that the interaction between two molten particles with an initial contact point between them can be described as a coalescence of two spherical drops.

Coalescence of liquid drops was studied by Frenkel [75]. He proposed a law for the time evolution of the contact radius r_c between two equal spherical liquid drops (Fig. 5.2):

$$r_c(t) = K_1 \left(\frac{r_0 \gamma}{\mu}\right)^{1/2} t^{1/2}, \tag{5.6}$$

where K_1 is a unitless geometry-dependent calibration coefficient, r_0 – the radius of the drop, γ and μ are the surface tension and the dynamic viscosity of the liquid material, respectively.

A similar law ($r_c \sim t^{1/2}$) was proposed in [76]. However it was only valid for the initial stage of the coalescence: $r_c \ll r_0$ (in [76] it was used for $r_c / r_0 < 0.03$).

Menchaca-Roca in [77] proposed a power law $r_c \sim t^{\alpha_0}$ for the description of the entire process (until $r_c \simeq r_0$): $\alpha_0 = 0.55$ for the beginning of the coalescence and $\alpha_0 = 0.41$ for larger neck radii between liquid drops.

Thoroddsen in [5] presented a differential equation describing the velocity of a neck growth between two equal spherical liquid drops:

$$\frac{\mathrm{d}r_c}{\mathrm{d}t} = \frac{K_2}{r_c}\sqrt{\frac{\gamma}{2\rho_l}}\left(r_0 - 2r_c + \sqrt{r_0^2 - r_c^2}\right)^{1/2}, \tag{5.7}$$

where K_2 is a unitless proportionality constant. The choice of K_2 depends on the value of $\rho_l r_0 \gamma / \mu^2$ (see [5] for the details), i.e. on the properties of the liquid and on the radii of the drops.

The surface tension γ, the dynamic viscosity μ and the density ρ_l of liquid 18Ni(300) Maraging Steel are listed in Tab. 5.1. According to these data we can set the values of the parameter K_2 for the Thoroddsen's equation. They are presented in Tab. 5.2.

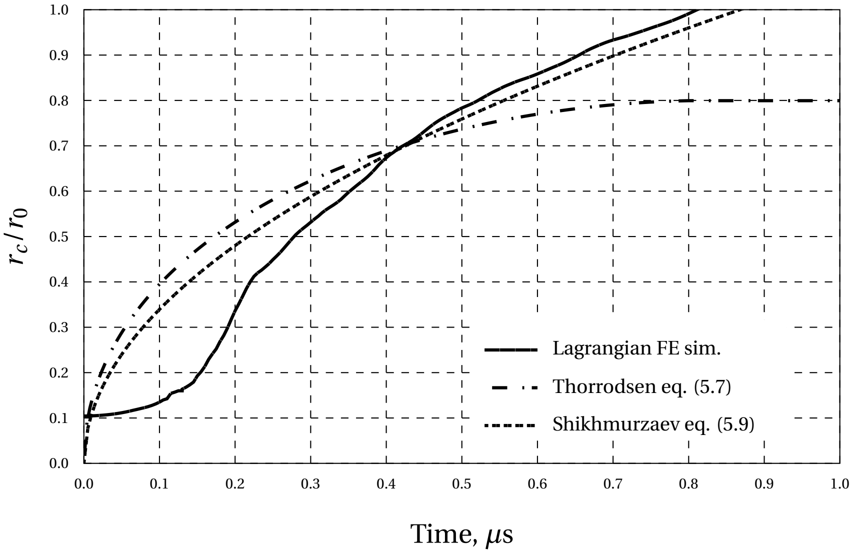

Figure 5.3 – Relative contact spot radius evolution: simulation and theoretical results, $r_0 = 4.435\ \mu$m

Remark 5.1. *Equation (5.7) is solved using MATLAB software with the initial condition for the contact spot radius*

$$r_c(0) = 10^{-3}\ \mu m, \tag{5.8}$$

$r_c(0) = 0$ *is not recommended due to the form of the right-hand side of (5.7).*

Later a similar power law for the evolution of a contact spot between two drops with initial point contact was obtained by Shikhmurzaev [78]:

$$r_c(t) = K_3 \left(\frac{2r_0\gamma}{\rho_l \tau_M} \right)^{1/2} t^{1/2}, \tag{5.9}$$

where τ_M – Maxwell relaxation time of the liquid. In the sequel we will use the Maxwell relaxation time of steel $\tau_M = 10^{-15}$ s [79]. In (5.9) K_3 is a phenomenological constant related to the inverse compressibility of the liquid. It is expressed with a unit of s/m.

The similarity of laws (5.6) and (5.9) seems to be promising, as far as they are based on different ideas: Frenkel (5.6) considers the coalescence of two drops from the energetic point of view, while Shikhmurzaev's hypothesis (5.9) is based on the motion of wetting lines and material fluxes from one interface to another through these lines. However (5.9) requires additional analysis of liquid material.

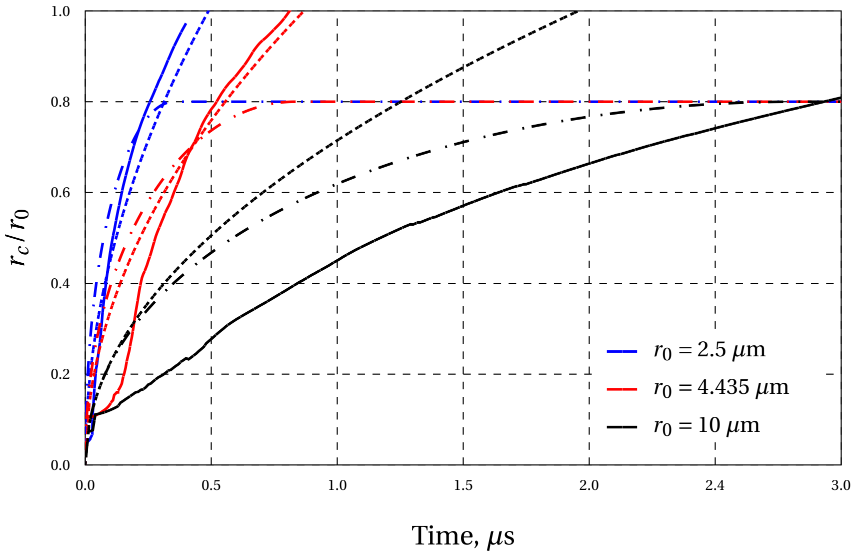

Figure 5.4 – Relative contact spot radius evolution for different radii of liquid drops: solid lines – LFEM, dashed lines – Shikhmurzaev's eq. (5.9) and Thorrodsen's eq. (5.7).

In order to estimate K_3 for the liquid parameters of liquid, presented in Tab. 5.1, coalescence of two drops was modelled by means of the Lagrangian finite element method (LFEM) [80]. Evolution of the relative contact radius r_c/r_0 in time, obtained numerically[1], can be seen in Fig. 5.3.

There is a clear possibility to fit the Shikhmurzaev law (5.9) with LFEM results at least for sufficiently large time t (see Fig. 5.3). In case of powder grains with radii $r_0 = 4.435\ \mu$m at melting temperature T_f the best fit is obtained for the value

$$K_3 \simeq 3.4 \cdot 10^{-6}\ \text{s/m} \tag{5.10}$$

of the Shikhmurzaev phenomenological constant.

In Fig. 5.3 we have also added the numerical solution of Thoroddsen's equation (5.7) for comparison. We can see, that (5.7) implies $r_c/r_0 \le 0.8$. However the results are in quite good correspondence.

r_0, μm	Temperature T, °C	t_c ($r_c \simeq r_0$), μs
2.5	1538	0.5
4.435	1538	0.8
4.435	2500	0.35
10	1538	1.9

Table 5.3 – Coalescence time of equal liquid drops.

---

[1] The data are provided by Dr. P. Clausen.

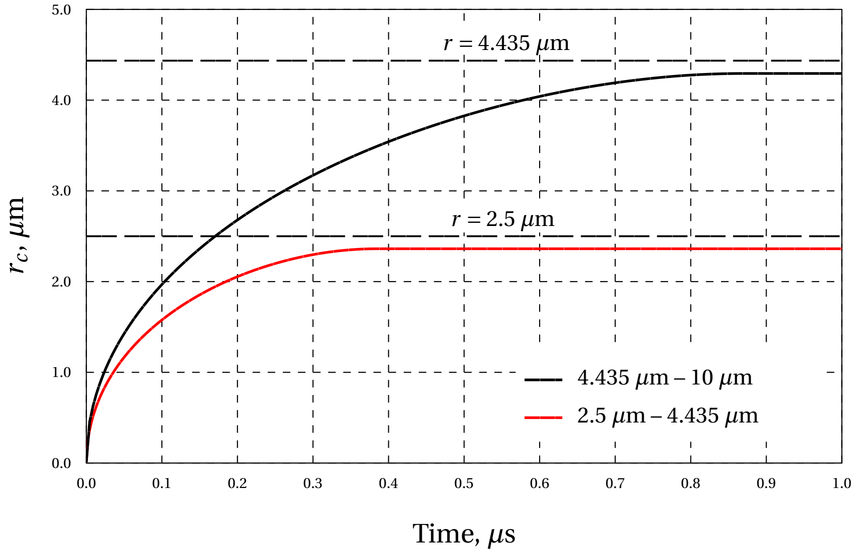

Figure 5.5 – Contact spot radius evolution between two liquid drops of different radii: (i) $r_1 = 2.5$ μm, $r_2 = 4.435$ μm; (ii) $r_1 = 4.435$ μm, $r_2 = 10$ μm (eq. (5.11)).

As we have already observed in Chapter 4, analysing a grain with radius $r_0 = 4.435$ μm is not enough to get a comprehensive overview of the used 18Ni(300) Maraging Steel powder shown in Fig. 3.1. We also have to consider the case of different grains, corresponding, for instance, to extreme radii 2.5 μm and 10 μm. In Fig. 5.4 we present the coalescence results for such grains as they are obtained from LFEM (solid lines) and eqs. (5.7) – (5.10) (dashed lines). It can be seen that for two equal liquid maraging steel drops of radii $2-10$ μm with an initial point contact between them, the time t_c, when $r_c \simeq r_0$, is in the range between 0.5 and 2 μs. For grain radii < 5 μm the two hypotheses (5.7) and (5.9) give quite similar results for the chosen parameters and $r_c/r_0 \leq 0.8$. The values of t_c for drops at melting temperature T_f can be estimated from Figs. 5.3 – 5.4. The results are presented in Tab. 5.3.

For typical 18Ni(300) Maraging Steel powder grains ($r_0 = 4.435$ μm) t_c does not exceed 1 μs. According to the results of Chapter 4, this time is much shorter than the time of complete melting for a particle of radius r_0 irradiated by a laser with a power $100-300$ W ($3-5$ μs).

Remark 5.2. *Since the surface tension γ and the dynamic viscosity μ are strongly dependent on temperature (see (5.1) and (5.3)), the contact spot evolution might also be affected. We can compare the values t_c for the minimum and maximum temperatures from the range $1538°C < T < 2500°C$. The case of equal grains of radii $r_0 = 4.435$ μm has been analysed for a temperature close to vaporization point T_v. The results can also be found in Tab. 5.3. According to Shikhmurzaev theory (5.9), the increase of temperature provokes the increase of the drops coalescence speed.*

r_1, μm	r_2, μm	Temperature T, °C	t_c ($r_c \simeq \min(r_1, r_2)$), μs
2.5	4.435	1538	~ 0.4
4.435	10	1538	~ 0.9

Table 5.4 – Coalescence time of liquid drops with different radii.

The Thoroddsen's equation (5.7) generalizes to the case, when the coalescence takes place between two drops of different radii r_1 and r_2:

$$\begin{aligned} \frac{\mathrm{d}r_c}{\mathrm{d}t} &= K_2\sqrt{\frac{\gamma}{\rho_l}\left(\frac{1}{\varsigma(t)} - \frac{1}{r_c(t)}\right)}, \\ \varsigma(t) &= r_1 + r_2 - \sqrt{r_1^2 - r_c^2(t)} - \sqrt{r_2^2 - r_c^2(t)}. \end{aligned} \tag{5.11}$$

Fig. 5.5 represents the evolution of the contact spot radius between two drops in two different cases $r_1 = 2.5$ μm, $r_2 = 4.435$ μm and $r_1 = 4.435$ μm, $r_2 = 10$ μm. When the grains have different radii, we define t_c as the time when $r_c \simeq \min(r_1, r_2)$. The values of t_c, measured on Fig. 5.5, are listed in Tab. 5.4.

From Figs. 5.4 – 5.5 we conclude that for the chosen radii of liquid drops, the coalescence time does not exceed 2 μs. For a typical 18Ni(300) Maraging Steel powder grain (4.435 μm) this time is even less than 1 μs, which is small compare to the corresponding melting time under a laser (3 – 5 μs, see Chapter 4).

5.3 Conclusions

In this Chapter we discussed the liquid-gas surface tension and the dynamic viscosity of liquid 18Ni(300) Maraging Steel. We have shown that an increase of temperature provokes a decrease of these parameters. However, the surface tension decreases slightly, while the reduction of the dynamic viscosity is significant. Capillary parameters of the material are summarized in Tab. 5.1.

We proposed a model for the initial stage of powder grains sintering. It considers the coalescence of liquid drops. The model describes the time evolution of the contact between two liquid drops using different 'square-root laws' $r_c \sim t^{1/2}$. The difficulty is that these laws involve empirical parameters. They have to be chosen according to the properties of the material and the geometry of the powder bed. We computed these parameters for liquid 18Ni(300) Maraging Steel by means of the Lagrangian finite element method.

The coalescence model has been used to show, that for 18Ni(300) Maraging Steel powder the time to reach merging between two molten particles does not exceed 1 μs. This time is relatively small compared to the typical time of complete melting of a powder grain ($3-5$ μs, see Chapter 4).

We have also shown, that, due to the decrease of the surface tension and the dynamic viscosity, the temperature increase can even accelerate the process of drops coalescence. Surface tension and dynamic viscosity do not intervene the coalescence process independently. It depends certainly only on the ratio γ/μ, which has the dimension of speed.

6 Numerical Modelling of SLS/SLM

A finite element simulation software has been developed at LGPP for the modelling of SLS/SLM processes [38]. This software, in contrast to commercial simulation tools, is built specially for Selective Laser Sintering and Melting.

In this Chapter, we discuss a numerical model used for the simulation of SLS/SLM. The model is based on the homogeneous medium hypothesis. We describe its main assumptions and advantages. In particular, we propose the use of two grids. One very fine mesh to achieve an accurate description of the geometry of the part under construction and one relatively coarse – to follow the temperature evolution with as few algorithmic complexity as possible. However local refinement will be needed to be sensitive, at the scale of the powder bed, to the fine features of the laser beam.

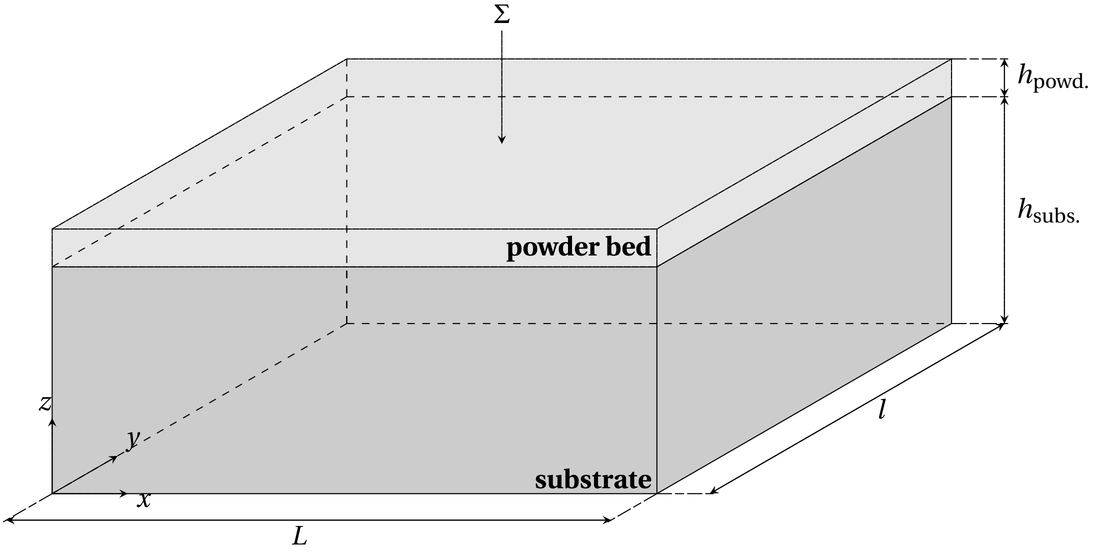

Figure 6.1 – Typical domain Ω: powder bed (with top surface Σ) on a substrate.

6.1 Numerical model description

The simulation software works in the framework of the *homogeneous medium hypothesis*. A powder bed is considered as an homogeneous medium. Material properties of this medium are characterized by averaged (so-called effective) parameters: absorptivity, thermal conductivity, etc. The parameters are averaged over a homogenization volume. For powders the dimensions of the homogenization volume should be several times larger than the characteristic size of the material, i.e. the size of a powder grain d_0.

In the framework of the model, heat transfer in a parallelepipedon Ω representing the powder bed and its immediate surrounding (like the substrate, see Fig. 6.1) is described by the evolution of two fields: the enthalpy per unit mass u and the temperature T.

6.1.1 Enthalpy and temperature evolution

The evolution of the first unknown, the enthalpy per unit mass u, follows the heat diffusion equation, completed by boundary and initial conditions [38]:

$$\begin{aligned}
&\rho\frac{\partial u}{\partial t} - \operatorname{div}(k\nabla T) = F, \text{ in } \Omega,\\
&-k\frac{\partial T}{\partial n} = \kappa(T - T_0) + f, \text{ on } \partial\Omega,\\
&u = u_0, \text{ in } \Omega, \text{ for } t = 0.
\end{aligned} \tag{6.1}$$

In equations (6.1) k denotes the effective thermal conductivity of the medium, ρ is its density, κ is the thermal exchange coefficient between the domain Ω and the environment of temperature T_0, F is a (given) volumic heat source, f is a (given) boundary heat source. The outwards normal derivative of the temperature on the surface $\partial\Omega$ is defined by $\frac{\partial T}{\partial n}$.

In SLS/SLM, the heat source is volumic, meaning that f is in principle zero. In some cases, the heat source will have to be approached by a surface source for numerical reason: $F = 0$ and $f \neq 0$ on the top surface Σ: $z = h_{\text{subs.}} + h_{\text{powd.}}$ (see Fig. 6.1).

It has also to be pointed that the thermal exchange coefficient κ is not well known except on the top surface Σ (see Chapter 8). The uncertainty on κ is however not an issue. The lateral surfaces and the bottom surface $z = 0$ (see Fig. 6.1) are (thermally) far away from the laser activities and the solution will be indifferent to the boundary conditions imposed there.

The equation, which connects the second unknown, the temperature T, with the enthalpy per unit mass u, is an algebraic relation [38]:

$$T = \beta(u), \text{ in } \Omega. \tag{6.2}$$

The function β, used in (6.2), is a non-decreasing function. Out of phase transitions, it can be directly connected to the heat capacity of the material C_p, by the formal relationship:

$$\frac{\mathrm{d}\beta}{\mathrm{d}u} = \frac{1}{C_p}, \quad \text{for } C_p = \text{const.} \tag{6.3}$$

The function β also allows to take the energy, consumed or released during phase transformations of the material, into account.

6.1.2 Sintering potential and effective properties

For a precise description of SLS/SLM process a third field is introduced. This field is called *sintering potential* Φ and contains the information about the state of the material during SLS/SLM [38, 81]. Its value is 0 in loose powder and the value 1 corresponds to fully dense bulk material.

The effective thermal conductivity k in (6.1) depends on sintering potential: $k = k(\Phi)$. During SLS/SLM the effective thermal conductivity of a medium evolves from the value k_p of a loose powder to the value k_s corresponding to a bulk material (see § 3.3.3 of Chapter 3) and can be connected to the sintering potential Φ by interpolating between k_p and k_s:

$$k(\Phi) = (1 - \Phi)k_p + \Phi k_s. \tag{6.4}$$

In this work we actually consider equation (6.4) as the definition for the sintering potential Φ. It respects the condition $\Phi = 0$ for loose powder and $\Phi = 1$ for bulk material. The sintering potential might also be used to evaluate another effective property of the powder bed: its absorptivity (see Chapter 3). The absorptivity α decreases from the high value α_p in powder to the low one α_l for liquid materials (see § 3.3.1 of Chapter 3). In the example of 18Ni(300) Maraging Steel we can see that even the absorptivity of the solid material α_s also often differs from the absorptivity of its liquid state α_l (see Tab. 3.6).

In the framework of our numerical model, we deduce α from the value of the sintering potential by means of an interpolation rule similar to (6.4). However, due to phase transition, the dependence of α on the local value of temperature can not be neglected

$$\alpha(\Phi, T) = (1-\Phi)\alpha_p + \Phi\alpha_{\text{bulk}}(T) \tag{6.5}$$

with

$$\alpha_{\text{bulk}}(T) = \begin{cases} \alpha_s, & \text{if } T < T_f, \\ \alpha_l, & \text{if } T \geq T_f. \end{cases} \tag{6.6}$$

If the interpolation rule (6.4) for the thermal conductivity is considered as exact and serves as a definition for the sintering potential Φ, consider that eq. (6.5) is only an assumption.

6.1.3 Sintering potential evolution

In fact, the sintering potential relates to the connections between particles of a sintered powder. It evolves in time according to an ordinary differential equation with initial data which can be written as [75]:

$$\begin{aligned} &\frac{\partial \Phi}{\partial t} = \zeta(1-\Phi), \ \text{in } \Omega, \\ &\Phi = 0, \ \text{in } \Omega, \text{for } t = 0. \end{aligned} \tag{6.7}$$

where the parameter ζ, called sintering rate, is the inverse of the characteristic sintering time τ_{sint} of the material.

We have developed the phenomenological law, which allows to compute the sintering rate ζ at any point $\mathbf{x}$ of the powder bed at any moment of time t. According to a microscopic model for the liquid flow dynamics between neighbouring powder particles, we assume:

$$\zeta(\mathbf{x}, t) = \begin{cases} 1/\tau_{\text{sint}}, \ \text{if } \frac{3}{4\pi\delta_0^3}\int_{B(\mathbf{x},\delta_0)} T(\mathbf{y}, t)\mathrm{d}^3\mathbf{y} \geq T_t \\ 0, \ \text{otherwise} \end{cases} \tag{6.8}$$

where $B(\mathbf{x}, \delta_0)$ denotes the sphere of radius δ_0 centered at the point $\mathbf{x}$. The three parameters: sintering time τ_{sint}, radius δ_0 and threshold temperature T_t, involved in the law (6.8), are connected to the properties of powder and molten material and to the operating parameters.

In particular, the parameter δ_0 is related to the geometrical powder properties (packing, grain size distribution). In the model, we will often assume it to be equal to the size of a typical powder grain d_0.

On the other hand, the default value for the sintering threshold T_t is the material melting point T_f [38]. However, in general, it also depends on the material properties and operating parameters. The estimation of the sintering threshold temperature in SLS/SLM simulation will be discussed in Chapter 7.

Finally, when processing of metallic powders with typical particle sizes less than 10 μm and with high laser powers (see § 2.1.3 of Chapter 2), the characteristic sintering time τ_{sint} turns out to be very small compare to the laser irradiation time (see Chapters 4 and 5), and the evolution equations (6.7)-(6.8) for Φ might be replaced by the limit case when $\tau_{\text{sint}} \to 0$. This limit case means that we can **neglect the partial sintering stage** and that the sintering potential goes to 1 as soon as the average temperature in the ball of radius δ_0 has reached the threshold T_t:

$$\Phi(\mathbf{x}, t) = \begin{cases} 0, \text{ if } \frac{3}{4\pi\delta_0^3} \int_{B(\mathbf{x},\delta_0)} T(\mathbf{y}, s) \mathrm{d}^3\mathbf{y} < T_t, \ \forall\, s < t, \\ 1, \text{ otherwise.} \end{cases} \tag{6.9}$$

6.2 Numerical method

The numerical approach, described by equations (6.1) – (6.9), not only helps to model SLS/SLM processes with good precision but also allows to estimate the accuracy of a final sintered part. In this Section we will describe the numerical method, used for its realisation.

6.2.1 Time discretization

A simulation time step τ is chosen for time discretization. It should be sensitive to the evolution of time- and temperature-dependent material and process parameters. In the case of melting of a powder with a continuous laser, the scales of this evolution are the time to melting for the powder surface and the characteristic sintering time τ_{sint}.

We assume τ_{sint} to be negligibly small (see § 6.1.3 for the details). For fine powders, like 18Ni(300) Maraging Steel (see Chapter 3), and laser powers between 100 W and 300 W the time to surface melting is less than 5 μs (see Chapter 8). Therefore, for the simulation of SLS/SLM under these process conditions, we propose:

$$\tau = 1 - 5\ \mu\text{s}. \tag{6.10}$$

The time step being chosen, we are looking for a series of profiles $u^n : \Omega \to \mathbb{R}$, $T^n : \Omega \to \mathbb{R}$ and $\Phi^n : \Omega \to \mathbb{R}$ approaching the real enthalpy per unit mass, temperature and sintering potential profiles, respectively, at discrete times $t_n = n\tau$, $n = 0, 1, 2 \ldots$.

The initial conditions in (6.1) and (6.7) and the algebraic relation (6.2) gives the profiles for $t_0 = 0$:

$$u^0 = u_0, \quad T^0 = \beta(u_0) \text{ and } \Phi^0 = 0. \tag{6.11}$$

The idea is then to deduce recursively $\{u^{n+1}, T^{n+1}, \Phi^{n+1}\}$ from $\{u^n, T^n, \Phi^n\}$, $n = 0, 1, 2, \ldots$. Implicit connections between $\{u^{n+1}, T^{n+1}, \Phi^{n+1}\}$ and $\{u^n, T^n, \Phi^{n+1}\}$ (like backward Euler scheme) are favorable. They do not impose strict restriction on the time step τ to be used. These restrictions, known as stability conditions [82], depend on spatial discretization and increase considerably the algorithmic complexity of the numerical method.

The simple profile to deal with is the sintering potential. Applied to (6.7) the backward Euler scheme gives

$$\Phi^{n+1} = \frac{\Phi^n + \tau\zeta^{n+1}}{1 + \tau\zeta^{n+1}} \tag{6.12}$$

with ζ^{n+1} - the profile of the sintering rate ζ at time t_{n+1} (see (6.8)).

The situation is unfortunately more complicated for the enthalpy and the temperature. Due to the non-linearity in the enthalpy-to-temperature function β (6.2), standard implicit scheme lead to non-linear equations to be solved at each time step and are therefore not appropriate. The so-called Nochetto-Verdi (NV) scheme [83] combines the advantages of stability and computing simplicity with only **one linear** equation to be solved at each time step. This is the reason why our numerical scheme is based on this technique [38].

The NV scheme works in two steps. At first, it updates the temperature profile by solving a Laplace problem for T^{n+1} which involves the enthalpy profile u^n only. This problem comes from (6.13) and reads:

$$\begin{aligned} &\rho T^{n+1} - \omega_{\mathrm{NV}}\tau \operatorname{div}(k\nabla T^{n+1}) = \rho\beta(u^n) + \omega_{\mathrm{NV}}\tau F^{n+1}, \text{ in } \Omega, \\ &-k\frac{\partial T^{n+1}}{\partial n} = \kappa(T - T_0) + f^{n+1}, \text{ on } \partial\Omega, \end{aligned} \tag{6.13}$$

with $F^{n+1}, f^{n+1} : \Omega \to \mathbb{R}$ - the profiles of the sources F and f at time t_{n+1} and ω_{NV} a relaxation parameter. Stability is ensured [83] if ω_{NV} is chosen bigger than the derivative of the function β (see eq. (6.3)):

$$\omega_{\mathrm{NV}} \geq \max \frac{\mathrm{d}\beta}{\mathrm{d}u} = \frac{1}{\min C_p}. \tag{6.14}$$

The next step is to recover u^{n+1} from u^n and from the temperature profile T^{n+1} computed in the first step. The equation we used is based on (6.2) and reads:

$$u^{n+1} = u^n + \frac{T^{n+1} - \beta(u^n)}{\omega_{\mathrm{NV}}}, \text{ in } \Omega. \tag{6.15}$$

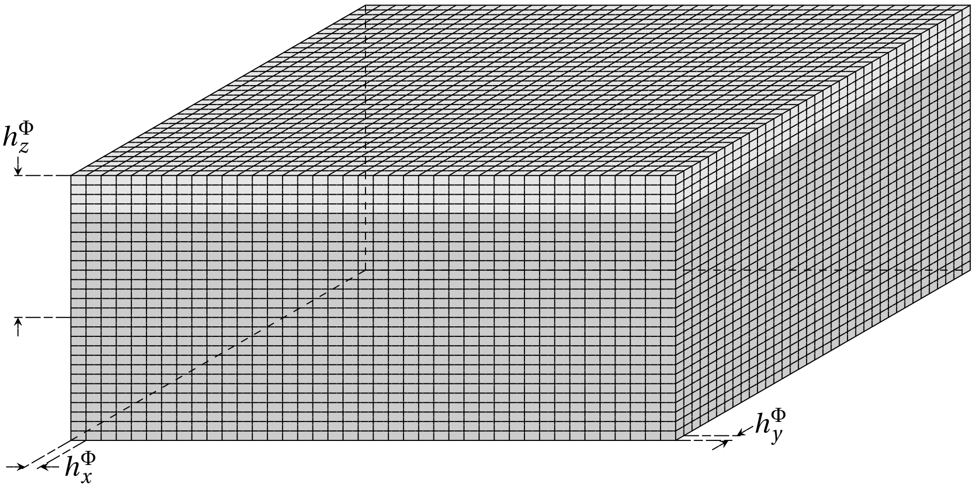

Figure 6.2 – Illustration of the net of parallelepipedic cells for the space discretization of the sintering potential Φ.

The NV scheme however suffers form a serious drawback. The temperature profiles T^n (called Nochetto-Verdi temperature profiles) show only weak convergence to the real temperature profiles. Fortunately, the convergence property of the enthalpy u^n is much better. For a reliable approximation of the temperature profile at time t_n it is therefore recommended to go back to equation (6.2) and to use

$$\vartheta^n = \beta(u^n) \tag{6.16}$$

instead of T^n.

6.2.2 Space discretization

A finite element method (FEM) is used to discretize the sintering potential, the enthalpy and the temperature profiles.

The case of the sintering potential is again the simplest. Since equation (6.12) does not involve any spatial derivation, it is possible to define the finite element approximation Φ_h^n of the sintering potential profile Φ^n as a piecewise constant function over a mesh of the domain Ω. The mesh we propose for Φ is illustrated on Fig. 6.2 and consists of (possibly non homogeneous) parallelepipedic cells.

The shape of the fabricated part is strongly connected to the sintering potential. Going back to the definition of Φ (6.4), we can identify the fabricated part with the subdomain of Ω in which $\Phi \simeq 1$. The mesh size h_x^Φ, h_y^Φ and h_z^Φ used to construct the discretization grid for Φ (Fig. 6.2) turn out to be directly connected to the geometrical resolution of our numerical model. To obtain predictions useful for general applications in mechanics, an accuracy of at least one hundredth of a mm is required meaning that

$$h_x^\Phi = h_y^\Phi = h_z^\Phi \simeq 10\,\mu\text{m}. \tag{6.17}$$

A consequence of this condition is the large number n_Φ of degrees of freedom which are needed for Φ at the scale of the domain Ω (some cm in the three directions). However, since the sintering potential can be updated in each FEM cell separately (eq. (6.12)), the algorithmic complexity only grows linearly with the number n_Φ. A very fine grid (up to 10^9 cells) for Φ is therefore possible with a limited impact on the method efficiency.

The situation is completely different for the discretization of the enthalpy and temperature profiles. Because of the Laplace problem (6.13), we have to limit ourselves to a few hundred thousand degrees of freedom to represent u_h^n or T_h^n if we want to maintain the algorithmic complexity in an acceptable range. The finite element mesh to be used for u_h^n or T_h^n has to be much coarser than the net (see Fig. 6.2) for Φ_h^n.

To satisfy this condition and to be still sensitive enough to the fine details of the laser beam shape (the typical beam radius are of some tens of μm), we propose a non-conformal mesh evolving in time (Fig. 6.3). It is composed of a refined part following the laser completed by a coarse part discretizing the entire domain Ω. The elements in the coarse mesh are tetrahedra, the elements in the fine mesh are orthogonal prisms obtained by extruding the surface triangles (see Fig. 6.3) in the z direction.

The dimensions H_x^T, H_y^T of the elements in the coarse mesh in the plane (x, y) (Fig. 6.3) are mostly defined by the scanning strategy and by the laser beam radius ω. For focused laser beams with $\omega < 100$ μm we propose:

$$H_x^T = H_y^T \simeq \frac{\omega}{2}. \tag{6.18}$$

A stability condition is actually linking the choice (6.18) to the time step τ (6.10). It reads:

$$\tau \ll \frac{\max\{H_x^T, H_y^T\}}{v} \tag{6.19}$$

where v is the laser scanning speed. The idea of this condition is to prevent the laser from flying over many coarse cells during a single time step. For normal processing condition (see Tabs. 3.4 and 3.5), the stability condition (6.19) is easily fulfilled by the time step given in (6.10) and the mesh sizes (6.18).

The parallelepipedic grid for the sintering potential (Fig. 6.2) is finally adapted to the coarse mesh. We recommend to create it by dividing each coarse mesh intervals in 3 to 5 sub-intervals.

The size of the elements in the fine mesh is determined according to the heat source distribution. Usually the regions with high temperature gradients are localized in the proximity of the heat source. However, due to the significant difference between powder and bulk thermal conductivities, the fine mesh should cover not only the laser spot area, but also the region around it. We propose the following relation between the dimensions D of the fine mesh (Fig. 6.3) and laser spot radius ω:

$$\frac{D}{\omega} \simeq 10-20. \tag{6.20}$$

In the center of the fine mesh, where the laser is supposed to be located, we propose to select the area A of the triangular element on the surface (Fig. 6.3) in order to have a good description of the laser beam:

$$\frac{\pi\omega^2}{A} \simeq 20-30. \tag{6.21}$$

The size of the elements in the fine mesh can be increased from the center to the border. The idea is to smoothen the transition to the coarse mesh and to avoid too much hanging nodes [84]. A thumb rule is that the ratio between triangle areas in neighboring zones should not exceed 4.

In the z direction the discretization is made in a way that all the nodes are located on horizontal planes (called reticular planes) with altitudes (Fig. 6.1)

$$z_0 = 0 < z_1 < z_2 < z_3 \ldots < z_m = h_{\text{subs.}} + h_{\text{powd.}} \tag{6.22}$$

possibly spaced in a non-regular manner. To increase computation accuracy, the altitudes z_i are usually arranged in geometric progression. For the case of a thin powder layer on a massive substrate we recommend to increase the z-discretization near the upper surface where we have the laser activity. In this region, the fine mesh interval h_z should be adapted to the penetration depth (see § 3.3.1 of Chapter 3). We propose:

$$h_z \simeq \frac{\delta}{10}. \tag{6.23}$$

In the vicinity of the interface between powder and substrate (where we expect properties discontinuities), the mesh should also be refined in the $z-$direction. In order to prevent numerical instabilities, the lengths of the last interval in the powder layer and the first interval in the substrate should be of the same order. Except the upper elements, discretization of the substrate is less important than in the powder domain.

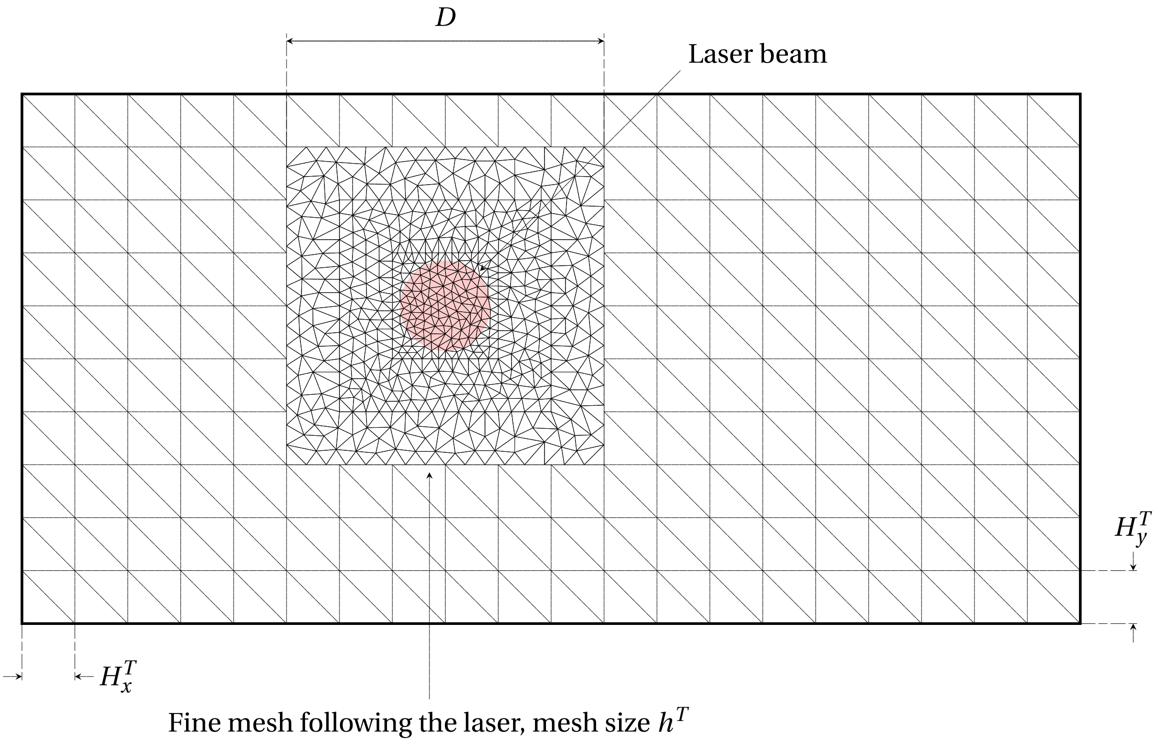

Figure 6.3 – Top view of the non conformal mesh for the temperature/enthalpy profiles.

In conformity with the NV scheme (6.13) the enthalpy profile u_h^n will be searched in the space of piecewise constant functions over the mesh. The degrees of freedom for the enthalpy are in the center of the elements. The temperature profile has to be more regular. We will look for it under the form of a continuous piecewise linear[1] function. The degrees of freedom for the temperature are located at the nodes of the mesh. As it is usual for non-conformal FEM, temperature discontinuities are tolerated across the border between the coarse and the fine meshes. The continuity is imposed afterwards by a penalty technique [84].

---

[1] In the fine mesh where prismatic elements with 6 nodes are used, the temperature will be piecewise linear but separately in the horizontal variables $\{x, y\}$ and in the vertical variable z to match the number of degrees of freedom.

7 Sintering Threshold in SLS/SLM

The powder sintering threshold is one of the key parameters, required for the estimation of the material state during the process (see Chapter 6). In particular, the knowledge of the sintering threshold allows to predict dimensions of the final part. Nowadays the most-used criterion of the sintering quality is based on the material melting temperature. However the discrepancies between theoretical and experimental results for actual process parameters (i.e. high laser powers and high scanning speeds, see § 2.1.3 of Chapter 2) point out that this criterion should be improved.

In this Chapter we propose and justify a new method for the estimation of the powder sintering threshold. This approach is based on the study of the melting of a single powder grain, which has been presented in Chapter 4.

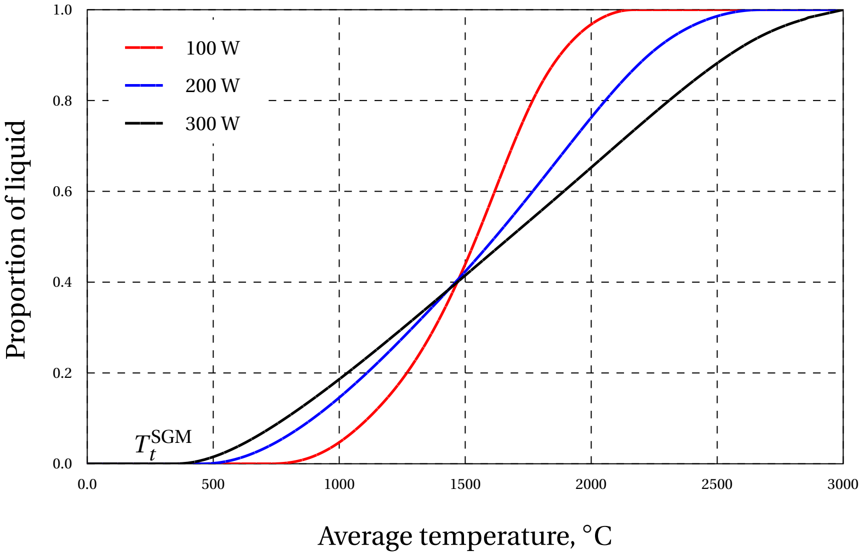

Figure 7.1 – Evolution of the molten material fraction and the average temperature of a 18Ni(300) Maraging Steel powder grain for different laser powers.

7.1 Evolution of the grain melting threshold

In Chapter 4 we studied the melting process of a separate 18Ni(300) Maraging Steel powder grain, irradiated by a plane wave (see Remark 7.1). The wave intensities corresponded to the intensities of the laser beam with the properties listed in Tab. 3.4. We have chosen a range of laser powers between 50 and 400 W, representative for actual industrial SLS/SLM process parameters.

Remark 7.1. *The values of the plane wave intensity I_0 are always calculated for a laser beam of radius $\omega = 40$ μm: $I_0 = P/\pi/\omega^2$ (see eq. (4.4) in Chapter 4). The laser wavelength is 1070 nm.*

Laser power P	Wave intensity I_0 (4.4)	T_t^{SGM}
50 W	9947 W/mm^2	1021 °C
100 W	19894 W/mm^2	710 °C
200 W	39789 W/mm^2	442 °C
300 W	59683 W/mm^2	309 °C
400 W	79577 W/mm^2	269 °C

Table 7.1 – Melting threshold T_t^{SGM} of a 18Ni(300) Maraging Steel powder grain, irradiated by a plane wave of intensity I_0, approaching the laser of power P.

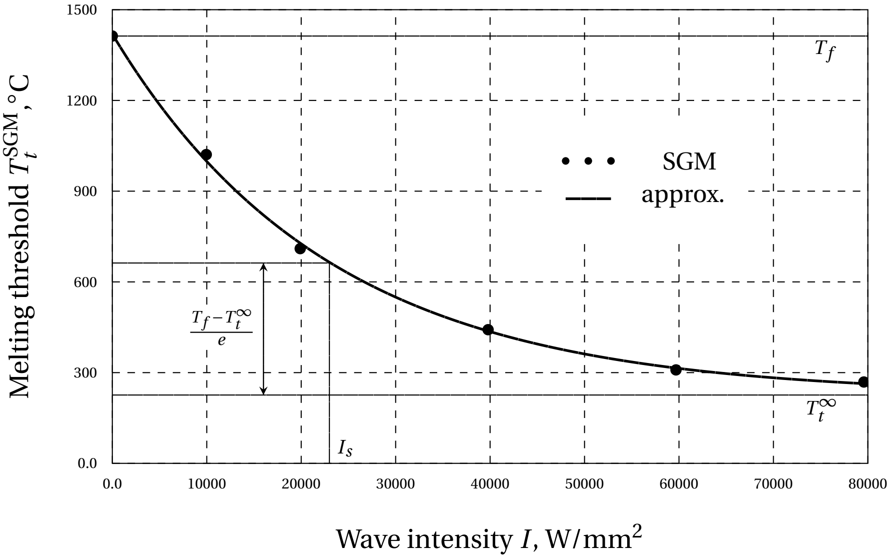

Figure 7.2 – The dependency of the grain melting threshold T_t^{SGM} on the wave intensity.

Under these conditions, we have shown that the melting of a single powder grain is not homogeneous over the grain volume (see Fig. 4.4). In order to connect the evolution of single grain properties to the modification of the parameters of the whole powder bed, we estimated the average temperature of a grain during its melting. Fig. 7.1 shows the relation between the molten material fraction and the average temperature in the particle. It proves that the melting of a separate powder particle starts when its average temperature is significantly less than the melting point of the material ($T_f = 1413$°C, see Tab. 3.2). We will denote this grain melting threshold as T_t^{SGM} ('threshold'). The values of T_t^{SGM} for different wave intensities are listed in Tab. 7.1. This information is also represented graphically in Fig. 7.2.

From this figure, it can be seen that the threshold temperature T_t^{SGM} decreases from the melting temperature T_f to an asymptotic value T_t^∞. We assume an exponential decay and we propose to fit the curve in Fig. 7.2 with the empirical formula

$$T_t^{\mathrm{SGM}}(I) = T_t^\infty + (T_f - T_t^\infty)e^{-I/I_s}, \tag{7.1}$$

where I_s denotes the wave intensity, for which $T_t^{\mathrm{SGM}} - T_t^\infty$ decreases by facor e times (Fig. 7.2). The fit parameters we get in this situation for a typical 18Ni(300) Maraging Steel powder grain (see Tab. 3.6) are:

$$\begin{aligned} I_s &\simeq 22984\,\mathrm{W/mm}^2, \\ T_t^\infty &\simeq 226°\mathrm{C}. \end{aligned} \tag{7.2}$$

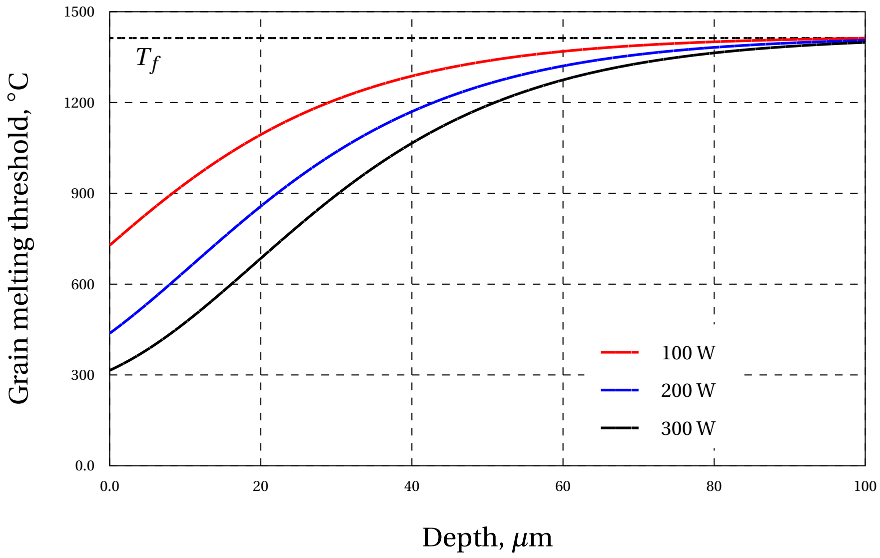

Figure 7.3 – The dependency of the melting threshold on the depth for wave intensities, approaching laser powers 100 W, 200 W, 300 W.

As we already discussed in § 3.3.1 of Chapter 3, the propagation in z-direction of a gaussian laser beam with properties listed in Tab. 3.4, in a powder can be described by a generalized Beer-Lambert law up to a depth not exceeding some millimeters:

$$I(x, y, z, t) \simeq I_l(x, y, t)e^{-z/\delta}. \tag{7.3}$$

In (7.3) $I_l(x, y, t)$ is the incident laser beam intensity at location (x, y) and time t on the surface of the material and δ is the optical penetration depth of the material.

Combining (7.1) and (7.3), we get a law expressing the threshold temperature as a function of the position in the powder bed:

$$T_t^{\mathrm{SGM}} = T_t^{\mathrm{SGM}}(x, y, z, t). \tag{7.4}$$

The dependency of the melting threshold in the depth for different laser powers is shown in Fig. 7.3. The penetration depth is 20 μm (see § 3.3.1 of Chapter 3).

From Fig. 7.3 we can see that, for the chosen wave intensities and powder properties, the melting threshold of a particle is significantly less than the melting point of the material T_f if the particle is located at a depth less than 100 μm from the surface of the powder layer. It can also be observed that the threshold temperature increases up to the melting point of the material T_f because, in the depth, the grains are heated more smoothly and homogeneously.

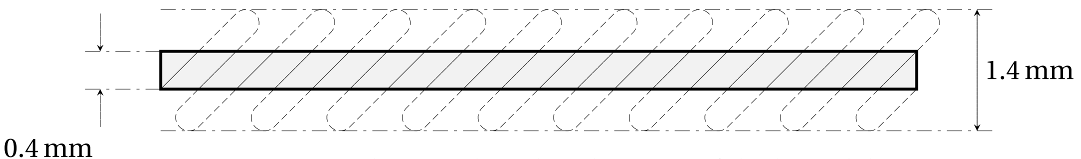

Figure 7.4 – Exact laser path and explanation of the laser delay.

We now propose to use the value T_t^{SGM} for the threshold T_t involved in the evolution equation for the sintering potential (6.7) – (6.8) or (6.9) in the limit case, when partial sintering can be neglected. Observe that all the discussions in the rest of this Chapter will be based on the limit case equation (6.9). The justification for that can be found in Chapters 4 and 5, where we have shown that, for 18Ni(300) Maraging Steel powder (Tab. 3.6) processed under standard SLS/SLM parameters (Tab. 3.4) the melting and interconnection time of particles is small compare to the laser irradiation time.

Our idea is now to propose an experimental validation of the empirical expression (7.4) for the sintering threshold. To do so, we will make use of this relation together with (7.1), (7.2) and (7.3) to simulate the SLM construction of a thin wall of 400 μm thickness out of 18Ni(300) Maraging Steel powder and with two different parameter sets. At the end, we will compare the numerical prediction of the interlayer connection quality to an EBSD analysis of the real parts and to equivalent simulation results obtained with the default choice $T_t = T_f$ for the sintering threshold.

7.2 Process parameters and material properties

The process conditions are listed in Tab. 7.2. We will denote the two sets of process parameters as ‘Set I’ and ‘Set II’. The scanning strategy, used in both cases, is presented in Fig. 7.4. The scanning starts with an angle of 30° from the border. When reaching the other border the laser follows a rounded path (see Fig. 7.4). During this time it is switched off. The time of the laser switch-off is 500 μs. The hatching distance of the strategy is 50 μm. The layer thickness is also 50 μm. The powder is deposited on the solid massive substrate, which is also made of 18Ni(300) Maraging Steel.

Properties of 18Ni(300) Maraging Steel powder and liquid materials are presented in Tab. 3.6. As we have already discussed in Chapter 6 (see eqs. (6.6) and (6.4)), we include into the simulation the evolution of the absorptivity (from 0.8 to 0.2) and the effective thermal conductivity (from 0.1 W/m/°C to 26 W/m/°C) of the material due to its phase change (see Chapter 8 for more information about influence of these phenomena on the process).

Parameter	Set I	Set II
Laser wavelength	1070 nm	1070 nm
Laser power P	200 W	330 W
Laser beam radius ω	40 μm	40 μm
Laser beam profile	TEM$_{00}$	TEM$_{00}$
Scanning speed v	1.4 m/s	3.4 m/s
Hatching distance h_h	50 μm	50 μm
Scanning angle	30°	30°
Powder layer thickness h_l	50 μm	50 μm
Laser switch-off time	500 μs	500 μs

Table 7.2 – Sets of process parameters.

We also take the latent heat of fusion and the latent heat of vaporization of the material into account (see § 3.2 of Chapter 3). The laser beam penetration depth is 20 μm (see § 3.3.1 of Chapter 3).

The chosen substrate thickness is 250 μm, which is several times bigger, than the powder layer (50 μm, see Tab. 7.2). The properties of the substrate correspond to the bulk 18Ni(300) Maraging Steel (Tab. 3.6).

7.3 Simulation results

A single layer scanning has been modelled. The quality of the final part depends on the attachment of the molten powder layer to the substrate or to the previous molten layer. In order to estimate it, we compute the time spent by the material at a temperature higher than the local melting threshold.

Fig. 7.5 represents the time spent above the local threshold as a function of the depth z, for coordinates x and y corresponding to the middle of the scanning strategy. For comparison the two parameters sets are analysed for the two different choices of the sintering threshold: $T_t = T_t^{\mathrm{SGM}}$ (see (7.1), (7.2) and (7.3)) and $T_t = T_f$.

Remark 7.2. *The oscillations, seen on the graphs, are caused by the domain discretization. They can be diminished by choosing of a finer mesh (see § 6.2.2 of Chapter 6 for the details). However it will increase the simulation time and require high computer powers.*

As it can be seen from Fig. 7.5, the default choice $T_t = T_f$ for the sintering threshold leads to the conclusion that there is no attachment between the sintered region and the substrate for the two sets of parameters (Fig. 7.5, dashed lines), which does not correspond to the experimental results.

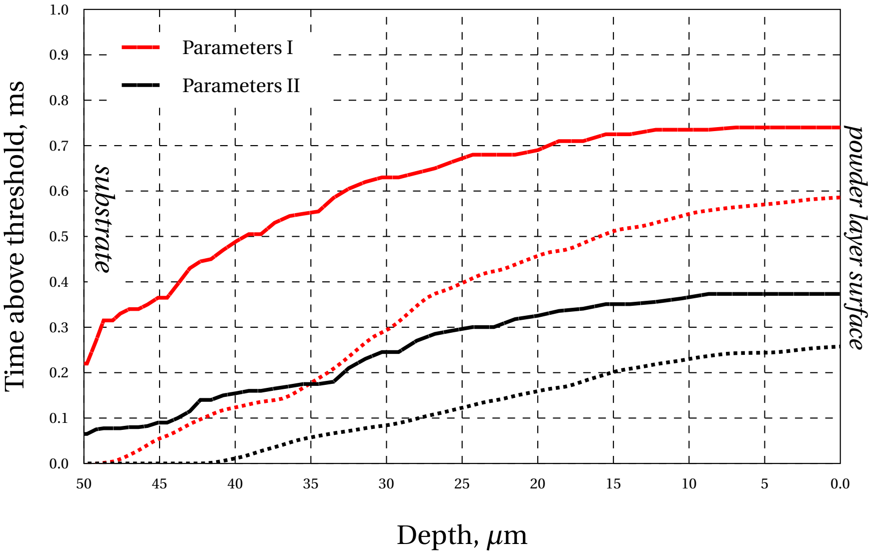

Figure 7.5 – Time above the sintering threshold when $T_t = T_t^{\text{SGM}}$ (solid lines) and when $T_t = T_f$ (dashed lines) for Sets I and II (Tab. 7.2).

The time, spent by the material at a temperature above the sintering threshold, gives also an indication about the quality of the final part. Fig. 7.5 shows, that the temperature near the substrate stays above the threshold for a longer time (about 200 μs), when the parameters of Set I are used. The conclusion is that the parameters of Set I are favorable to a better interlayer attachment of the part and they should be preferred to the parameters of Set II.

The simulation results are in agreement with the study of the real sintered parts. Fig. 7.6 shows the results of the EBSD (electron backscattered diffraction) analysis made on the polished sections of the sintered parts in z-direction[1].

The analysis represents the microstructure of the samples. It was made to see how the grains have grown between different layers. Each color corresponds to a different crystallographic orientation. The black regions are the regions which have not been indexed. That is caused by the distortion of martensite crystals which do not always diffract the electrons clearly.

In Fig. 7.6, it can be seen that the grains of the sample ‘Set I’ are bigger than the grains in sample ‘Set II’. Moreover they are elongated in the direction of the construction. This experimental observation confirms the prediction deduced from the simulation results presented in Fig. 7.5 on the quality of the interlayer attachment.

---

[1] The data are provided by Dr. J.Jhabvala.

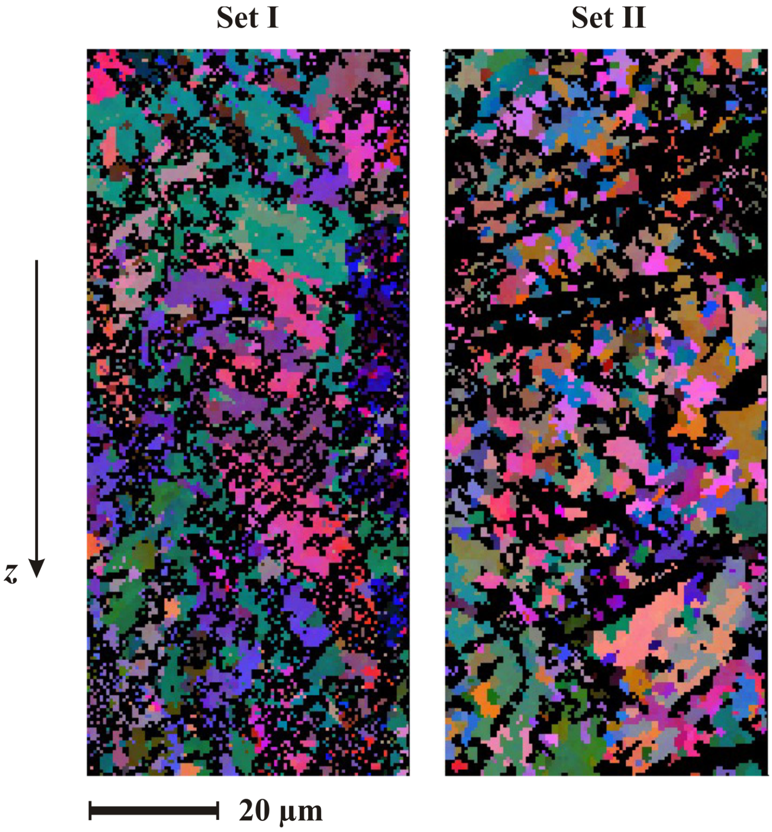

Figure 7.6 – EBSD analysis of the results for sets I and II (Tab. 7.2). Provided by Dr. J.Jhabvala.

7.4 Conclusions

In this Chapter we discussed the questions related to the numerical estimation of the material state during SLS/SLM. We have proposed a theory based on the results of the Single Grain Model (Chapter 4), telling that the melting threshold of a grain in a scanned powder bed depends on the local value of the incoming radiation intensity.

We justified this model by experimental validations. They are based on the comparison between the observations by SEM/EBSD and the numerical predictions of the dimension and of the interlayer connection in produced SLM samples.

The approach is not universal for all powders types and process parameters. Actually it requires a preliminary analysis of the melting mechanisms of a single powder particle. However in this Chapter we introduce an empirical formula (eqs. (7.1) – (7.2)) to estimate the sintering threshold for 50 μm layer of the 18Ni(300) Maraging Steel powder (or other steel powders with similar properties), sintered by a focused laser beam (Tab. 7.2) in the range of powers between 50 and 400 W and scanning speeds 1 – 3 m/s.

8 Mechanisms Affecting the Efficiency of SLS/SLM Process

Additive processes have now reached a point where they are considered as possible alternatives to traditional manufacturing technologies. At this moment their effectiveness becomes crucial. That is why process efficiency is one of the key characteristics for SLS/SLM.

Application of high laser powers (up to 1 kW) can improve the process efficiency. However significant energy losses and fast heat evacuation from the surface of the material during SLS/SLM could reduce the benefit that the increase of the laser power should have on the speed of the process. It could also cause premature wear of the technical equipment mounted in immediate proximity of the powder surface: for example, back reflection of the laser irradiation can damage lenses, scanning head, etc.

In this Chapter we discuss phenomena, which can be caused by the evolution of material properties during SLS/SLM. We also study different mechanisms of energy losses and their influence on the process efficiency.

P/v W/(m/s)	Simulation $\alpha_p = 0.8$ $k_p = 0.1$ W/m/°C	Simulation $\alpha = 0.8 - 0.2$ $k = 0.1 - 26$ W/m/°C	Rosenthal (powder) $\alpha_p = 0.8$ $k_p = 0.1$ W/m/°C	Rosenthal (liq. mat.) $\alpha_l = 0.2$ $k_l = 26$ W/m/°C
100/1	12700 °C	2862 °C	253895 °C	3556 °C
100/2	2862 °C	2290 °C	179559 °C	2662 °C
100/3	2862 °C	1930 °C	146617 °C	2209 °C
200/1	34200 °C	2862 °C	507790 °C	7112 °C
200/2	13200 °C	2862 °C	359118 °C	5324 °C
200/3	6250 °C	2862 °C	293234 °C	4418 °C
300/1	55900 °C	3460 °C	761685 °C	10668 °C
300/2	24200 °C	2862 °C	538677 °C	7986 °C
300/3	13700 °C	2862 °C	439851 °C	6627 °C

Table 8.1 – Influence of the thermal conductivity and absorptivity evolution on the maximum temperature reached under the laser: simulation vs. Rosenthal solution (8.4).

8.1 Thermal conductivity and absorptivity evolution in SLS/SLM

In Chapter 3 we came to the conclusion that properties of a metallic powder can change significantly during SLS/SLM. We have shown that in the case of 18Ni(300) Maraging Steel powder, its absoprtivity evolves from quite a high value for the loose powder (0.7 – 0.8) to the low one of the liquid metal (0.1 – 0.3). In the case of high laser powers it can cause significant laser energy losses during sintering process and can even damage the equipment.

In Chapter 3 we also discussed that in the case of laser treatment of a bulk material the evolution of its thermal conductivity may be not significant, while in the case of metallic powders it cannot be neglected. The difference between the thermal conductivities of 18Ni(300) Maraging Steel powder and bulk material is more than 200 times: 0.1 W/m/°C and 26 W/m/°C for powder and solid, respectively (see Tab. 3.6). We see that a metallic powder can act as an insulator during the process. However its melting can provoke fast evacuation of laser heat from the surface in depth of the material.

8.1.1 Simulation: constant material properties

To prove the existence of material powder absorptivity and thermal conductivity evolution during SLS/SLM process, we will estimate numerically the maximum temperature reached on the surface of a thick powder bed during laser scanning. Calculations are made in the framework of the homogeneous medium hypothesis (see Chapter 6), in assumption that melting does not influence the powder bed properties.

For the simulation we use the parameters corresponding to 18Ni(300) Maraging Steel powder (Tab. 3.6). Thermal conductivity and absorptivity of the material stay constant: $\alpha_p = 0.8$, $k_p = 0.1$ W/m/°C. Latent heat of fusion L_f and latent heat of vaporization L_v are taken into account (see § 3.2 of Chapter 3). Powder bed thickness is 250 μm, scanning strategy is a line. As far as we deal with a powder, the laser is considered as a volumic heat source (the optical penetration depth of powder is 20 μm, see Chapter 3). Laser beam radius is 40 μm, the profile is top-hat.

Maximum temperature values reached on the surface of the powder bed during laser scanning for the selected process parameters (see Tab. 3.5) are presented in the second column of Tab. 8.1.

It is experimentally known that for the used process and material parameters the vaporization point of a material is almost never reached ($T_v = 2862$ °C, see Chapter 3). However the temperature values, calculated in assumption of non-evolving material properties, significantly exceed it.

Therefore during SLS/SLM, heat evacuation from the surface into the depth of a powder bed due to a material thermal conductivity increase necessarily takes place. At the same time a drastic decrease of the surface absorptivity of the material under the laser due to its melting has also to be considered.

8.1.2 Rosenthal solution

We can estimate temperature under the laser by means of the Rosenthal solution of the heat transfer equation for a semi-infinite material with a moving non-point surface heat source.

Assume a point heat source of the power P, which moves with the scanning speed v along x-axis on the surface of a semi-infinite homogeneous material with the effective thermal conductivity k, the thermal diffusivity $\eta = k/\rho/C_p$ and the absorptivity α.

In that case, in a referential moving with the laser, the pseudo-stationary solution of the heat transfer equation is:

$$T(x,y,z) = \frac{P}{2k\pi}\frac{e^{-\frac{v(r+x)}{2\eta}}}{r}, \tag{8.1}$$

where $r = \sqrt{x^2+y^2+z^2}$.

For a non-point heat source with intensity distribution $Q(x,y)$, the expression of the temperature (8.1) generalizes as:

$$T_Q(x,y,z) = \frac{\alpha}{2k\pi}\int_{\mathbb{R}^2} Q(\xi,\zeta)\frac{e^{-\frac{v}{2\eta}\left(\sqrt{(x-\xi)^2+(y-\zeta)^2+z^2}+(x-\xi)\right)}}{\sqrt{(x-\xi)^2+(y-\zeta)^2+z^2}}\mathrm{d}\xi\mathrm{d}\zeta. \tag{8.2}$$

For a homogeneous cylindrical heat source of power P and radius ω (top-hat beam profile):

$$Q(\xi,\zeta)=\begin{cases}\dfrac{P}{\pi\omega^2}, & \xi^2+\zeta^2<\omega^2\\[2ex] 0, & \xi^2+\zeta^2\geq\omega^2,\end{cases} \tag{8.3}$$

(8.2) can be used to compute the value of the temperature under the laser:

$$T_Q(0,0,0)=\frac{P}{k\pi\omega}H\left(\frac{v\omega}{2\eta}\right). \tag{8.4}$$

The function H is an elliptic integral:

$$H(s)=\frac{1}{2\pi}\int_0^{2\pi}\frac{1-e^{-s(1-\cos\theta)}}{s(1-\cos\theta)}\mathrm{d}\theta. \tag{8.5}$$

For a gaussian heat source of power P and radius ω:

$$Q(\xi,\zeta)=\frac{P}{\pi\omega^2}e^{\frac{\xi^2+\zeta^2}{\omega^2}} \tag{8.6}$$

we get

$$T_Q(0,0,0)=\frac{P}{2k\sqrt{\pi}\omega}K\left(\frac{v\omega}{2\eta}\right), \tag{8.7}$$

where function K is:

$$K(s)=\frac{1}{2\pi}\int_0^{2\pi}e^{\frac{s^2}{4}(1-\cos\theta)^2}\left(1-\operatorname{erf}\left(\frac{s}{2}(1-\cos\theta)\right)\right)\mathrm{d}\theta. \tag{8.8}$$

Using equation (8.4) for the top-hat laser beam, we calculate the values of the maximum temperature, reached on the surface of the material under the laser, for 18Ni(300) Maraging Steel powder and liquid material (Tab. 3.6). Laser beam radius is 40 μm. The results are presented in two last columns of Tab. 8.1. We can observe that the Rosenthal solution (8.4) cannot be applied for the low-conductive materials (as powders) and high laser powers, as far as the results are far from reality.

For liquid metal, the temperature values, provided by (8.4), are significantly less, but still exceed the vaporization temperature of the material $T_v = 2862°\mathrm{C}$. It can be explained by the fact that the penetration of laser radiation into the material is not taken into account. It does not affect the results in the case of laser melting of bulk metals, but becomes crucial for powders (see § 3.3.1 of Chapter 3).

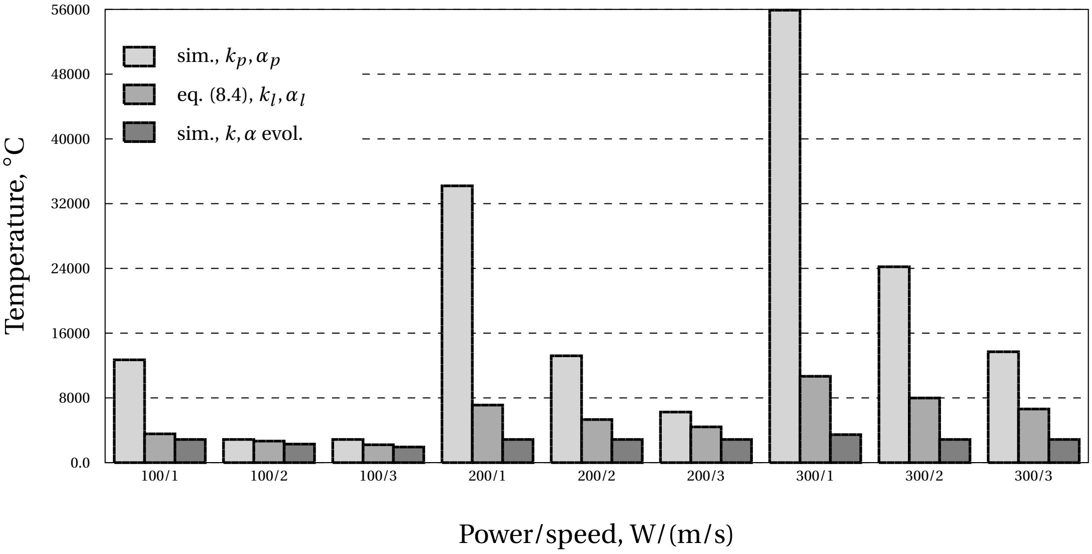

Figure 8.1 – Influence of the thermal conductivity and absorptivity evolution on the maximum temperature reached on the surface of the material during laser scanning (see Tab. 8.1).

8.1.3 Simulation: evolving material properties

When the melting temperature T_f is reached, molten material is produced and the rearrangement and interconnection of particles take place. Therefore, in the framework of the homogeneous medium hypothesis, the effective thermal conductivity of the medium evolves from a low value k_p, corresponding to loose powder, to a high value k_s for solid material (§ 3.3.3 of Chapter 3). The same mechanism explains the evolution of the surface absorptivity of a powder bed during laser melting. It decreases from a high powder absorptivity α_p to the low value α_l of a liquid material (§ 3.3.1 of Chapter 3)

The evolution laws of a material thermal conductivity and absorptivity are related to the melting dynamics of a powder bed and will be discussed in Chapters 4 and 5. In our numerical model, we neglect the stage of partially-sintered material, as it is explained in § 6.1.3 of Chapter 6. We assume that, when the temperature reaches the threshold value T_t equal to the melting temperature T_f in this case, the thermal conductivity and the absorptivity of the medium immediately evolve from k_p to k_s and from α_p to α_s, respectively (see Chapter 6).

We repeat the simulation, performed in § 8.1.1, but now we will include the evolution of the material properties. As far as we model the homogeneous medium with the effective properties of 18Ni(300) Maraging Steel powder (Tab. 3.6), we consider that its absorptivity decreases from 0.8 to 0.2, while the thermal conductivity increases from 0.1 to 26 W/m/°C, when the melting temperature $T_f = 1413°\text{C}$ is reached in conformity with the assumption that the partial sintering phase is negligible (see Chapter 6). Latent heat of fusion L_f and latent heat of vaporization L_v are also taken into account. Laser spot radius is 40 μm, beam profile is top-hat, optical penetration depth is 20 μm, scanning strategy is a line.

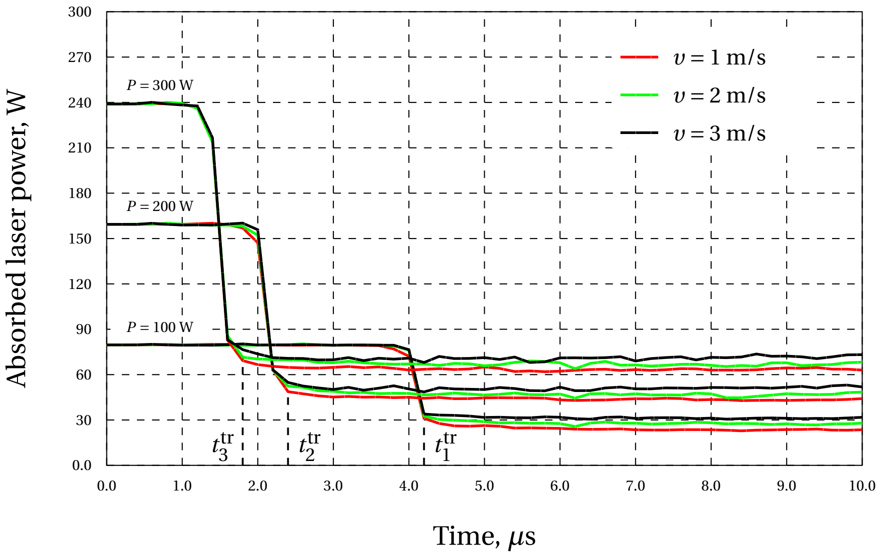

Figure 8.2 – Absorption of laser power in the beginning of the scanning for 18Ni(300) Maraging Steel powder.

Results of this simulation are presented in the third column of Tab. 8.1. The obtained values of the maximum temperature on the surface of the powder bed never exceed the vaporization point of the material $T_v = 2862°\text{C}$. It corresponds to experimental results for the selected process parameters. Thus, for a precise modelling of SLS/SLM of a metallic powder, it is necessary to take into account the evolution of its properties due to the phase change.

Fig. 8.1 visualizes the comparison between the data, obtained numerically, and the results, provided by Rosenthal solution (8.4) for the liquid material properties in § 8.1.2 (see Tab. 8.1).

We can see that only the simulation, which takes into account the evolution of material properties due to the phase change, gives reasonable results. However temperature values, calculated by means of Rosenthal solution (8.4) for the liquid metal properties, are not far from the numerical results. It allows to conclude that the evolution of the material properties due to the phase change is fast under considered process conditions (Tabs. 3.6 and 3.5).

8.1.4 Influence of absorptivity evolution on SLS/SLM efficiency

For SLM, process efficiency is defined as the ratio between the heat source integrated over the whole powder bed (absorbed power) and the laser power itself.

We have shown in Chapter 3, that the absorptivity of 18Ni(300) Maraging Steel powder decreases significantly due to the phase change. Melting of a powder surface under the laser can therefore cause a significant loss of the process efficiency.

Laser power P	t^{tr}
100 W	4.2 μs
200 W	2.4 μs
300 W	1.8 μs

Table 8.2 – Stabilization time of the surface state within the laser spot.

As far as the laser power and the scanning speed are kept constant and the powder is considered as a homogeneous medium, the surface state *within the laser spot* experiences a transition from powder to molten material in some time after laser irradiation start. We will denote this time as t^{tr} ('transition'). Using the simulation we can estimate t^{tr} for the selected process conditions.

Fig. 8.2 shows the laser power absorption in the beginning of the scanning. The treated cases again correspond to the process parameters used in industrial applications (Tab. 3.5). The scanning strategy is a line, $\omega = 40\ \mu$m and the laser beam profile is top-hat. The material properties correspond to 18Ni(300) Maraging Steel powder bed (Tab. 3.6) and the absorptivity evolves from 0.8 to 0.2.

Fig. 8.2 also shows that, the values of the absorbed power are close to $\alpha_l P$, when the surface state within the laser spot is completely stabilized. Therefore almost all the powder bed surface under the laser within the laser spot is molten after time t^{tr}. The measured values of the transition time t^{tr} are presented in Tab. 8.2. For the selected process parameters, t^{tr} does not exceed 5 μs.

Our conclusion is that, for 18Ni(300) Maraging Steel and the chosen process conditions and material parameters (Tabs. 3.6 and 3.5), SLS/SLM process has quite a low efficiency.

In fact, the process efficiency decrease due to the surface state evolution is defined by the ratio between powder and liquid material absorptivity. In the case of metallic powders, this ratio goes up to 4 – 5.

8.2 Convection and radiation

In Section 8.1 we have already discussed energy losses which can take place during SLS/SLM of a metallic powder due to its absorptivity evolution. However radiation and convection phenomena also can influence the process.

On the top surface Σ of the powder bed (see Fig. 6.1), the boundary condition (eq. (6.1)) can be written as:

$$k\frac{\partial T}{\partial n} = q_{\text{rad}} + q_{\text{conv}}. \tag{8.9}$$

The notations q_{rad} and q_{conv} are used for the fluxes describing the energy losses due to radiation and convection, respectively.

To estimate the effects of radiation and convection, we will compare q_{rad} and q_{conv} to the flux q_{abs} of electromagnetic energy coming from the laser (power P, radius ω) and absorbed by the material:

$$q_{\text{abs}}(x,y) = \begin{cases} \alpha_l \frac{P}{\pi\omega^2}, \text{ if } (x,y) \in \Sigma_l, \\ 0, \text{ otherwise,} \end{cases} \tag{8.10}$$

with Σ_l the laser spot (see Fig. 8.3). In eq. (8.10) α_l denotes the absorptivity of the material in liquid state: as it was shown in Section 8.1, the laser mostly interacts with molten material which justifies the use of α_l and not of α_p (powder material) or of α_s (solid bulk material).

The flux q_{conv} corresponding to convective losses, can now be expressed (see eq. (6.1)) as:

$$q_{\text{conv}} = \kappa(T - T_0), \tag{8.11}$$

where κ is the heat transfer coefficient from the heated material surface to the surrounding atmosphere of temperature $T_0 \simeq 20$ °C

The flux q_{rad}, corresponding to radiative losses, is given by Stefan-Boltzmann law:

$$q_{\text{rad}} = \varepsilon(T)\sigma((T+273)^4 - (T_0+273)^4). \tag{8.12}$$

In (8.12), $\varepsilon(T)$ is the emissivity of the material (actually, also dependent on its surface state), and $\sigma = 5.67 \cdot 10^{-14}$ W/mm^2/K^4 – the Stefan-Boltzmann constant. Equation (8.12) assumes that all the temperatures are given in °C.

8.2.1 Convection

For the estimation of the influence of the convection from the surface of a powder bed during SLS/SLM we need to know the heat transfer coefficient κ. We can calculate it, considering the melt pool, formed during laser scanning, as a hot horizontal 'plate'. This 'plate' interacts with the atmosphere. There exist convection and conduction heat flows parallel to each other and to the normal to the boundary surface of liquid metal and atmosphere. The ratio of convective to conductive heat transfer is defined by Nusselt number $\mathrm{Nu_l}$:

$$\mathrm{Nu_l} = \frac{\kappa L_c}{k_{\mathrm{atm}}}, \tag{8.13}$$

where L_c – the characteristic length of the liquid metal 'plate' and k_{atm} – the thermal conductivity of the surrounding atmosphere.

According to [85], for the top surface of a hot liquid metal plate in a colder environment:

$$\mathrm{Nu_l} = 0.54\mathrm{Ra_l}^{1/4}, \quad 10^5 \leq \mathrm{Ra_l} \leq 2 \cdot 10^7, \tag{8.14}$$

where $\mathrm{Ra_l}$ is the Rayleigh number.

We consider Ar as the protective atmosphere of SLS/SLM process: $k_{\mathrm{atm}} = 0.016$ W/m/°C.

Characteristic length of a plate representing a melt pool can be found as

$$L_c = \frac{\mathrm{Surf.area}}{\mathrm{Perimeter}}. \tag{8.15}$$

To estimate L_c we need to know the geometry of the melt pool formed during laser scanning. We can get an idea of the shape of a stabilized melt pool by drawing the isotherm $T_Q(x, y, 0) = T_f$ of the pseudo-stationary solution of the heat transfer equation for a moving non-point heat source (8.2). The results are presented in Fig. 8.3. It shows the position of the melt pool with respect to the laser spot for process parameters with maximum laser energy density: $P = 300$ W, $v = 1$ m/s. Material properties correspond to 18Ni(300) Maraging Steel bulk material (Tab. 3.6).

However Fig. 8.3 does not give the exact information about the melt pool surface area, as far as the evolution of thermal conductivity and absorptivity of the material due to its melting are not taken into account in (8.2). For more precise estimation we will use numerical modelling. According to the simulation results, for process parameters $P = 300$ W, v=1 m/s ($\omega = 40$ μm, top-hat laser beam profile) and for the material properties corresponding to the effective properties of 18Ni(300) Maraging Steel powder (Tab. 3.6), the area of a stabilized melt pool is:

$$A_{\mathrm{mp}} \simeq 0.045 \text{ mm}^2. \tag{8.16}$$

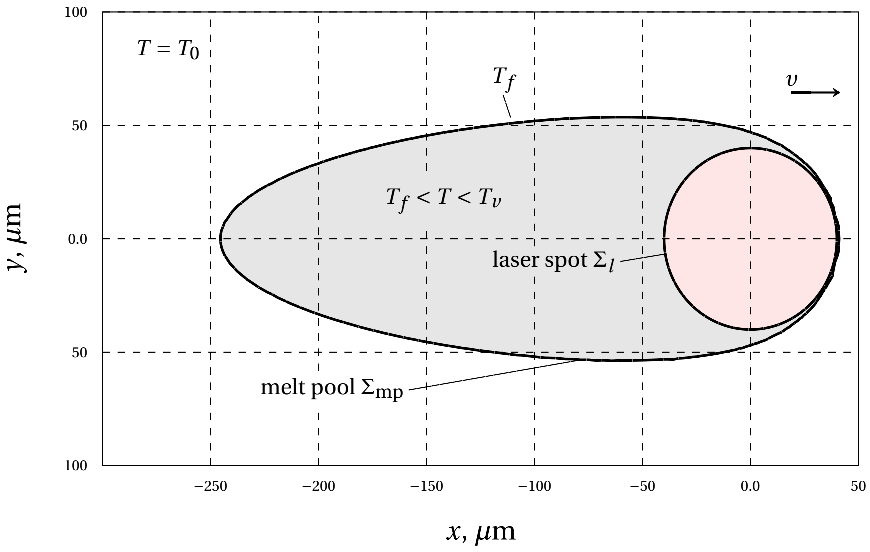

Figure 8.3 – Approximate position of the stabilized melt pool with respect to the laser spot: $P = 300$ W, $v = 1$ m/s, $\omega = 40$ μm (by Mathematica software).

Considering the melt pool Σ_{mp} as an ellipse (Fig. 8.3) with the minor semi-axis b approximately equal to the radius ω of the laser beam Σ_l (for the top-hat beam profile):

$$b \simeq \omega. \tag{8.17}$$

Then the major semi-axis can be found as:

$$a = A_{\mathrm{mp}}/\pi b. \tag{8.18}$$

The characteristic length (8.15) of an elliptical melt pool is now expressed as:

$$L_c = \frac{A_{\mathrm{mp}}}{\pi(3(a+b) - \sqrt{(3a+b)(a+3b)})}, \tag{8.19}$$

where we use the Ramanujan approximation for the ellipse perimeter [86]. For our parameters and with (8.16) – (8.18) we obtain:

$$L_c \simeq 31\ \mu\mathrm{m}. \tag{8.20}$$

Using (8.13), (8.14) and (8.19), we obtain a range for the heat transfer coefficient κ:

$$\kappa = \frac{\mathrm{Nu_l} k_{\mathrm{atm}}}{L_c}, \quad 0.005 \le \kappa \le 0.019 \quad \frac{\mathrm{W}}{\mathrm{mm}^2{}^\circ\mathrm{C}}. \tag{8.21}$$

We can now estimate the energy losses by convection during SLS/SLM. This will be done under the rough assumption that the temperature drops rapidly in the low conductive loose powder and also in the already sintered part. In that case, the only contribution to the convection losses will come from the melt pool Σ_{mp} (see Fig. 8.3) and their relative effect can be measured by the ratio:

$$\eta_{\mathrm{conv}} \equiv \frac{\iint_{\Sigma_{\mathrm{mp}}} q_{\mathrm{conv}}(x,y)\mathrm{d}x\mathrm{d}y}{\iint_{\Sigma} q_{\mathrm{abs}}(x,y)\mathrm{d}x\mathrm{d}y}. \tag{8.22}$$

The denominator in the right-hand side gives the absorbed laser power $\alpha_l P$ (8.10). To estimate the numerator, we replace q_{conv} by its value (8.11) and we observe that the temperature within the melt pool does certainly not to exceed the vaporization point T_v. We obtain

$$\eta_{\mathrm{conv}} \leq \frac{\kappa(T_v - T_0)A_{\mathrm{mp}}}{\alpha_l P}. \tag{8.23}$$

Taking the numerical values

$$T_v = 2862°\mathrm{C},\ T_0 \simeq 20°\mathrm{C}, \tag{8.24}$$

(8.21) for κ, (8.16) for A_{mp} into account and replacing α_l and P by values used for Fig. 8.3:

$$\alpha_l = 0.2,\ P = 300\ \mathrm{W}, \tag{8.25}$$

we come to the conclusion that

$$\eta_{\mathrm{conv}} \leq 1-4\%. \tag{8.26}$$

This estimation shows that the relative laser energy losses due to convection are *negligible* as long as from the melt pool is the only contribution. The actual situation can be different if the powder material and the already sintered part start to play a significative role in the convection processes.

8.2.2 Radiation

As we can see from (8.9), the estimation of laser energy losses due to radiation phenomenon requires the value of the material emissivity. An empirical formula for the emissivity of a porous media (i.e. a powder bed) is proposed in [87]. According to this model, the emissivity of a powder bed mainly depends on its porosity. For 18Ni(300) Maraging Steel powder (with the porosity of about 50%) it is approximately 0.7 – 0.8. The emissivity of a powder can also change due to its melting. The exact value of the emissivity of the liquid maraging steel is not known, but the value for the emissivity of molten steel at temperature close to the melt point can be used instead: $\varepsilon_l = 0.28$ [88]. However, since our goal is to prove that radiative losses are negligible, we will only consider the 'worst' case, when the emissivity of the material is maximum:

$$\varepsilon = 1. \tag{8.27}$$

We will again assume a quick drop of temperature inside the powder and the sintered part, so that only the melt pool contributes to radiative losses. Their effect can thus be estimated by the ratio

$$\eta_{\mathrm{rad}} \equiv \frac{\iint_{\Sigma_{\mathrm{mp}}} q_{\mathrm{rad}}(x,y)\,\mathrm{d}x\mathrm{d}y}{\iint_{\Sigma} q_{\mathrm{abs}}(x,y)\,\mathrm{d}x\mathrm{d}y}. \tag{8.28}$$

The numerator gives again the absorbed laser power $\alpha_l P$ (8.10). An upper bound for the numerator can be found by going back to the expression (8.12) of q_{rad} and by observing that the melt pool is obviously below the material melting point:

$$\eta_{\mathrm{rad}} \le \frac{\sigma((T_v+273)^4-(T_0+273)^4)A_{\mathrm{mp}}}{\alpha_l P}. \tag{8.29}$$

With the numerical values (8.24) for T_v and T_0, (8.27) for ε and (8.16) for A_{mp}, and taking the values (8.25) for α_l and P, we get

$$\eta_{\mathrm{rad}} \le 0.5\%. \tag{8.30}$$

The conclusion is that the laser energy losses due to radiation are also *negligible* if the only significative contribution is the melt pool.

8.3 Conclusions

In this Chapter we proved that in the case of SLS/SLM of metallic powders it is necessary to take the evolution of absorptivity and thermal conductivity into account. Increase of material thermal conductivity leads to efficient heat evacuation from the surface of the processed material, while the decrease of the surface absorptivity during liquefaction significantly diminishes the energy efficiency of the process. Using the example of 18Ni(300) Maraging Steel powder (Tab. 3.6), we have shown that the absorptivity evolution reduces the process efficiency by a factor of 4. The situation is similar for most of the metallic materials used in SLS/SLM.

Process productivity can be increased by the selection of operating parameters which promote the efficient laser-powder coupling. Our simulation method is certainly an efficient tool for identifying such process conditions.

We also estimated energy losses caused by radiation and convection from the powder bed during processing. The conclusion is that these mechanisms can be neglected as long as they are localized inside the melt pool: for 18Ni(300) Maraging Steel powder and chosen process parameters (Tab. 3.5) they do not exceed 5% of the laser input. An open question remains about the actual radiative and convective effects in the loose powder and in the already sintered part.

9 Melt Pool Dynamics

In Selective Laser Melting the powder grains under the laser are completely molten and form a liquid domain called melt pool. Evolution of the melt pool during the process, its interaction with the substrate and the surrounding non-molten powder strongly affect the quality of the final part.

Estimation of the melt pool geometry allows to adjust the process parameters and, therefore, to increase its efficiency. Predictions of the melt pool surface area can be also useful for the calibration of online monitoring systems for Selective Laser Melting.

In this Chapter we discuss the dynamics of the melt pool, formed in SLM of 18Ni(300) Maraging Steel powder. In the framework of the homogeneous medium hypothesis we study the stabilization of the melt pool and the evolution of its geometrical aspects during laser scanning. We also compare laser melting of a loose powder to a bulk material and propose a theoretical method, based on the transient solution of the heat transfer equation, to estimate the melt pool stabilization time and distance.

Power/speed, W/(m/s)	$t_{\mathrm{mp}}^{\mathrm{b}}$, ms	$t_{\mathrm{mp}}^{\mathrm{pb}}$, ms	$t_{\mathrm{mp}}^{\mathrm{pl}}$, ms	$t_{\mathrm{mp}}^{\mathrm{th}}$, ms ($\epsilon = 1\%$)	$t_{\mathrm{mp}}^{\mathrm{bc}}$, ms
100/1	0.18	1.6	0.2	0.424	0.36
100/2	0.05	0.4	0.1	0.175	0.15
100/3	0.04	0.8	0.08	0.107	0.08
200/1	0.28	4.5	0.64	0.7	0.67
200/2	0.12	2.3	0.16	0.305	0.27
200/3	0.07	1.0	0.08	0.19	0.15
300/1	0.5	9.5	0.8	0.963	0.93
300/2	0.18	2.5	0.3	0.429	0.4
300/3	0.14	1.5	0.16	0.272	0.24

Table 9.1 – Time to stabilize the melt pool for different process and material parameters.

9.1 Bulk material

We can simulate the melt pool behavior during laser sintering of various materials by means of our numerical model, based on the homogeneous medium hypothesis (see Chapter 6). In this section, using 18Ni(300) Maraging Steel as an example, we will estimate the time to stabilize the melt pool[1] for a bulk highly-conductive material.

Properties of bulk 18Ni(300) Maraging Steel are listed in Tab. 3.6. In the simulation we take into account melting and evaporation of the material and its absorptivity evolution due to the phase change: from 0.5 to 0.2, according to the data from Chapter 3. The heat source is treated numerically as a surface heat source. This assumption is justified by the fact that the penetration depth of the laser beam is small in comparison with the material thickness (see § 3.3.1 of Chapter 3). For the simplicity we choose a single line as scanning strategy. The laser beam profile is top-hat and its radius $\omega = 40$ μm. The material thickness is 250 μm.

Values of the time needed to stabilize the melt pool for these conditions, are presented in the second column of Tab. 9.1. We denote them as $t_{\mathrm{mp}}^{\mathrm{b}}$ ('bulk'). Also Fig. 9.1a demonstrates the melt pool behavior during the scanning for the process parameters 100/1, 100/2 and 100/3 (laser power/scanning speed).

From Tab. 9.1 and Fig. 9.1a we see that after the material melting, it takes less than 500 μs for the melt pool to stabilize. Stabilization time $t_{\mathrm{mp}}^{\mathrm{b}}$ is decreasing with the increase of laser scanning speed.

---

[1] Further in the text, if we speak about a melt pool stabilization time, calculated by means of the simulation, we mean 'stabilization time of the surface area of a melt pool'.

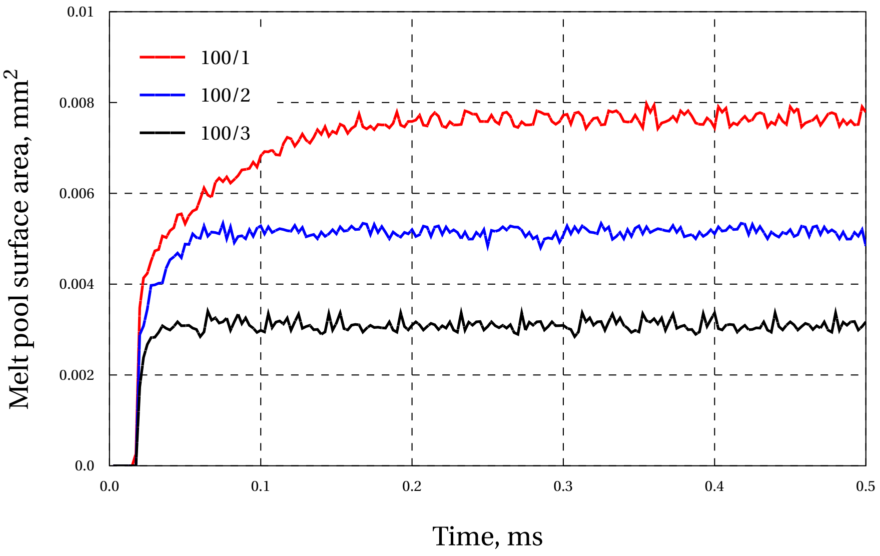

(a) 18Ni(300) Maraging Steel bulk material.

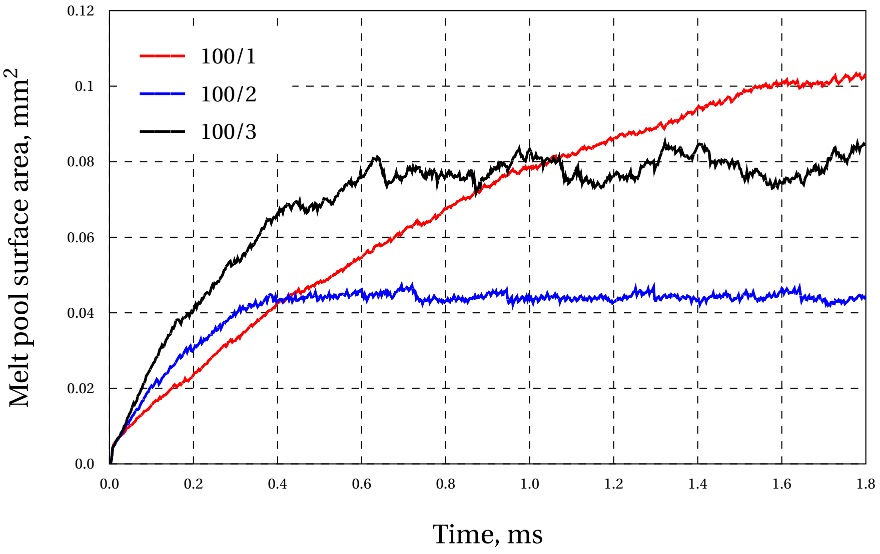

(b) 18Ni(300) Maraging Steel powder.

Figure 9.1 – Evolution of the melt pool surface area during laser scanning of 18Ni(300) Maraging Steel powder and bulk material (Tab. 3.6).

Power/speed, W/(m/s)	$h_{\rm mp}^{\rm pb}$, μm	h_l, μm	$t_{\rm mp}^{\rm pl}$, ms
100/1	48	32	0.2
100/2	28	19	0.1
100/3	22	15	0.08
200/1	66	44	0.64
200/2	41	27	0.16
200/3	34	22	0.08
300/1	76	50	0.8
300/2	57	38	0.3
300/3	48	32	0.16

Table 9.2 – Melt pool depth reached during laser melting of 18Ni(300) Maraging Steel powder.

9.2 Powder bed

In Fig. 9.1b the melt pool behavior during laser scanning of 18Ni(300) Maraging Steel powder for process parameters 100/1, 100/2, 100/3 is shown. Material properties are listed in Tab. 3.6. In the simulation we consider absorptivity (from 0.8 to 0.2) and thermal conductivity (from 0.1 to 26 W/m/°C) evolution due to the phase change of the material. The latent heat of fusion L_f and the latent heat of vaporization L_v (see Tab. 3.2) are also taken into account.

As far as we deal now with a powder bed, we consider the laser beam as a volumic heat source. The penetration depth is $\delta = 20$ μm. All other parameters stay the same as we used before: the laser beam profile is top-hat, its radius is 40 μm, we choose a single track as a scanning strategy, and the powder bed thickness is 250 μm.

In the third column of Tab. 9.1 values of the melt pool stabilization time for the case of 18Ni(300) Maraging Steel powder melting are presented. They are denoted as $t_{\rm mp}^{\rm pb}$ (‘powder bed’).

From Tab. 9.1 and Fig. 9.1b we can see that stabilization of the melt pool in the powder takes much longer (up to a factor of 10) than in the bulk material. The surface area of the melt pool, formed in the powder, is also bigger. We can explain it by the fact that the powder thermal conductivity is very low compare to the thermal conductivity of the bulk material. Non-molten powder, which surrounds the melt pool, plays the role of an insulator, while in the highly-conductive bulk material the heat is quickly evacuated from the molten region.

In the second column of Tab. 9.2 we can see the depth $h_{\rm mp}^{\rm pb}$ of the melt pool created during laser sintering of 18Ni(300) Maraging Steel powder bed. As one can observe, for the chosen process and material parameters, melt pool depth does not exceed 80 μm. The results correspond to the current tendency to use powder layer thicknesses of several tens of microns for industrial SLM of metallic powders.

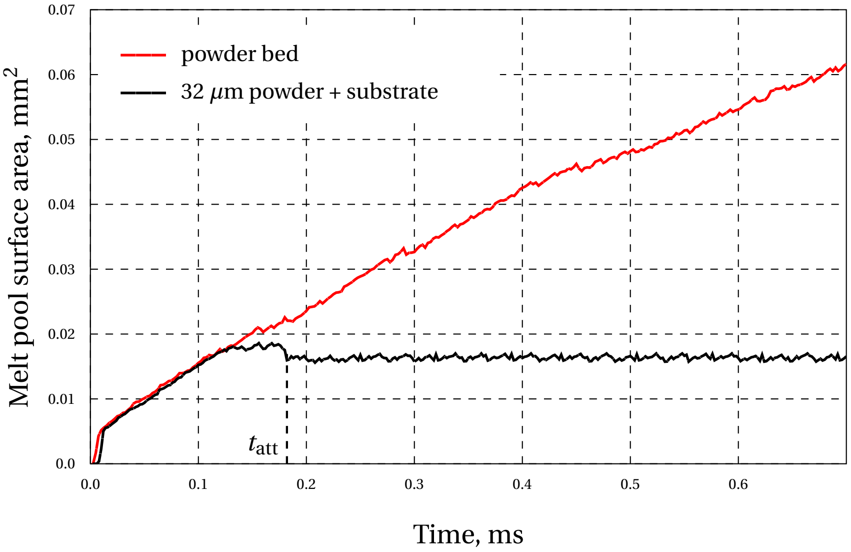

Figure 9.2 – Melt pool evolution during melting of 32 μm powder layer on a substrate: $P = 100$ W, $v = 1$ m/s.

9.3 Powder layer on a substrate

In SLS/SLM process the laser scanning is actually applied to a layer of powder on a solid substrate. The thickness of a layer is adjusted according to the properties of the processed materials. The purpose is to melt a powder layer completely in depth and to attach it to the substrate (or to the previous sintered layer). A good connection between powder layers and the substrate provides a high quality of the final part.

Substrates are often made of the same (or similar) materials as sintered powders. Similarity of the material properties between the substrate and the molten powder material allows to reach better cohesion between them.

We modelled the case of SLM process of a thin powder layer on a bulk substrate. In Fig. 9.2 (black line) we can observe the melt pool behavior during the scanning of 32 μm layer of 18Ni(300) Maraging Steel powder on a substrate, made of the same material. We compare the results to the melt pool evolution in the case of sintering of a thick powder bed (red line). Laser beam is top-hat with a power of 100 W and a radius of 40 μm, the scanning speed 1 m/s.

For these process parameters the melt pool depth h_{mp}^{pb} in the case of powder bed processing is about 48 μm (see Tab. 9.2). We choose the powder layer thickness $h_l = 32$ μm: it is equal to 2/3 of 48 μm and should provide good attachment of the molten layer to the substrate.

In Fig. 9.2 we can see the moment when the melt pool touches the substrate: we denote it as t_{att} ('attachment'). When the melt pool reaches the highly-conductive substrate (or the previous layer), the evacuation of heat from its surface into the depth becomes much more efficient. It provokes rapid cooling of the melt pool and, as a consequence, the decrease of its surface area and its earlier stabilization. The melt pool formed in a thick powder bed and surrounded by the low-conductive powder continues to grow.

We modelled the sintering of a powder layer on a substrate for all the sets of process parameters (Tab. 3.5). Each time, to have an attachment with the substrate, we adjusted the layer thickness h_l according to the values of the melt pool depth $h_{\mathrm{mp}}^{\mathrm{pb}}$, obtained for the powder bed in § 9.2. The chosen values of h_l are presented in Tab. 9.2. They correspond to $2/3$ of $h_{\mathrm{mp}}^{\mathrm{pb}}$ for each set of process parameters.

Remark 9.1. *For process parameters corresponding to the low laser energy density (for example, 100/3), h_l is of the order of the diameter of a typical powder grain ($d_0 = 8.87\ \mu m$ for 18Ni(300) Maraging Steel powder). Producing a layer of this thickness will be difficult. As a conclusion, such process parameters may not be convenient for SLS/SLM of 18Ni(300) Maraging Steel.*

Values of the melt pool stabilization time $t_{\mathrm{mp}}^{\mathrm{pl}}$ ('powder layer') are presented in Tab. 9.2. For comparison with the other results we also added $t_{\mathrm{mp}}^{\mathrm{pl}}$ in Tab. 9.1 (fourth column).

From Tab. 9.1 we can see that the values of $t_{\mathrm{mp}}^{\mathrm{pl}}$ are in good correspondence with the melt pool stabilization time for the bulk material $t_{\mathrm{mp}}^{\mathrm{b}}$. It can be explained by the fact that the used powder layer thicknesses are low. After reaching an attachment between the melt pool and the substrate, the heat transfer process is similar to the one taking place in a bulk material.

Melt pool behavior strongly depends on the thickness of powder layer, process conditions and material properties. It is however interesting to observe that, considering the cases of melting a bulk material and a thick powder bed, we obtain a lower and an upper bounds for the melt pool stabilization time of a powder layer on a substrate.

9.4 Theoretical model

In Section 8.2 of Chapter 8 we discussed theoretical methods to estimate the surface area of the melt pool formed during the selective laser melting of a given material. For this purpose we used the pseudo-stationary solution of the heat transfer equation for a non-point heat source of power P moving with speed v along x-axis on the surface of a semi-infinite material (see eq.(8.2)). However this solution only gives information about an already stabilized melt pool. When the laser starts heating a medium at room temperature T_0, the melt pool does not reach its stable state immediately. Our goal is to estimate the time necessary to stabilize it in the case of a semi-infinite material with thermal diffusivity $\eta = k/\rho/C_p$ and absorptivity α treated by a laser of power P, moving with speed v. However, to simplify the calculations, we come back to the case of a point heat source.

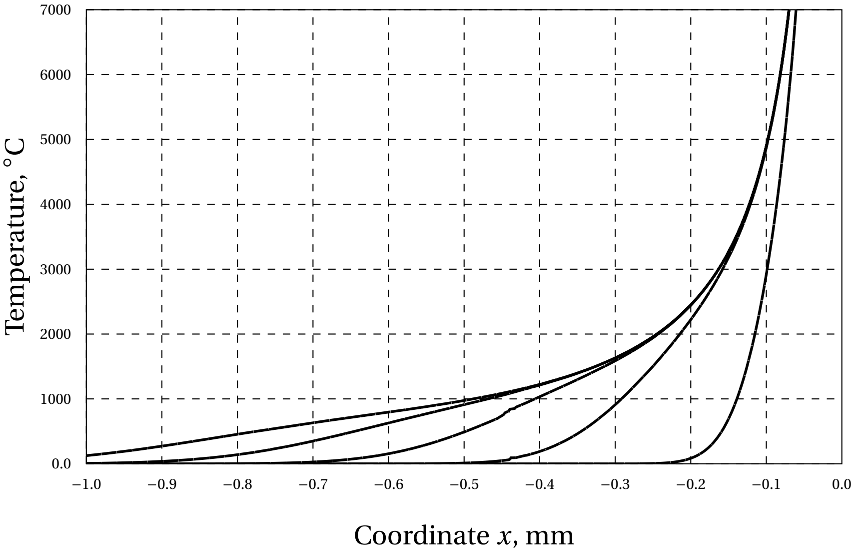

Figure 9.3 – Temperature evolution according to (9.1): 0.1, 0.3, 0.5, 0.7, 0.9 ms (from the right to the left) from the laser irradiation start: $P = 100$ W, $v = 1$ m/s.

In a referential moving with the laser, it can be seen that the temperature $T(t,x)$ at a point lying on the laser scan line at a distance x from the laser spot is:

$$\begin{aligned} T(t,x,0,0) = \frac{\alpha P}{2k\pi}\Bigg(&\frac{e^{-\dfrac{v(|x|+x)}{2\eta}}}{|x|} - \\ &- \frac{1}{2x}\Bigg(e^{-\dfrac{vx}{\eta}}\Big(1-\operatorname{erf}(\frac{vt-x}{2\sqrt{\eta t}})\Big) - \Big(1-\operatorname{erf}(\frac{vt+x}{2\sqrt{\eta t}})\Big)\Bigg)\Bigg) + T_0. \end{aligned} \tag{9.1}$$

The first term in the brackets on the right-hand sight is the pseudo-stationary solution of the Rosenthal equation, already discussed in Chapter 8 (see eq.(8.4) in § 8.1.2):

$$T_{\text{p.s.}}(x,0,0) = \frac{\alpha P}{2k\pi|x|} e^{-\dfrac{v(|x|+x)}{2\eta}}. \tag{9.2}$$

The second term in the brackets in (9.1) is a transient solution used to match $T(0,x,0,0)$ with the initial temperature distribution:

$$T(0,x,0,0) = T_0. \tag{9.3}$$

Fig. 9.3 shows an example of the evolution of the temperature profile T (9.1) in the negative part of x-axis during laser scanning for the laser power 100 W and the scanning speed 1 m/s. The moments of time are 0.1, 0.3, 0.5, 0.7, 0.9 ms from the laser irradiation start.

Material properties are listed in Tab. 9.3. They correspond to bulk 18Ni(300) Maraging Steel (see Tab. 3.6), however the absorptivity of the material stays constant during laser processing.

From Fig. 9.3 we can observe that every temperature profile ‘joins’ quickly an upper bound, which corresponds to the pseudo-stationary temperature profile (9.2).

The melt pool is obviously the area bounded by the isotherm corresponding to the melting temperature T_f of the material. As it was shown above, the extremum coordinate of this area $-r_{\mathrm{mp}}$ (in the negative part of the x-axis) will depend on time. We can calculate it, solving the equation:

$$T(t, -r_{\mathrm{mp}}(t), 0, 0) = T_f. \tag{9.4}$$

When $t \to \infty$, $r_{\mathrm{mp}}(t)$ tends to its maximum r_{mp}^{∞}, which is a solution of the equation for the pseudo-stationary temperature profile:

$$T_{\mathrm{p.s.}}(-r_{\mathrm{mp}}^{\infty}, 0, 0) = T_f. \tag{9.5}$$

Therefore from (9.2)

$$r_{\mathrm{mp}}^{\infty} = \frac{\alpha P}{2k\pi T_f}. \tag{9.6}$$

From (9.1), (9.4) and (9.6) we can conclude that the relative difference between $r_{\mathrm{mp}}(t)$ and r_{mp}^{∞}

$$\frac{r_{\mathrm{mp}}(t) - r_{\mathrm{mp}}^{\infty}}{r_{\mathrm{mp}}^{\infty}} \tag{9.7}$$

will be less than an arbitrary quality $\epsilon > 0$, if t is bigger than the value [89]:

$$\bar{t}(\epsilon) = t_{\infty} + \frac{2\eta}{v^2}\left(1 + \sqrt{1 + \frac{v^2 t_{\infty}}{\eta \ln \frac{1}{2\epsilon}}}\right) \ln \frac{1}{2\epsilon}, \tag{9.8}$$

where

$$t_{\infty} = \frac{r_{\mathrm{mp}}^{\infty}}{v}. \tag{9.9}$$

In this context we define the melt pool stabilization time $t_{\mathrm{mp}}^{\mathrm{th}}$ (‘theoretical’) as the value $\bar{t}(\epsilon)$, corresponding to a quite small relative error ϵ, e.g. $\epsilon = 1\%$.

Absorptivity α	Thermal conductivity k	Heat capacity C_p	Density ρ	T_f
0.5	26 W/m/°C	0.5 J/g/°C	0.008 g/mm^3	1413 °C

Table 9.3 – Material properties used for the estimation of the melt pool stabilization time.

In the fifth column of Tab. 9.1 we present the values of the melt pool stabilization time $t_{\text{mp}}^{\text{th}}$, calculated using (9.6), (9.8) and (9.9).

Remark 9.2. *Formula (9.8) can be validated by means of simulation. For this purpose we again model laser melting of bulk 18Ni(300) Maraging Steel. The simulation parameters are similar to the ones that we used in Section 9.1 of this Chapter (Tab. 9.3). However for the justification of (9.8) we assume the material properties to be constant. We also do not take the latent heat of fusion and the latent heat of evaporation into account.*

Simulation results are presented in the last column of Tab. 9.1. We denote them as $t_{\text{mp}}^{\text{bc}}$ ('bulk constant'). They are in a good correspondence with the values of the melt pool stabilization time $t_{\text{mp}}^{\text{th}}$, provided by formula (9.8).

From Tab. 9.1 we can see that the numerical results for the bulk material with evolving properties t_{mp}^{b} are of the same order as the results $t_{\text{mp}}^{\text{th}}$ of (9.8). Good correspondence between $t_{\text{mp}}^{\text{pl}}$ and t_{mp}^{b} also means that the theoretical method can definitely be used for the evaluation of a melt pool stabilization time in the case of laser sintering of a thin low-conductive powder layer on a massive highly-conductive substrate.

We can also observe that the melt pool stabilization time in the powder bed $t_{\text{mp}}^{\text{pb}}$ is much bigger than it is predicted by (9.8). This discrepancy can be explained by the significant difference between the thermal conductivities of the melt pool and the surrounding powder and by the evolution of the material properties during melting, which are not taken into account in (9.8).

Therefore we can conclude that, for typical industrial SLS/SLM parameters, the theoretical method, presented above, is not suitable for all types of materials. We cannot use this approach for metallic powders. However it can be applied for the estimation of the upper bound of the melt pool stabilization time in the case of materials with constant or insignificantly evolving properties.

Looking at the results, presented in Tab. 9.1, we can see that for all the types of materials the melt pool stabilization time decreases with the increase of the laser scanning speed. It can be explained by the fact that the growth of the laser speed reduces the depth of the formed melt pool (see Tab. 9.2) and shallow melt pools tend to stabilize. If the stabilization time decreases with laser speed, we can expect that their product representing the stabilization distance will be a constant. This point is discussed in the next section.

Power/speed, W/(m/s)	$d_{\mathrm{mp}}^{\mathrm{b}}$, mm	$d_{\mathrm{mp}}^{\mathrm{pl}}$, mm	$d_{\mathrm{mp}}^{\mathrm{th}}$, mm ($\epsilon = 1\%$)
100/1	0.18	0.2	0.424
100/2	0.1	0.2	0.35
100/3	0.12	0.24	0.321
200/1	0.28	0.64	0.7
200/2	0.24	0.32	0.61
200/3	0.21	0.24	0.57
300/1	0.5	0.8	0.963
300/2	0.36	0.6	0.858
300/3	0.42	0.48	0.816

Table 9.4 – Melt pool stabilization distance for different process and material parameters.

9.5 Stabilization distance

The distance, traveled by the laser before the melt pool stabilizes, is called stabilization distance and denoted as d_{mp}:

$$d_{\mathrm{mp}} = v t_{\mathrm{mp}}. \tag{9.10}$$

The theoretical model (9.8) implies:

$$t_{\mathrm{mp}} \sim \frac{1}{v}, \tag{9.11}$$

for large values of v. Therefore we might expect from (9.10) that d_{mp} will only depend on laser power and not so much on scanning speed.

To check this assumption, we compared the values of the stabilization distance $d_{\mathrm{mp}}^{\mathrm{th}}$ ('theoretical'), provided by (9.8) with simulation results for the cases of laser sintering/melting of bulk material $d_{\mathrm{mp}}^{\mathrm{b}}$ (Section 9.1) and of powder layers on a solid substrate $d_{\mathrm{mp}}^{\mathrm{pl}}$ (Section 9.3). The values of the melt pool stabilization distance for the three cases are presented in Tab. 9.4.

Tab. 9.4 confirms that the stabilization distance does not depend much on scanning speed, especially at low laser power. It also shows that, for the chosen process and material parameters (Tabs. 3.6 and 3.4) the melt pool stabilization distance is in the order of hundreds of micrometers, both for the bulk material and for the powder layer on the substrate. These results are in correspondence with the theoretical values, provided by (9.8).

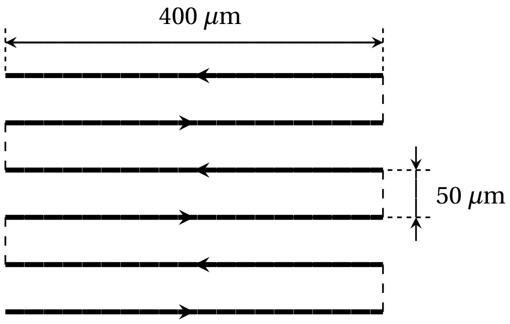

Figure 9.4 – Scanning strategy used for the numerical modelling in § 9.6.

9.6 Different scanning strategies

For the study, presented above, we always consider a single track as scanning strategy. We choose it in order to obtain precise data on the melt pool stabilization time for the selected process parameters. However, in real conditions, the melt pool behavior can be much more complicated.

As we see from Tab. 9.1, in the case of laser melting of a 18Ni(300) Maraging Steel powder layer on a massive substrate, made of the same material, the melt pool stabilization distance is of the order of several hundreds micrometers for process parameters close to industrial ones.

Another factor influencing the melt pool behavior during laser sintering is the complexity of the scanning strategy. To show it, we will study the scanning strategy presented in Fig. 9.4.

It consists of parallel lines of 400 μm length each, the hatching distance is 50 μm. After the scanning of one line, the laser is switched off during 250 μs. Then it starts moving in the opposite direction. Such a strategy is typically used to build real parts like thin walls.

We apply this scanning strategy to a 32 μm layer of 18Ni(300) Maraging Steel powder on a substrate made in the same material (Tab. 3.6). The details of all the process parameters are summarized in Tab. 9.5.

Laser power P	100 W
Scanning speed v	1 m/s
Beam profile	top-hat
Beam radius ω	40 μm
Layer thickness h_l	32 μm
Hatching distance h_h	50 μm
Laser switch-off	250 μs

Table 9.5 – Simulation parameters for the scanning strategy presented in Fig. 9.4.

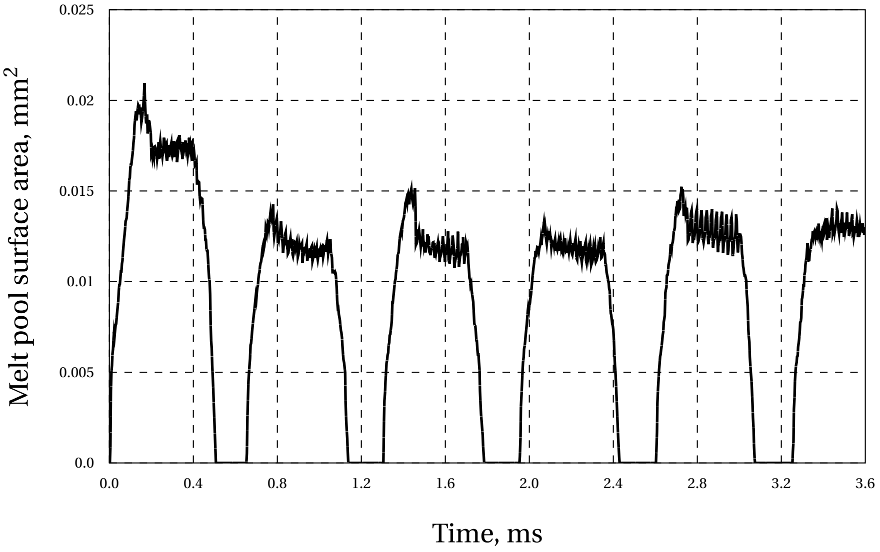

Figure 9.5 – Melt pool evolution during scanning of the strategy Fig. 9.4: $P = 100$ W, $v = 1$ m/s.

Fig. 9.5 presents the evolution of the melt pool area. One can observe that the melt pool totally disappear between the scanning of two successive lines. It means that the laser switch-off time (250 μs) is enough to reach complete resolidification of the molten regions.

The powder layer thickness is adjusted in a way to reach an attachment between the melt pool and the substrate (see Tab. 9.2). The moments, when the molten region touches the substrate, can be clearly identified on the graph in Fig. 9.5. They correspond to the quick drop of the melt pool area due to an enforced heat diffusion. As soon as it has reached the substrate, the melt pool is quickly stabilized. The oscillations correspond to the discretization of the domain, used in numerical modelling (see § 6.2.2 of Chapter 6).

Actually, the melt pool area profile of the first scanned line in Fig. 9.4 is similar to the one we have already seen in Fig. 9.2. As we have calculated, the melt pool stabilization distance $d_{\mathrm{mp}}^{\mathrm{pl}}$ is about 200 μm for a power of 100 W and a scanning speed of 1 m/s (see Tab. 9.4). Therefore the length of the line (400 μm) is enough to observe a stabilized melt pool.

From Fig. 9.5 we can see that the melt pool surface area during the scanning of the first line is bigger that for the next ones. The explanation is as follows. The hatching distance h_h of the strategy is 50 μm, the beam radius is 40 μm. Therefore the scanned track overlaps the previously sintered area (see Fig. 9.6), which possess the properties of the bulk material and is highly-conductive. It causes more efficient heat evacuation of laser energy and decreases the melt pool surface.

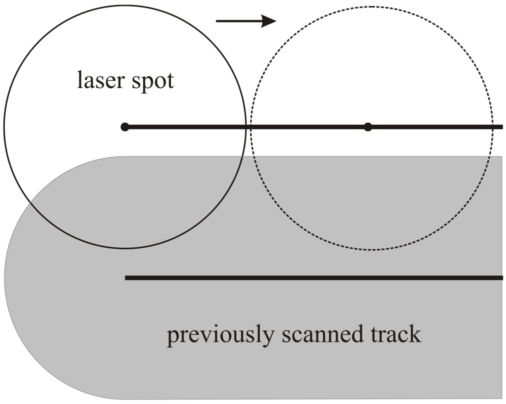

Figure 9.6 – Overlapping of scanned tracks for the strategy Fig. 9.4 and top-hat laser beam of radius 40 μm.

Partial remelting of previously sintered regions during SLS/SLM provides better quality of the final part. In this case the melt pool surface area depends on the overlap of scanned tracks. However, for homogeneous scanning strategies, we can observe some kind of melt pool stabilization (see Fig. 9.4).

There is a slight decrease of the melt pool area during the scanning of each line. It can be explained by the fact that, in the beginning, the sintered area under the laser is slightly less than in the middle of a line (see Fig. 9.6).

9.7 Conclusions

In this Chapter, we discussed the melt pool stabilization during SLM, using 18Ni(300) Maraging Steel as an example of metallic powder (Tab.3.6). We compared the melting of a bulk material, of a thick powder bed and of a thin powder layer on a substrate for typical industrial process parameters (Tab. 3.5).

In the framework of the homogeneous medium model we concluded that the time necessary for the complete melt pool stabilization during laser melting can vary from several hundreds of microseconds for bulk materials to tens of milliseconds for thick powder beds. Such a wide range is caused by the significant difference between thermal conductivities of powder and bulk materials.

We have shown that in the case of laser melting of a powder layer on a massive substrate, the stabilization time of a formed melt pool strongly depends on its attachment to the substrate, i.e. on the chosen thickness of the layer. The layer thickness should be adjusted for each set of process parameters. For this purpose, the value of the melt pool depth, obtained during SLM of a thick powder bed can be used as an upper bound for the layer thickness. For example, for 18Ni(300) Maraging Steel and our process parameters, we see that the maximum melt pool depth will never exceed 80 μm.

In the case of a good attachment of the molten region to the substrate (or to the previously sintered layer) the melt pool stabilization time is close to the value for the bulk materials – several hundreds of microseconds for our parameters.

We proposed an analytical formula (see eq.(9.8)) to predict the time for the melt pool stabilization in the case of selective laser melting of a bulk material or a powder layer on a substrate. Based on the theoretical and numerical results, we presented the melt pool stabilization distance as a better criterion for the estimation of the melt pool evolution, as far as it is not too much dependent on the laser scanning speed. It was shown that for the chosen process and material parameters, the melt pool stabilization distance never exceed 1 mm.

We have also demonstrated that in real conditions the behavior of the melt pool during SLM depends not only on the laser and material parameters, but also on the complexity of the used scanning strategy and on the dimensions of the final part.

10 Conclusions

This work is devoted to a theoretical study of Selective Laser Sintering and Selective Laser Melting of 18Ni(300) Maraging Steel powder under process conditions corresponding to operating parameters used in practical applications. For this purpose we use a finite element simulation tool, built specially for SLS/SLM. The applied numerical model is based on the homogeneous medium hypothesis. However, it is demonstrated that, for the comprehensive understanding of the process, it is not sufficient to rely only on macroscopic models.

Numerical modelling of SLS/SLM also requires

- preliminary analysis of the loose powder properties;
- study of the phenomena, taking place at the powder grain level: melting and particle interaction in the presence of liquid phase.

In this work, we have proposed theoretical approaches, allowing to estimate effective powder properties. The results were validated experimentally. It was shown that during sintering/melting of a metallic powder, the thermal conductivity and the absorptivity of the material change drastically due to the phase changes. In the domain of powder melting dynamics, we have developed a model to simulate of the melting process of a separate particle located on the surface layer of a powder bed (Single Grain Model). We have also introduced a theoretical method, which allows to estimate the interaction of molten powder grains, approaching their interaction by a coalescence mechanism.

It is shown that, for the chosen material properties and SLM operating parameters, the powder grain melting time is negligibly small (several microseconds) compared to the laser irradiation time. The same conclusion can be made about the merging time of two molten particles, which is less than 1 μs. Therefore, the stage of partial powder sintering can certainly be neglected in the SLM process under typical conditions.

Another important result is that the powder grain melting is not homogeneous. Under specific process conditions, powder sintering starts at average temperatures significantly less than the melting point of the material. To allow for this mechanism at the macroscopic level, we have proposed a completely new phenomenological evolution law for the powder sintering threshold depending on the local laser beam intensity. The approach has been experimentally validated.

The results, obtained by means of these sub-models, have been applied in the principal numerical model, based on the homogeneous medium hypothesis. This approach allowed us to simulate SLS/SLM process and to predict the final part quality with much better precision, than the commonly used macroscopic numerical models do. By means of our method, we have studied the SLS/SLM efficiency. It was shown that the evolution of the material properties during SLS/SLM strongly influences the process. Increase of material thermal conductivity leads to fast heat evacuation from the surface of the material, while the decrease of the surface absorptivity during liquefaction significantly diminishes process energy efficiency (factor 4 – 5 for metallic powders). We also estimated energy losses caused by radiation and convection from the powder bed during laser melting. The conclusion is that these mechanisms can be neglected as long as they are localized inside the melt pool.

The dynamics of the melt pool, formed during SLM, was also investigated. The dependency of the melt pool stabilization process on the used material was studied. We concluded that the time necessary for the complete melt pool surface area stabilization during laser melting can vary from several hundreds of microseconds for bulk materials to tens of milliseconds for thick powder beds. In the case of laser melting of a thin powder layer on a massive substrate, the melt pool stabilization time is close to the value for the bulk materials.

We have shown that in SLM the powder layer thickness should be chosen for each set of operating parameters. Numerical estimation of the melt pool depth, obtained during SLM of a thick powder bed, is a reliable and fast method for the layer thickness adjustment.

We proposed an analytical formula to predict the time for the melt pool stabilization in the case of SLM of a bulk material or a powder layer on a substrate. Based on the theoretical and numerical results, we came to the conclusion that the melt pool stabilization distance can be also used as a criterion for the estimation of the melt pool evolution.

By means of the simulation, we have also demonstrated that in real conditions the behaviour of the melt pool during SLM depends not only on the laser and material parameters, but also on the complexity of the used scanning strategy and on the dimensions of the final part.

In general, we have shown that our simulation software is an efficient tool for identifying optimal SLS/SLM process conditions in term of energy efficiency and for the prediction of the dimensions and the quality of the final sintered part. However, for a better accuracy of these predictions, the mechanisms of the cooling process of a sintered part should be studied and implemented into the numerical model. This must be the subject of a future investigation.

Bibliography

[1] J. Jhabvala, *Study of the consolidation process under macro-and microscopic thermal effects in Selective Laser Sintering and Selective Laser Melting.* PhD thesis, École Polytechnique Fédérale de Lausanne (EPFL), 2010.

[2] MATWEB, "`http://www.matweb.com/`," 2015.

[3] A. Gusarov and E. Kovalev, "Model of thermal conductivity in powder beds," *Physical Review B*, vol. 80, no. 2, p. 024202, 2009.

[4] V. Postovalov, E. Romanov, V. Kondrat'ev, and V. Kononenko, "Theory of transport in liquid metals: Calculation of dynamic viscosity," *High temperature*, vol. 41, no. 6, pp. 762–770, 2003.

[5] S. Thoroddsen, K. Takehara, and T. Etoh, "The coalescence speed of a pendent and a sessile drop," *Journal of Fluid Mechanics*, vol. 527, pp. 85–114, 2005.

[6] J. Kruth, B. Van der Schueren, J. Bonse, and B. Morren, "Basic powder metallurgical aspects in selective metal powder sintering," *CIRP Annals-Manufacturing Technology*, vol. 45, no. 1, pp. 183–186, 1996.

[7] J. Kruth, X. Wang, T. Laoui, and L. Froyen, "Lasers and materials in selective laser sintering," *Assembly Automation*, vol. 23, no. 4, pp. 357–371, 2003.

[8] I. Yadroitsev, P. Bertrand, and I. Smurov, "Parametric analysis of the selective laser melting process," *Applied surface science*, vol. 253, no. 19, pp. 8064–8069, 2007.

[9] W. Meiners, K. Wissenbach, and R. Poprawe, "Direct selective laser sintering of steel powder," in *Proceedings of the LANE*, vol. 97, pp. 615–622, 1997.

[10] C. Over, W. Meiners, K. Wissenbach, M. Lindemann, and G. Hammann, "Selective laser melting: a new approach for the direct manufacturing of metal parts and tools," *Proceedings of the International Conferences on LANE*, pp. 391–398, 2001.

[11] T. Wohlers, *Wohlers report 2005: rapid prototyping, tooling & manufacturing state of the industry: annual worldwide progress report.* Wohlers associates, 2005.

[12] J. Kruth, P. Mercelis, J. Van Vaerenbergh, L. Froyen, and M. Rombouts, "Binding mechanisms in selective laser sintering and selective laser melting," *Rapid prototyping journal*, vol. 11, no. 1, pp. 26–36, 2005.

[13] J. Kruth, B. Vandenbroucke, J. Vaerenbergh, and P. Mercelis, "Benchmarking of different sls/slm processes as rapid manufacturing techniques," 2005.

[14] J. Kruth, G. Levy, F. Klocke, and T. Childs, "Consolidation phenomena in laser and powder-bed based layered manufacturing," *CIRP Annals-Manufacturing Technology*, vol. 56, no. 2, pp. 730–759, 2007.

[15] P. Karapatis, *A sub-process approach of selective laser sintering.* PhD thesis, École Polytechnique Fédérale de Lausanne (EPFL), 2002.

[16] M. Rombouts, "Selective laser sintering/melting of iron-based powders," *Katholieke Univesiteit Leuven, Leuven*, 2006.

[17] N. Tolochko, M. Arshinov, A. Gusarov, V. Titov, T. Laoui, and L. Froyen, "Mechanisms of selective laser sintering and heat transfer in ti powder," *Rapid prototyping journal*, vol. 9, no. 5, pp. 314–326, 2003.

[18] B. Van Der Schueren, "Basic contributions to the development of the selective metal powder sintering process," *University of Leuven, Leuven*, 1996.

[19] P. Aggarangsi and J. Beuth, "Localized preheating approaches for reducing residual stress in additive manufacturing," in *Solid Freeform Fabrication Proceedings*, pp. 709–720, 2006.

[20] P. Mercelis and J. Kruth, "Residual stresses in selective laser sintering and selective laser melting," *Rapid Prototyping Journal*, vol. 12, no. 5, pp. 254–265, 2006.

[21] S. Kumar, "Selective laser sintering: recent advances," in *4th Pacific International Conference on Applications of Lasers and Optics, Wuhan, China*, p. 8, 2010.

[22] V. Beal, P. Erasenthiran, N. Hopkinson, P. Dickens, and C. Ahrens, "The effect of scanning strategy on laser fusion of functionally graded h13/cu materials," *The International Journal of Advanced Manufacturing Technology*, vol. 30, no. 9, pp. 844–852, 2006.

[23] V. Beal, P. Erasenthiran, C. Ahrens, and P. Dickens, "Evaluating the use of functionally graded materials inserts produced by selective laser melting on the injection moulding of plastics parts," *Proceedings of the Institution of Mechanical Engineers, Part B: Journal of Engineering Manufacture*, vol. 221, no. 6, pp. 945–954, 2007.

[24] S. Kumar, J. Kruth, J. Van Humbeeck, and A. Voet, "A study of degradation of laser-sintered moulds using wear tests," *Rapid Prototyping Journal*, vol. 15, no. 2, pp. 104–110, 2009.

[25] N. Raghunath and P. Pandey, "Improving accuracy through shrinkage modelling by using taguchi method in selective laser sintering," *International journal of machine tools and manufacture*, vol. 47, no. 6, pp. 985–995, 2007.

[26] B. Caulfield, P. McHugh, and S. Lohfeld, “Dependence of mechanical properties of polyamide components on build parameters in the sls process,” *Journal of Materials Processing Technology*, vol. 182, no. 1, pp. 477–488, 2007.

[27] A. Pilipović, T. Haramina, J. Kodvanj, and M. Šercer, “Influence of laser sintering parameters on mechanical properties of polymer products,” in *Proceedings of 3rd International Conference on Additive Technologies*, Hrvatska znanstvena bibliografija i MZOS-Svibor, 2010.

[28] M. Schmidt, D. Pohle, and T. Rechtenwald, “Selective laser sintering of peek,” *CIRP Annals-Manufacturing Technology*, vol. 56, no. 1, pp. 205–208, 2007.

[29] A. Pilipović, I. Drstvenšek, and M. Šercer, “Mathematical model for the selection of processing parameters in selective laser sintering of polymer products,” *Advances in Mechanical Engineering*, vol. 2014, 2014.

[30] L. Thijs, F. Verhaeghe, T. Craeghs, J. Van Humbeeck, and J. Kruth, “A study of the microstructural evolution during selective laser melting of ti–6al–4v,” *Acta Materialia*, vol. 58, no. 9, pp. 3303–3312, 2010.

[31] S. Das, “Physical aspects of process control in selective laser sintering of metals,” *Advanced Engineering Materials*, vol. 5, no. 10, pp. 701–711, 2003.

[32] G. Cervera and G. Lombera, “Numerical prediction of temperature and density distributions in selective laser sintering processes,” *Rapid Prototyping Journal*, vol. 5, no. 1, pp. 21–26, 1999.

[33] A. Simchi, “Direct laser sintering of metal powders: Mechanism, kinetics and microstructural features,” *Materials Science and Engineering: A*, vol. 428, no. 1, pp. 148–158, 2006.

[34] B. Xiao and Y. Zhang, “Laser sintering of metal powders on top of sintered layers under multiple-line laser scanning,” *Journal of Physics D: Applied Physics*, vol. 40, no. 21, p. 6725, 2007.

[35] T. Chen and Y. Zhang, “Three-dimensional modeling of selective laser sintering of two-component metal powder layers,” *Journal of Manufacturing Science and Engineering*, vol. 128, no. 1, pp. 299–306, 2006.

[36] L. JunChang, C. Langlade, and A. Vannes, “Evaluation of the thermal field developed during pulsed laser treatments: semi analytical calculation,” *Surface and Coatings Technology*, vol. 115, no. 1, pp. 87–93, 1999.

[37] A. Nisar, M. Schmidt, M. Sheikh, and L. Li, “Three-dimensional transient finite element analysis of the laser enamelling process and moving heat source and phase change considerations,” *Proceedings of the Institution of Mechanical Engineers, Part B: Journal of Engineering Manufacture*, vol. 217, no. 6, pp. 753–764, 2003.

[38] S. Kolossov, *Non-linear model and finite element simulation of the selective laser sintering process.* PhD thesis, École Polytechnique Fédérale de Lausanne (EPFL), 2005.

[39] I. Roberts, C. Wang, R. Esterlein, M. Stanford, and D. Mynors, "A three-dimensional finite element analysis of the temperature field during laser melting of metal powders in additive layer manufacturing," *International Journal of Machine Tools and Manufacture*, vol. 49, no. 12, pp. 916–923, 2009.

[40] T. Childs and C. Hauser, "Raster scan selective laser melting of the surface layer of a tool steel powder bed," *Proceedings of the Institution of Mechanical Engineers, Part B: Journal of Engineering Manufacture*, vol. 219, no. 4, pp. 379–384, 2005.

[41] A. Gusarov and J. Kruth, "Modelling of radiation transfer in metallic powders at laser treatment," *International journal of heat and mass transfer*, vol. 48, no. 16, pp. 3423–3434, 2005.

[42] A. Gusarov and I. Smurov, "Modeling the interaction of laser radiation with powder bed at selective laser melting," *Physics Procedia*, vol. 5, pp. 381–394, 2010.

[43] X. Wang, T. Laoui, J. Bonse, J. Kruth, B. Lauwers, and L. Froyen, "Direct selective laser sintering of hard metal powders: experimental study and simulation," *The International Journal of Advanced Manufacturing Technology*, vol. 19, no. 5, pp. 351–357, 2002.

[44] C. Argento and D. Bouvard, "Modeling the effective thermal conductivity of random packing of spheres through densification," *International journal of heat and mass transfer*, vol. 39, no. 7, pp. 1343–1350, 1996. provided by EPFL.

[45] A. Gusarov, T. Laoui, L. Froyen, and V. Titov, "Contact thermal conductivity of a powder bed in selective laser sintering," *International Journal of Heat and Mass Transfer*, vol. 46, no. 6, pp. 1103–1109, 2003.

[46] J. Steinberger, J. Shen, K. Manetsberger, and J. Muellers, "The simulation of the sls process as the basis of a process optimization," in *Proceedings of the 11th Solid Freeform Fabrication Symposium, University of Texas, Austin*, pp. 377–385, 2000. provided by EPFL.

[47] S. Safdar, L. Li, and M. Sheikh, "Numerical analysis of the effects of non-conventional laser beam geometries during laser melting of metallic materials," *Journal of Physics D: Applied Physics*, vol. 40, no. 2, p. 593, 2007.

[48] A. Bauereiß, T. Scharowsky, and C. Körner, "Defect generation and propagation mechanism during additive manufacturing by selective beam melting," *Journal of Materials Processing Technology*, vol. 214, no. 11, pp. 2522–2528, 2014.

[49] Azom, "`http://www.azom.com/`," 2015.

[50] A. Pinkerton and L. Li, "An analytical model of energy distribution in laser direct metal deposition," *Proceedings of the Institution of Mechanical Engineers, Part B: Journal of Engineering Manufacture*, vol. 218, no. 4, pp. 363–374, 2004.

[51] EMPA, "`http://www.empa.ch/`," 2015.

[52] S. Seshadri, "Effect of absorption on the spreading of a laser beam," *Optics letters*, vol. 29, no. 11, pp. 1179–1181, 2004.

[53] D. Bergström, "The absorption of laser light by rough metal surfaces," 2008.

[54] R. Glardon, N. Karapatis, V. Romano, and G. Levy, "Influence of nd: Yag parameters on the selective laser sintering of metallic powders," *CIRP Annals-Manufacturing Technology*, vol. 50, no. 1, pp. 133–136, 2001.

[55] J. Kruth, P. Peeters, T. Smolderen, J. Bonse, T. Laoui, and L. Froyen, "Comparison between co2 and nd: Yag lasers for use with selective laser sintering of steel-copper powders," *Revue internationale de CFAO et d'informatique graphique*, vol. 13, no. 4-6, pp. 95–110, 1998.

[56] N. Tolochko, Y. Khlopkov, S. Mozzharov, M. Ignatiev, T. Laoui, and V. Titov, "Absorptance of powder materials suitable for laser sintering," *Rapid Prototyping Journal*, vol. 6, no. 3, pp. 155–161, 2000.

[57] Y. Kizaki, H. Azuma, S. Yamazaki, H. Sugimoto, and S. Takagi, "Phenomenological studies in laser cladding. part i. time-resolved measurements of the absorptivity of metal powder," *Japanese journal of applied physics*, vol. 32, no. part 1, pp. 205–212, 1993.

[58] S. Sih and J. Barlow, "The measurement of the thermal properties and absorptances of powders near their melting temperatures," in *Proceedings of the Solid Freeform Fabrication Symposium 1992*, pp. 131–140, DTIC Document, 1992.

[59] C. Van Gestel, *Study of physical phenomena of selective laser melting towards increased productivity*. PhD thesis, École Polytechnique Fédérale de Lausanne (EPFL), 2015.

[60] M. Rombouts, L. Froyen, A. Gusarov, E. Bentefour, and C. Glorieux, "Light extinction in metallic powder beds: Correlation with powder structure," *Journal of applied physics*, vol. 98, no. 1, p. 013533, 2005.

[61] M. Alkahari, T. Furumoto, T. Ueda, A. Hosokawa, R. Tanaka, A. Aziz, and M. Sanusi, "Thermal conductivity of metal powder and consolidated material fabricated via selective laser melting," in *Key Engineering Materials*, vol. 523, pp. 244–249, Trans Tech Publ, 2012.

[62] Y. Shi and Y. Zhang, "Simulation of random packing of spherical particles with different size distributions," in *ASME 2006 International Mechanical Engineering Congress and Exposition*, pp. 539–544, American Society of Mechanical Engineers, 2006.

[63] AKSTEEL, "`http://www.aksteel.com/`," 2015.

[64] D. Bergström, J. Powell, and A. Kaplan, "The absorptance of steels to nd: Ylf and nd: Yag laser light at room temperature," *Applied Surface Science*, vol. 253, no. 11, pp. 5017–5028, 2007.

[65] J. Xie, A. Kar, J. Rothenflue, and W. Latham, "Temperature-dependent absorptivity and cutting capability of co2, nd: Yag and chemical oxygen–iodine lasers," *Journal of Laser Applications*, vol. 9, no. 2, pp. 77–85, 1997.

[66] J. Xie and A. Kar, "Laser welding of thin sheet steel with surface oxidation," *WELDING JOURNAL, NEW YORK*, vol. 78, pp. 343–s, 1999.

[67] P. Fischer, N. Karapatis, V. Romano, R. Glardon, and H. Weber, "A model for the interaction of near-infrared laser pulses with metal powders in selective laser sintering," *Applied physics A*, vol. 74, no. 4, pp. 467–474, 2002.

[68] G. Mie, "Beiträge zur optik trüber medien, speziell kolloidaler metallösungen," *Annalen der physik*, vol. 330, no. 3, pp. 377–445, 1908.

[69] A. Lozinskaïa and E. Boillat, "Potentiels de debye et diffraction par une sphère," *Internal communication LGPP*, 2009.

[70] M. Korolczuk-Hejnak, "Empiric formulas for dynamic viscosity of liquid steel based on rheometric measurements," *High Temperature*, vol. 52, no. 5, pp. 667–674, 2014.

[71] K. Laidler, "Chemical kinetics, 3rd," 1987.

[72] N. Eustathopoulos, B. Drevet, and E. Ricci, "Temperature coefficient of surface tension for pure liquid metals," *Journal of crystal growth*, vol. 191, no. 1, pp. 268–274, 1998.

[73] Z. Li, K. Mukai, M. Zeze, and K. Mills, "Determination of the surface tension of liquid stainless steel," *Journal of materials science*, vol. 40, no. 9-10, pp. 2191–2195, 2005.

[74] W. Hager, "Wilfrid noel bond and the bond number," *Journal of Hydraulic Research*, vol. 50, no. 1, pp. 3–9, 2012.

[75] Y. Frenkel, "Viscous flow of crystalline bodies under the action of surface tension," *SCI. SINTERING Sci. Sintering*, vol. 12, no. 1, p. 7, 1980.

[76] J. Eggers, J. Lister, and H. Stone, "Coalescence of liquid drops," *Journal of Fluid Mechanics*, vol. 401, pp. 293–310, 1999.

[77] A. Menchaca-Rocha, A. Martínez-Dávalos, R. Nunez, S. Popinet, and S. Zaleski, "Coalescence of liquid drops by surface tension," *Physical Review E*, vol. 63, no. 4, p. 046309, 2001.

[78] Y. Shikhmurzaev, *Capillary flows with forming interfaces.* CRC Press, 2008.

[79] T. Iwashita, D. Nicholson, and T. Egami, "Elementary excitations and crossover phenomenon in liquids," *Physical review letters*, vol. 110, no. 20, p. 205504, 2013.

[80] P. Clausen, M. Wicke, J. Shewchuk, and J. O'Brien, "Simulating liquids and solid-liquid interactions with lagrangian meshes," *ACM Transactions on Graphics (TOG)*, vol. 32, no. 2, p. 17, 2013.

[81] S. Kolossov, E. Boillat, R. Glardon, P. Fischer, and M. Locher, “3d fe simulation for temperature evolution in the selective laser sintering process,” *International Journal of Machine Tools and Manufacture*, vol. 44, no. 2, pp. 117–123, 2004.

[82] T. Hughes, “Unconditionally stable algorithms for nonlinear heat conduction,” *Computer Methods in Applied Mechanics and Engineering*, vol. 10, no. 2, pp. 135–139, 1977.

[83] E. Magenes, R. Nochetto, and C. Verdi, “Energy error estimates for a linear scheme to approximate nonlinear parabolic problems,” *RAIRO-Modélisation mathématique et analyse numérique*, vol. 21, no. 4, pp. 655–678, 1987.

[84] E. Boillat, “Finite element methods on non-conforming grids by penalizing the matching constraint,” *ESAIM: Mathematical Modelling and Numerical Analysis*, vol. 37, no. 02, pp. 357–372, 2003.

[85] M. Lindeburg *et al.*, *Mechanical engineering reference manual for the PE exam*. www.ppi2pass.com, 2013.

[86] S. Ramanujan, “Modular equations and approximations to π,” *Quart. J. Math*, vol. 45, pp. 350–372, 1914.

[87] S. Sih and J. Barlow, “Emissivity of powder beds,” in *Solid Freeform Fabrication Symposium Proceedings*, vol. 6, pp. 7–9, Center for Materials Science and Engineering, Mechanical Engineering Department and Chemical Engineering Department, the University of Texas at Austin, 1995.

[88] T. of Emissivity, “`http://www.monarchserver.com/tableofemissivity.pdf`,” 2015.

[89] E. Boillat, “Une solution de l’équation de la chaleur sous la forme d’un profil translaté en 3d,” *Internal communication LGPP*, 2015.

CURRICULUM VITAE

PERSONAL INFORMATION

Name	**TATIANA POLIVNIKOVA**
Date of birth	**27 APRIL 1986**
Place of birth	**RUSSIAN FEDERATION**
E-mail	**tatiana.polivnikova@gmail.com**

WORK EXPERIENCE

• Dates (from – to)	January 2010 – July 2011
• Name and address of employer	Electrosetstroyproekt, Moscow Russia
• Type of business or sector	Research and development in energy transmission sector
• Occupation or position held	researcher

EDUCATION

• Dates (from – to)	**July 2011 – September 2015**
• Name and type of organization	Laboratoire de Gestion et Procédés de Production (LGPP), Ecole Polytechnique Fédérale de Lausanne
	Doctoral student
• Dates (from – to)	**September 2003 – February 2009**
• Name and type of organization	Moscow State University, Faculty of Physics, Physical Electronics Department, Moscow, Russian Federation
• Title of qualification awarded	Master Degree in Physics